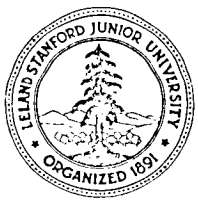

Department of AERONAUTICS and ASTRONAUTICS
STANFORD UNIVERSITY

NASA-CR-168965
19820016577

INVESTIGATION OF LASER-INDUCED IODINE FLUORESCENCE FOR THE MEASUREMENT OF DENSITY IN COMPRESSIBLE FLOWS

by

James Carter McDaniel, Jr.

SUDAAR No. 532

January 1982

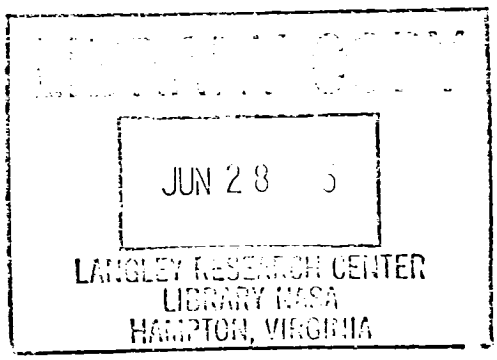

This investigation was supported by
NASA grant NAG 2-36 and in part by
AFOSR contract F49620-80-C-0091

ENTER:

DISPLAY 82N24453/2

82N24453*# ISSUE 15 PAGE 2083 CATEGORY 34

RPT#: NASA-CR-168965 NAS 1.26:168965 SUDAAR-532 CNT#: NAG2-36

F49620-80-C-0091 82/01/00 139 PAGES UNCLASSIFIED DOCUMENT

UTTL: Investigation of laser-induced iodine fluorescence for the measurement of density in compressible flows

AUTH: A/MCDANIEL, J. C., JR.

CORP: Stanford Univ., CA. CSS: (Dept. of Aeronautics and Astronautics.)

AVAIL.CASI

SAP: Avail: CASI HC A07/MF A02

CIO: UNITED STATES

MAJS: /*COMPRESSIBLE FLOW/*DENSITY MEASUREMENT/*FLUID MECHANICS/*FLUORESCENCE/*IODINE/*LASER APPLICATIONS

MINS: / ABSORPTION SPECTRA/ ARGON LASERS/ DENSIMETERS/ LASER INDUCED FLUORESCENCE/ QUENCHING (ATOMIC PHYSICS)/ RECOMBINATION COEFFICIENT/ SATURATION (CHEMISTRY)

ABS: Laser induced fluorescence is an attractive nonintrusive approach for measuring molecular number density in compressible flows although this technique does not produce a signal that is directly related to the number density. Saturation and frequency detuned excitation are explored as means for minimizing the quenching effect using iodine as the molecular system because of its convenient absorption spectrum. Saturation experiments indicate that with available continuous wave laser sources of Gaussian

ENTER: MORE

Department of Aeronautics and Astronautics

Stanford University

Stanford, California

INVESTIGATION OF LASER-INDUCED IODINE FLUORESCENCE FOR THE MEASUREMENT OF DENSITY IN COMPRESSIBLE FLOWS

by

James Carter McDaniel, Jr.

SUDAAR No. 532

January 1982

This investigation was supported by

NASA grant NAG 2-36 and in part by

AFOSR contract F49620-80-C-0091

Acknowledgments

I would like to thank my faculty advisors, Drs. Donald Baganoff and Robert Byer, for their expert technical advice and guidance during the course of this thesis investigation. I would like to express my appreciation to Eric Gustafson for his experimental assistance and to Larry Lehman for his assistance with TEX, the Stanford computer program used for the writing of this dissertation. I sincerely thank my parents and my family for their support and encouragement throughout my graduate studies.

This investigation was supported by NASA grant NAG 2-36 and in part by AFOSR contract F49620–80–C–0091.

Abstract

An experimental technique is needed for the nonintrusive measurement of the molecular number density at a point in a compressible flowfield. Laser–induced fluorescence (LIF) is an attractive approach but due to the complication of collisional quenching does not produce a signal that is directly related to the number density. The objective of this work is to investigate the use of LIF for the quantitative measurement of density in compressible flows. Two approaches for minimizing the quenching effect are explored: saturation and frequency–detuned excitation. Iodine is chosen as the molecular system in which to evaluate the feasibility of these approaches due to its convenient visible absorption spectrum.

It is shown theoretically that complete saturation would eliminate the quenching dependence of the fluorescence signal. Saturation experiments are performed which indicate that with available continuous–wave laser sources of Gaussian transverse intensity distribution only partial saturation can be achieved in iodine at the pressures of interest in gasdynamics. Therefore, it is concluded that saturation is not a viable approach to eliminating the quenching complication.

Using a fluorescence lineshape theory it is shown that for sufficiently large detuning of a narrow bandwidth laser from a molecular transition the quenching can be cancelled by collisional broadening over a large range of pressures and temperatures. Experimental data are obtained in a room temperature static cell which allow determination of the molecular quenching, collisional broadening and effective hyperfine–width constants. Data are obtained in a Mach 4.3 underexpanded jet of nitrogen, seeded with iodine, for various single–mode argon laser detunings from a strong iodine transition at 5145 Å. Using the experimentally–determined

molecular constants and the lineshape theory, good agreement is shown between the experimental and calculated fluorescence distribution in the jet flowfield. For a detuning of 3 GHz the signal is seen to be proportional to the iodine density and independent of the gasdynamic pressure and temperature over most of the flowfield; thus, the quenching dependence is effectively suppressed. The conclusion is drawn that LIF becomes a quantitative density probe by frequency detuning a narrow bandwidth laser from the molecular transition.

Contents

Tables

Figures

Chapter 1

Introduction

1.1 Diagnostic Techniques in Fluid Mechanics

Diagnostic techniques are essential to the study of fluid mechanics due to the difficulty in developing solutions to the Navier–Stokes equations and to the limited theoretical understanding of complex flows. Theoreticians and computational modelers in the field of fluid mechanics need experimental information for comparison with theory and models to advance their ability to predict such complex flows. In addition, new developments in fluid mechanics often come as the result of an experimental discovery, as in many other fields of science and engineering.

One might list desired characteristics of a general diagnostic technique, regardless of what parameter is being measured in a particular scheme. A major consideration is that the diagnostic technique be nonintrusive. This means that the measurement scheme should cause a minimal disturbance to the flow parameter that is being measured. This includes minimizing the physical displacement of particle paths and minimizing the perturbations to the thermodynamic state of the flow by the measurement process. Good spatial and temporal resolutions are certainly desired in nonuniform and unsteady flows of practical interest. The resolution requirements often place severe restrictions on diagnostic techniques and must

often be compromised when practical signal–to–noise ratios are considered. Ideally, the diagnostic scheme would provide information about a desired parameter in the flowfield without the need for additional measurements for the interpretation of the results. In other words, the output signal of the measurement scheme should be linear in the desired flowfield variable and independent of other parameters that might also vary in the flow. Other characteristics can certainly be listed as desirable in a particular application. Optical probes, when available, eliminate the physical disturbance to the flowfield that develops when employing a mechanical probe. Spatial resolution is readily achieved with optical probes using laser beams because they may be focused to very small spot sizes. However, temporal resolution and the possible perturbation of the thermodynamic state of the flowfield by the optical probe must be considered with respect to the particular scheme being employed.

There are, of course, many useful diagnostic techniques that are available for making measurements in fluid flows for particular situations. Pressure probes, hot–wire and hot–film anemometers, and thermocouples are often used to provide measurements of pressure, velocity, and temperature in a flowfield. Such devices are physical probes and one must consider the perturbations caused by the use of such probes in the particular flowfield of interest. In addition, the spatial and temporal resolution of these devices must be considered in a particular measurement. Optical schemes, such as the shadowgraph, schlieren and various interferometric techniques [1], are extremely useful for providing information about the density distribution in many fluid flows. A major limitation of such schemes is that they provide line–of–sight, or integrated, information across the entire flowfield, instead of point information. For flows that are inherently three dimensional, these approaches may not be the most desirable. Optical tomography is a new approach that may provide the capability of producing information about the density distribution in a plane of a flowfield [2]. The laser anemometer is a device that has been developed in

recent years for measuring the components of the velocity field with rather good spatial and temporal resolution. The need to control the particle size and number density in the flow in order to produce the Doppler–shifted signal and the high signal frequencies encountered in supersonic flows can be significant drawbacks. However, in general the laser anemometer is a very valuable nonintrusive probe of velocity for many flows of practical interest and has been extensively developed by many researchers in experimental fluid mechanics.

There is a present need for a technique that would complement the velocity measurement capability of the laser anemometer and provide information about the thermodynamic state in a flowfield with good spatial and temporal resolution and in a similar nonperturbing fashion. In the specialized field of aeronautics, high speed flows are often of interest and in such flows the variation in the density is often of particular interest. For example, density information is of interest in diffusion or shearing flows, both at high and low speeds. The objective of this work is to pursue the application of an optical technique for measuring density in compressible flows of interest in aeronautics. The inclusion of the requirement that the technique be applicable in a compressible flow will be seen to increase the difficulty in applying an optical probe to extract density information. It is often much simpler to measure concentrations in an environment where the pressure and temperature are essentially constants, such as in diffusion or shearing flows at low speeds. In high speed flows, all the thermodynamic parameters are variables in the flowfield and the measurement of density is often complicated by variations in the pressure and temperature as the Mach number varies in the compressible flowfield.

We will next examine physical processes that are capable of providing density information in a fluid flow and then address the particular technique to be pursued in this work.

1.2 Optical Processes of Potential Interest

There are many physical processes that may occur in the interaction of optical radiation with a molecular (or atomic) system. We will focus on the various ways in which such a system may respond when subjected to the electromagnetic field of a laser beam. It is convenient in this discussion to divide the resulting processes into four major groups: elastic scattering, inelastic scattering, absorption, and nonlinear optical effects. We will now briefly discuss these four major classes of optical processes that might be of potential use in an optical diagnostic scheme for the measurement of density in a compressible flowfield.

In scattering processes the incident laser radiation encounters a particle or a molecule and is scattered. The scattering process is termed elastic if the scattered radiation is unshifted in energy from the laser radiation. Doppler shifts that may occur due to motion of the scatterer are not the subject of this current discussion. Elastic scattering processes are divided into two types, depending on the nature of the scatterer. Rayleigh scattering results from the elastic scattering of a laser field by objects which are small compared to the wavelength of the radiation, such as a molecule. The scattering occurs at the same wavelength as the laser radiation, since the scattering is elastic, and is not specific to the scattering molecule. The process is very weak, in that the scattered radiation is a small fraction of the incident radiation. Typical Rayleigh scattering cross–sections are 10^{-26} square cm/sr. Measurements of concentration [3] and temperature [4] in turbulent flames via Rayleigh scattering have been reported. The other elastic scattering process is termed Mie scattering and occurs when the scatterer is of the order of, or larger than, the wavelength of the laser radiation. Mie scattering cross–sections are much larger than Rayleigh scattering and range from 10^{-26} to 10^{-8} square cm/sr, depending on the size of the scatterer. Mie scattering is employed in the laser anemometer

for the measurement of velocity by the Doppler–shifted radiation from the moving seed particles. It has also been used for gas concentration measurements [5], but is severely limited in high speed flows since the seed particles may not follow the details of the flowfield when the local accelerations become large.

The next class of optical processes are the inelastic scattering processes, so called because the scattered radiation is shifted in energy from the incident radiation. Spontaneous Raman scattering is an inelastic scattering process that involves an exchange of energy between the incident radiation field and the molecular system. The process is of interest in measuring density since the signal is directly proportional to the density of the scattering molecules. The scattered radiation is shifted in energy from the incident radiation by an amount that is characteristic of an energy level spacing of the molecule. Therefore, the scattering is specific to the molecule involved in the scattering process. The major drawback with the application of Raman scattering for the measurement of density in practical flows is that the scattering signals are very weak, with a typical cross–section of 10^{-29} square cm/sr. Raman scattering is, therefore, weaker than both Rayleigh and Mie scattering but can still be useful, even in the presence of the stronger elastic scattering processes, since the Raman scattered signal is shifted in frequency from the elastic scattered signals and can be spectrally selected. Many studies have been carried out of the measurement of gas concentration and temperature by laser Raman scattering [6].

The second class of inelastic scattering is termed fluorescence. Fluorescence is an inelastic scattering process that occurs when the laser radiation is tuned near a resonance of the molecular scatterer. It is much stronger than Raman scattering due to the resonant enhancement of the signal by the molecular transition. In fluorescence, a photon from the incident radiation field is absorbed by the molecule, causing the molecule to undergo a transition to an excited energy state. The excited state molecule may then decay by the emission of a photon at the same frequency as

the incident photon, sometimes called resonance fluorescence, or shifted in frequency by amounts characteristic of the energy level spacings of the molecule. However, the characteristic time of the fluorescence process is the lifetime of the excited state, which is typically 10^{-6} to 10^{-9} seconds. As a result of the long lifetimes of the excited state, collisions can result between the excited state molecule and other molecules in the flowfield, having a characteristic time between collisions of about 10^{-9} seconds at near atmospheric pressure and room temperature, before deexcitation through the fluorescence process. Therefore, the excited state molecule may undergo nonradiative energy decay by transfer of energy to colliding molecules or to adjacent energy levels within the same molecule. Other processes, such as predissociation, may also provide nonradiative energy decay channels. These nonradiative energy decay mechanisms compete with the fluorescence, or radiative decay, and serve to reduce the magnitude of the fluorescent signal and to complicate the interpretation of the fluorescent signal in terms of the density of the absorbing molecules. These nonradiative processes that compete with the radiative decay are termed *quenching* processes and are a major complication in the use of laser–induced fluorescence for the measurement of density in compressible flows. Since the quenching processes are dependent on the collision frequency, the fluorescent signal is a function of pressure and temperature in the flow, in addition to the density of the absorbing molecules. However, the fluorescent signal, with a typical cross–section of 10^{-23} square cm/sr, is many orders of magnitude stronger than the Raman signal. By monitoring the fluorescence from a point in a flow, spatial resolution can be easily achieved. Therefore, laser–induced fluorescence is a very attractive process in principle and concentration measurements of various species in flames have been reported using this technique [7]. This is the process that is considered as most promising in this work and is pursued at length in later chapters. The application of laser–induced fluorescence to the measurement of density in compressible flows

and ways to eliminate the quenching dependence in order that the fluorescent signal may be related to the density is the central theme of this work.

The third class of optical processes of interest for diagnostic applications in fluid mechanics is absorption. Absorption is a very useful scheme for measuring the density of absorbing species in flows. However, most absorption measurements have provided integrated absorption and, therefore, integrated density along the absorbing path. Methods have been proposed that involve the interaction of two intersecting laser beams to alter the absorption at a point along the absorbing path length and, therefore, improve the spatial resolution of the absorption technique [8], [9]. Additionally, sampling probes have been employed to shorten the length of the absorption path and provide more spatial resolution [10]. With these developments, density measurements may become possible using absorption, with the spatial and temporal resolution required of a density–measuring diagnostic scheme.

Nonlinear optical techniques are the fourth class of optical processes to be discussed. There are many nonlinear interactions that can occur when intense laser fields interact with a molecular system. The underlying concept in all the nonlinear processes is that the medium responds in a nonlinear fashion to the optical field, either because of an inherent nonlinearity in the medium, or because the laser field is intense enough to drive the medium to respond nonlinearly. Nonlinear optical techniques are capable of high resolution probing of molecular systems and with signal strengths many orders of magnitude greater than spontaneous Raman scattering [11]. Useful nonlinear techniques for diagnostic applications include CARS (coherent anti–Stokes Raman scattering), stimulated Raman gain and loss spectroscopy, and higher–order Raman processes. These techniques have been employed for the measurement of temperature and density in many practical flowfields [12] and are an important class of diagnostic techniques.

1.3 Laser–Induced Fluorescence and the Iodine Molecule

Fluorescence is the optical process that will be studied in this work. Fluorescence is viewed as, potentially, a very practical diagnostic scheme for the measurement of density. The fluorescent signals are much stronger than spontaneous Raman signals and easier to collect than the elastic Raleigh–scattered signal. For laboratory flows, which are free of large particles, the strong Mie scattering is not a problem. Fluorescence allows measurements to be easily made with good spatial resolution, as opposed to absorption techniques, and is a simpler approach to implement than the nonlinear techniques. However, before laser–induced fluorescence is a useful diagnostic tool, methods for dealing with the quenching complication must be found. To date, most approaches have considered the use of saturation of the absorbing transition in order to remove the quenching dependence of the fluorescent signal [7]. Subsequent chapters will deal with a theoretical description of the fluorescent process and methods of avoiding the quenching complication. First, we must discuss the specific molecule which will be employed for this investigation.

One would like to use laser–induced fluorescence from molecular oxygen or nitrogen, the primary gaseous components in air, to measure the density in a flowfield. However, the use of fluorescence requires the availability of laser frequencies that coincide with resonant frequencies of the fluorescing molecule. In the case of oxygen or nitrogen, this means that a laser source is needed at 200 nm, or further into the UV part of the spectrum. Such laser sources are not yet available with adequate power and tunability to make laser–induced fluorescence from the primary components of air practical. Therefore, until such laser sources become available, one must consider seeding the flow with a molecule that possesses a resonant transition that can be reached with currently–available laser sources. One would seed such molecules into the reservoir of the flow facility, allow them

to thoroughly premix with the primary gas in the flow system, and, assuming the mixing fraction remains constant in the resulting flowfield, infer the total density of the flow from the density of the seed molecules.

The choice of an appropriate seed molecule and laser system for inducing the fluorescence is somewhat limited when one considers the requirements for such a seed gas. The seed gas should, first of all, possess an absorption spectrum that is accessible by currently available laser systems. Since experiments in the visible part of the spectrum are easier to perform and detectors and laser sources are readily available in the visible, it is most desirable that the absorption be in the visible part of the spectrum. The seed gas should be relatively easily to handle; that is, it should not be extremely toxic to humans or corrosive to metals. It should have a relatively large room temperature vapor pressure for ease in seeding into the flow. The molecule should possess a large absorption cross-section and good quantum efficiency, in order that the fluorescent signals be reasonably large. When one considers these requirements, there are not many potential seed molecules that appear suitable.

Biacetyl is a molecule that has been proposed for laser-induced fluorescence diagnostic applications [13]. It is nontoxic, has a 40 torr room temperature vapor pressure, and absorbs in the visible and near UV where laser sources are available. Biacetyl has both a fluorescence and a phosphorescence emission. The phosphorescence is much stronger than the fluorescence and must be spectrally discriminated against due to its longer lifetime and, therefore, greater susceptibility to collisionally-induced quenching complications. Density measurements have been reported in a Mach 3 flow using laser-induced biacetyl fluorescence [14].

The seed molecule chosen for the purposes of this investigation is iodine. There are advantages and disadvantages to the use of iodine as the seed molecule. The primary advantage is that is possesses a strong absorption spectrum that ranges

from about 500 to 650 nm, in the center of the visible part of the spectrum where several laser systems are available for the excitation. The room temperature vapor pressure of iodine is 0.3 torr, far less than biacetyl, but provides an adequate seeding ratio without heating the reservoir. It is, therefore, easily introduced into the flow facility. Iodine has a large absorption cross-section and fluoresces quite strongly, even when quenched at atmospheric pressure. In addition to its large absorption cross-section, it has a relatively long fluorescent lifetime. These properties combine to produce a relatively low saturation intensity for iodine, compared to a molecule like biacetyl. Since a portion of this work is devoted to the saturation approach for eliminating the quenching complication, a low saturation intensity is highly desirable. In addition, the iodine molecule has been thoroughly studied by physical chemists and a large literature is available on the properties of the molecule. For these reasons, iodine was chosen as the seed molecule to be used in this investigation. It should be pointed out, however, that iodine is not an ideal choice from all considerations. Iodine does react with many metals, especially aluminum and copper, and is toxic to humans in large doses. For laboratory experiments these drawbacks are not too serious since one can use metals, like stainless steel, that are not attacked by iodine and can enclose the flow facility completely and exhaust the gas safely, so that the human operators are not exposed to large amounts of the iodine vapor. For the initial investigation of the application of laser-induced fluorescence to the measurement of density, iodine is a good choice. The philosophy employed in this work is that one can develop experience with the iodine molecule, even if it is not an ideal choice from all standpoints, such that when UV laser sources become available, one can apply the knowledge gathered from the iodine studies to other more suitable molecular systems.

1.4 Thesis Overview

The objective of this work is to study the application of laser–induced fluorescence from the iodine molecule for the measurement of density in compressible flows. Chapter 2 is devoted to a theoretical consideration of the subject. In that chapter, two approaches are examined for the removal of the complication of quenching in interpeting the fluorescent signal in terms of the iodine density. The next two chapters are devoted to experimental studies of these two separate approaches. Data are collected and analysed, using the theory developed in Chapter 2, to assess the practical application of the two approaches. Chapter 5 contains conclusions about the use of laser–induced iodine fluorescence for the measurement of density and ways to minimize the quenching complication. Recommendations are made for the future application of the technique for density measurements in practical compressible flows.

Chapter 2

Laser–Induced Iodine Fluorescence: Theory

2.1 Introduction

When the frequency of a laser is tuned to coincide with a molecular resonant frequency of an irradiated molecule, the molecule undergoes a transition from the ground state to a higher energy excited state. The excited state molecule can then decay to the ground state by the spontaneous emission of a photon, termed fluorescence. There are also non–radiative energy decay mechanisms, due to collisions of the excited state molecule with other molecules, that compete with the fluorescence process. These are referred to as quenching processes. These collisional quenching processes serve to reduce the fluorescence intensity and, through collisional transfer, populate energy levels other than the two levels resonant with the laser.

In order to measure the density in a compressible flow using laser–induced fluorescence, it is necessary to relate the fluorescence signal to the total number density of the seed molecules. The seed molecules are premixed in the gas reservoir and the total number density is related to the seed–gas number density through the seeding mole fraction. However, the fluorescence intensity is proportional to the

number density of *excited state* molecules, and this excited state number density must, therefore, be related to the total seed gas number density in order to make use of the fluorescence signal. To do this requires a model of the dynamics of the excitation and decay mechanisms for the two resonant energy levels and any other collisionally–coupled levels present.

It is generally accepted that the only exact way to treat the problem of the interaction of a molecular system with electromagnetic radiation is through the quantum–mechanical density matrix formalism. The alternate phenomenological approach is through the use of classical rate equations. Daily [15] has examined the range of application of the rate equations and shown that they agree completely with the density matrix equations unless the excitation laser is pulsed and the pulse rise time becomes comparable with the longest molecular collision time. For the purposes of this work, the rate equation description of the dynamics of the laser–induced fluorescence process will be employed. This choice is made because the laser sources employed in the experimental portion of this work are continuous–wave (cw), not pulsed, devices and, in addition, the rate equations lead to a simpler set of equations and a more straightforward physical interpretation than the density matrix formulation.

A rate equation model for the iodine molecule is presented in Section 2.2. The resulting rate equations are then solved for the two cases of narrow bandwidth laser excitation (Section 2.3) and broadband laser excitation (Section 2.4). The two solutions are used to review the two approaches (frequency detuning and saturation) that were experimentally investigated for relating the fluorescence signal to the total number density.

2.2 Rate Equation Model for the Iodine Molecule

In constructing a rate equation model, one must identify the resonant energy levels, any other levels containing significant population, and the important rate processes that couple these levels. Even in a simple diatomic molecule, like iodine, this identification can involve many vibrational–rotational levels in the electronic states, and many rate processes between these levels. One would like to use the simplest possible rate equation model that contains all the physical processes of importance to the phenomenon of interest. In order to decide which levels and rates were essential to a description of iodine, an extensive literature search was performed. The results of this literature search are summarized in Appendix A, which includes a discussion of the basic spectroscopy and energy transfer mechanisms of the iodine molecule. The reader is referred to this appendix for a complete discussion of the background material for the rate equation model. Only the essential features needed to understand the model will be included here. This discussion will concentrate on the overlapping P(13) R(15) lines in the 43–0 band of the iodine B–X electronic transition, since these fall within the gain profile of the strong 5145Å argon–laser line used in the experiments. These two lines will be considered together as a single effective transition since they differ only in the initial rotational level and, thus, are very similar.

Figure 1 presents a diagram of the simplest rate–equation model that can be used for this iodine transition. In this diagram, energy levels are denoted by horizontal lines and energy transfer rate processes are denoted by arrows connecting the levels. The ground electronic, X, state consists of many vibrational–rotational levels. The total population in all these ground levels is labeled as N_1. The population in the individual levels is given by the Boltzmann distribution when the system is in thermodynamic equilibrium. The fraction of the ground state

population which is in the level resonant with the laser is denoted by f_1. The laser pumps molecules from this resonant ground level to the resonant excited level via the stimulated rate coefficient b_{12}, thus populating a single vibrational–rotational level in the electronic B state. Through collisions, population is transferred to additional levels in the excited state. The total population in the excited electronic state is labeled as N_2. The fraction of this population in the resonant level is denoted by f_2. The excited state molecules can then return to the ground state via several rate processes: stimulated emission, b_{21}, spontaneous emission, A_{21}, or collisional quenching, Q_{21}. In addition, some collisions with excited state iodine molecules cause the molecules to predissociate through the rate coefficient Q_{23}, to produce iodine atoms in level 3 with population N_3. These iodine atoms recombine through

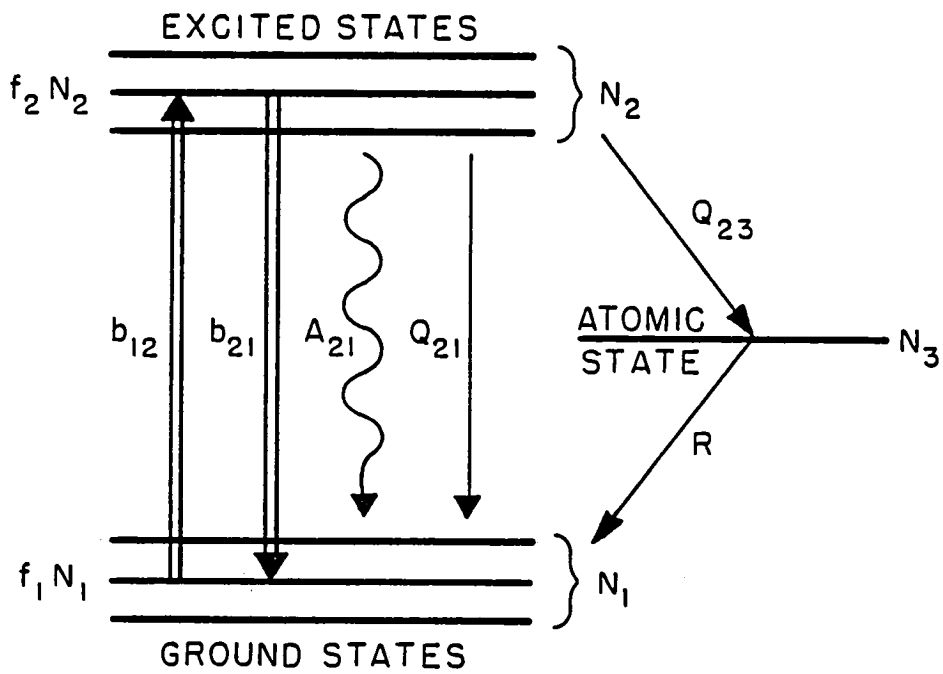

Fig. 1. Rate–Equation Diagram for the Iodine Molecule

the three–body recombination rate, R, to produce ground state molecules.

In drawing the rate–equation diagram in this way, the excited state has effectively been lumped into a single level, except that only a fraction of this level is considered to be resonant with the laser. A rate equation will be written for this single lumped level. The spontaneous emission rate, A_{21}, and the collisional quenching rates, Q_{21} and Q_{23}, actually depend on the specific excited level involved, but are taken here to be single values, averaged over the entire collection of levels. This approximation is consistent with our desire to collect the broadband fluorescence from all the upper levels and not to study the details of the energy transfer process within the upper and lower states. In a more complete model, if needed for energy transfer studies, the upper and lower states would be split into several levels which are coupled by collisional transfer rates. In the present model this complexity is absorbed in the fractions f_1 and f_2, and the question of what values to use for these fractions and whether they depend strongly on experimental parameters, like the total pressure or the laser intensity, then arises. Lucht and Laurendeau [16] have considered this question and concluded that the fraction in the upper level, f_2, is determined primarily by the ratio of the rates of rotational transfer to collisional quenching and is independent of laser intensity. Since the two rates have the same pressure dependence their ratio is independent of pressure and, thus, the fraction f_2 is independent of pressure as well as laser intensity. In the context of this work, the fraction f_2 will be taken to be a number which will be determined from the experimental data. As discussed in Reference 2, the fraction in the lower level, f_1, does depend on the laser intensity and decreases by a factor of about two from the Boltzmann value as full saturation is approached. The fraction f_1 in this work will be taken to be that given by the Boltzmann distribution and, thus, determined by the temperature alone. This approximation will be seen to be acceptable in that full saturation is never approached in the experiments and the resulting error is far

less than the factor of two calculated by Lucht and Laurendeau.

Given the diagram in Figure 1, rate equations which describe the rate of transfer of molecules between the three levels, as induced by the laser, are easily written. A separate equation is written for the time rate of change of the number density of molecules in each level. The terms in the equations consist of products of the number density of the level and the corresponding rate coefficient, except for recombination, which is quadratic in number density. The rate equations for the number density of molecules in the three iodine energy levels are then given by

$$\frac{dN_2}{dt} = b_{12}f_1N_1 - (b_{21}f_2 + A_{21} + Q_{21} + Q_{23})N_2 \tag{2.1}$$

$$\frac{dN_1}{dt} = -b_{12}f_1N_1 + (b_{21}f_2 + A_{21} + Q_{21})N_2 + RN_3^2 \tag{2.2}$$

$$\frac{dN_3}{dt} = 2Q_{23}N_2 - 2RN_3^2 . \tag{2.3}$$

In writing the collisional rate coefficients in this way, they are defined as the average number of collisions per second per excited state molecule that produce the specific results. For example, Q_{23} represents the average number of collisions per second per excited iodine molecule that result in a predissociation event, thereby producing two iodine atoms. Similarily, R is the rate coefficient for three body collisions involving the recombination of two iodine atoms into a ground state iodine molecule, with a third body required to carry off the energy released in the recombination process. The rate coefficient A_{21} is the transition probability per unit time for spontaneous emission of a photon by an excited state iodine molecule, a known constant for iodine (Appendix A). As mentioned previously, the spontaneous emission coefficient depends on the specific upper and lower states involved in the fluorescent emission through the Frank–Condon factors for the two wavefunctions. However, since the total broadband fluorescent emission is the observed quantity in this work, this

coefficient will be taken as the average transition probability for the collection of fluorescent transitions involved. The b_{ij} coefficients represent the number of stimulated transitions per second per molecule. The exact form for the stimulated coefficients depends on the relationship between the linewidth of the laser and the molecular absorption linewidth and will be considered in the next two sections.

In addition to the rate equations, there is a constraint on the system that the total number of iodine atoms, N_I, is a conserved quantity regardless of whether they appear as free atoms or as iodine molecules. Atom conservation is expressed as

$$2N_1 + 2N_2 + N_3 = N_I . \tag{2.4}$$

Equations (2.1)-(2.4) represent the complete coupled set of equations for the time-dependent populations in the three iodine energy levels. In this work we are interested in the steady state solution to these equations since the laser employed is cw, not pulsed. (The steady state solution may be employed even in pulsed laser experiments as long as the pulse duration is greater than the fluorescence lifetime of the transition [17].) To develop the steady state solution we set the left-hand sides of Equations (2.1), (2.2), and (2.3) to zero and solve the resulting set of algebraic equations. We then have four algebraic equations for the three unknowns, N_1, N_2, and N_3; however, it is easily seen that Equations (2.2) and (2.3) combine, with the aid of (2.4), to give Equation (2.1). Therefore, we may use Equations (2.1), (2.4), and either (2.2) or (2.3) in developing the solution.

The three algebraic equations are solved for N_2 since the fluorescence signal is proportional to the excited state number density. It is seen that the three equations are a nonlinear set, due to the recombination term. It is also seen that a much simpler solution could be developed by using Equations (2.1) and (2.4) if the atomic population, N_3, could be neglected in Equation (2.4). Two linear equations

for the two unknowns, N_1, and N_2, then result. Measurements were made by Rabinowitch and Wood [18] of the steady state atomic population produced by an intense broadband cw lamp and they found that less than one percent of the iodine molecules were dissociated into atoms. The conditions of these experiments were comparable to those of gasdynamic interest. This suggests that the neglection of N_3 in (2.4) is a reasonable approximation, especially since the laser excites only a small fraction of the ground state population whereas the broadband lamp pumps essentially all the molecules. Since the neglection of N_3 is a critical assumption in the following development, the solution of the set of nonlinear equations is presented in Appendix B. It is shown in Appendix B that Q_{21} must be much larger than Q_{23} for our experimental conditions and, therefore, that very few excited state molecules pass through the atomic level. The atomic population can thus be neglected in using (2.4). It is also shown that the nonlinear solution consists of two terms: the first term is precisely the solution obtained by neglecting N_3 in Equation (2.4) and the second term is the nonlinear contribution and is much smaller than the first for the value of Q_{23} consistent with the experimental data. For the remainder of the theoretical development the first term will be utilized since it is algebraically much easier to handle and the resulting equations are much more transparent to physical interpretation.

The approximate set of rate equations to be solved when the atomic population is neglected in (2.4) is

$$\frac{dN_2}{dt} = b_{12} f_1 N_1 - (b_{21} f_2 + A_{21} + Q) N_2 \tag{2.5}$$

$$N_1 + N_2 = N_{I_2}\,, \tag{2.6}$$

where N_{I_2} is the total *molecular* number density and is assumed to be a constant

and Q is now defined to be the total collisional quenching rate,

$$Q = Q_{21} + Q_{23}.$$

If N_{I_2} is allowed to vary in (2.6) then the equation is exact. The approximation is introduced by taking N_{I_2} to be a constant. These two equations are the starting point for the development of the next two sections. In both sections the development follows the same pattern: first an expression is presented for the stimulated rate coefficient, consistent with the desired laser linewidth, then the equations are solved for N_2, and finally an expression is developed for the total fluorescence emission. The two solutions show that the fluorescence emission depends on the bandwidth of the laser used to excite the molecule. The solutions also suggest different approaches in minimizing the complication of collisional quenching when interpeting the fluorescent emission in terms of the total iodine number density.

2.3 Fluorescence Induced by a Narrow Bandwidth Laser

2.3.1 Piepmeier Theory Applied to Iodine Fluorescence

A theory of laser saturated *atomic* resonance fluorescence has been developed by Piepmeier [19]. The development was carried out for the case of excitation by a narrow bandwidth laser of arbitrary intensity. The theory starts with a rate equation model for an atom with three active levels. In applying his theory to a molecule, one needs only to use a rate equation model applicable to the specific molecular system considered. Such a model has been developed for iodine in the previous section. The remainder of the theory in this section is motivated by Piepmeier's development, with a few extensions and modifications.

If the laser used to excite the molecule has a bandwidth that is less than, or on the order of, the linewidth of the molecular transition then the molecular lineshape must be included in the stimulated rate coefficient. In Piepmeier's development the laser is considered to be monochromatic and pressure broadening of the transition is treated by a collision theory. Collisions are thought of as interrupting the coherence of the fluorescence process, thereby shortening the lifetime of the excited state, and producing collisional, or Lorentz, broadening of the transition.

This collisional broadening in gases is an example of the general class of homogeneous broadening, so termed because all the molecules are affected uniformly by the broadening mechanism. Every molecule in the collection thus has the same resonance frequency and lineshape and the same frequency response to an applied laser signal. The other broadening class is inhomogeneous broadening, represented in gases as Doppler broadening. In inhomogeneous broadening, different groups (spectral packets) of molecules have slightly different resonant frequencies on the same transition. The overall response of the collection of molecules is thus spread out in frequency due to the smearing of the center frequencies of the various spectral packets. An applied laser signal now interacts strongly only with molecules whose shifted resonance frequencies are close to the laser frequency. Therefore, in a strongly inhomogeneously–broadened transition the laser does not have the same effect on all the molecules in the collection. In gases this smearing of the center resonant frequency of the molecules is due to the velocity of the molecules which produces a Doppler shift in the resonant frequency of the molecule as seen by the laser radiation. Both Doppler and collisional (Lorentz) broadening will be considered in the following development. Natural broadening (another type of homogeneous broadening) will be neglected since it's contribution to the total linewidth is much less than either Doppler or collisional broadening for the pressure and temperature regimes to be considered in this work.

The rate equations can be written to exhibit the frequency dependence of the molecular lineshape as

$$\frac{dN_2(\nu)}{dt} = b_{12}(\nu) f_1 N_1(\nu) - [b_{21}(\nu) f_2 + A_{21} + Q] N_2(\nu)$$

$$N_1(\nu) + N_2(\nu) = N_{I_2}(\nu).$$

In order to account for the effect of inhomogeneous broadening, the equations are written for the number density in the two levels, *in a specific Doppler interval* $d\nu$, where the stimulated rate coefficients, b_{ij}, contain the Lorentzian part of the molecular lineshape. Before introducing the exact frequency dependence of the molecular lineshape, the steady–state solution for the excited state number density, $N_2(\nu)$, in a given Doppler interval, $d\nu$, can be solved for as

$$N_2(\nu) = f_1 N_{I_2}(\nu) \frac{1}{A_{21} + Q} \frac{b_{12}(\nu)}{1 + [b_{12}(\nu) f_1 + b_{21}(\nu) f_2]/(A_{21} + Q)}. \tag{2.7}$$

We can now introduce the expression for the stimulated rate coefficient and then integrate over all the Doppler intervals in order to describe the average state of the entire molecular collection.

The stimulated rate coefficient for a molecular transition of resonance frequency ν (in Hz), excited by a monochromatic laser of frequency ν_L, and intensity I (in watts per square cm), is written as

$$b_{ij} = \frac{1}{c} B_{ij} I g(\nu - \nu_L), \tag{2.8}$$

where

$$g(\nu - \nu_L) = \frac{\Delta\nu_c/2\pi}{(\nu - \nu_L)^2 + \Delta\nu_c{}^2/4} \tag{2.9}$$

is the normalized Lorentzian lineshape function with a full width at half maximum (FWHM) given by $\Delta\nu_c$ [20]. The speed of light (in vacuum), denoted by c, is needed since the definition is in terms of intensity, not energy density. With this definition, the relation between the stimulated and spontaneous rate coefficients is given by the formula [20]

$$A_{21} = \frac{8\pi h\nu^3}{c^3} B_{21} \,. \tag{2.10}$$

The two stimulated rate coefficients are related by [20]

$$g_1 B_{12} = g_2 B_{21} \,, \tag{2.11}$$

where g_1 and g_2 are the degeneracies (number of available states) of the two resonant energy levels.

Substituting the explicit frequency dependence of b_{ij} given by (2.8) and (2.9) into Equation (2.7), with the aid of (2.11), gives the steady–state number density in level 2 in a given Doppler interval as

$$N_2(\nu) = \frac{f_1}{c} \frac{B_{12}}{A_{21} + Q} N_{I_2}(\nu) \frac{\Delta\nu_c}{2\pi} \frac{I}{(\nu - \nu_L)^2 + \left(\Delta\nu_c{}^2/4\right)(1 + I/I^{sat})} \,, \tag{2.12}$$

where the saturation intensity, I^{sat}, is defined as

$$I^{sat} = \frac{\pi c\, \Delta\nu_c}{2} \frac{A_{21} + Q}{B_{12}} \frac{1}{f_1 + f_2 g_1/g_2} \,. \tag{2.13}$$

The relation between the total number density in a given Doppler interval, $N_{I_2}(\nu)$, and the total number density in all intervals, N_{I_2}, is given by the velocity distribution function. For a Maxwellian distribution we have [20]

$$\frac{N_{I_2}(\nu)}{N_{I_2}} = \sqrt{\frac{4\ln 2}{\pi}} \frac{1}{\Delta\nu_D} \exp\left[-4(\ln 2)\left(\frac{\nu - \nu_o}{\Delta\nu_D}\right)^2\right], \tag{2.14}$$

where

$$\Delta\nu_D = \sqrt{\frac{8(\ln 2)kT}{mc^2}}\,\nu_o \tag{2.15}$$

is the FWHM of the distribution and ν_o is the molecular center frequency with no Doppler shift. Substituting for $N_{I_2}(\nu)$ and integrating over all frequencies in order to sum up the Doppler spectral packets gives

$$N_2 = \sqrt{\frac{4\ln 2}{\pi}}\frac{B_{12}/c}{A_{21}+Q} f_1 N_{I_2} I \frac{\Delta\nu_c}{2\pi\,\Delta\nu_D} \int_{-\infty}^{+\infty} \frac{\exp[-4(\ln 2)((\nu-\nu_o)/\Delta\nu_D)^2]\,d\nu}{(\nu-\nu_L)^2 + (\Delta\nu_c^2/4)(1+I/I^{sat})}. \tag{2.16}$$

The integral occurring in Equation (2.16) is the convolution of the Gaussian and Lorentzian distributions and is known as the Voigt integral [21]. The equation can be cast into the standard form of the Voigt integral with the following substitutions

$$y = 2\sqrt{\ln 2}\,\frac{\nu-\nu_o}{\Delta\nu_D} \tag{2.17}$$

$$D = 2\sqrt{\ln 2}\,\frac{\nu_L-\nu_o}{\Delta\nu_D} \tag{2.18}$$

$$B = \sqrt{\ln 2}\,\frac{\Delta\nu_c}{\Delta\nu_D} \tag{2.19}$$

$$B' = B\sqrt{1+I/I^{sat}}. \tag{2.20}$$

The final expression for the number density of excited state molecules then becomes

$$N_2 = \sqrt{\frac{4\ln 2}{\pi}}\frac{B_{12}/c}{A_{21}+Q}\frac{f_1}{\Delta\nu_D} N_{I_2} \frac{I}{\sqrt{1+I/I^{sat}}} V(D,B'), \tag{2.21}$$

where

$$V(D,B') = \frac{B'}{\pi}\int_{-\infty}^{+\infty} \frac{\exp(-y^2)\,dy}{B'^2+(D-y)^2} \tag{2.22}$$

is the standard Voigt integral. The parameters in the Voigt integral are the normalized detuning, D, and the saturated broadening parameter, B', as defined in the above equations. The integral cannot be expressed in terms of common functions but can be related to the complementary error function of a complex variable or to the plasma dispersion function [21],[22]. Extensive tabulations of the Voigt integral are also available [23].

The fluorescence emission is now easily related to the excited state number density. For collection of the fluorescence at 90 degrees to the laser beam and neglecting absorption outside the observation volume (a valid assumption for the concentrations of iodine to be considered), the fluorescence signal can be expressed as [24]

$$S_F = \eta h\nu \frac{\Omega}{4\pi} A_{21} \int N_2 \, dV, \tag{2.23}$$

where η is the collection efficiency and Ω is the solid angle of the collection optics. The integration is taken over the observation volume defined by the collection optics. For the purposes of this section, the excited state population will be considered constant over the observation volume. (In the next section where the saturation effects are investigated more thoroughly, the transverse intensity distribution of the laser beam causes a nonuniform population over the volume and the integration must be carried out.) Substituting for N_2 from Equation (2.21) above gives the desired expression for the fluorescence signal

$$S_F = \eta h\nu \frac{\Omega}{4\pi} V_c \sqrt{\frac{4\ln 2}{\pi}} \frac{1}{\Delta\nu_D} \frac{A_{21}}{A_{21}+Q} \frac{I}{\sqrt{1+I/I^{sat}}} \frac{B_{12}}{c} V(D,B') f_1 N_{I_2}, \tag{2.24}$$

where V_c is the observation volume.

Before proceeding further, it is desirable to examine Equation (2.24) and its implications for the measurement of density in a compressible flowfield. The factor

$A_{21}/(A_{21}+Q)$ is the fluorescence efficiency or Stern–Volmer factor, and is simply the ratio of the radiative decay rate to the total decay rate. The quantity B_{12} is the absorption line strength and $V(D,B')$ is the absorption lineshape. Therefore, the equation shows that the fluorescence signal is given by the product of the absorption coefficient, the number of absorbing molecules, the laser intensity, the fluorescence efficiency, and the collection efficiency. This seems quite reasonable and could have been written without the use of rate equations.

The rate equation approach is most useful in developing the expression to account for the saturation effects, apart from getting all the proper constants. It is seen that the effects of saturation appear in two places in the equation. In the first place, Equation (2.20) shows that the laser intensity causes the broadening parameter, B', to be power dependent, a phenomenon referred to as power broadening [20]. Secondly, if the laser intensity becomes on the order of the saturation intensity, I^{sat}, the signal no longer depends linearly on the laser intensity but is said to *saturate*. The exact nature of this saturation depends on the dominant broadening mechanism for the particular transition. In the homogeneously–broadened limit the Voigt integral becomes [19]

$$\lim_{\substack{D=0 \\ B' \gg 1}} V(D,B') = \frac{1}{\sqrt{\pi}B'}$$

and, therefore, it follows that

$$S_F = \eta h\nu \frac{\Omega}{4\pi} V_c \frac{2}{\pi \Delta\nu_c} \frac{A_{21}}{A_{21}+Q} \frac{I}{1+I/I^{sat}} \frac{B_{12}}{c} f_1 N_{I_2}. \tag{2.25}$$

The transition is said to saturate homogeneously, or *bleach*. However, in the inhomogeneously–broadened limit ($B' \ll 1$) the Voigt integral approaches unity and (2.24) becomes

$$S_F = \eta h\nu \frac{\Omega}{4\pi} V_c \sqrt{\frac{4\ln 2}{\pi}} \frac{1}{\Delta\nu_D} \frac{A_{21}}{A_{21}+Q} \frac{I}{\sqrt{1+I/I^{sat}}} \frac{B_{12}}{c} f_1 N_{I_2}. \tag{2.26}$$

The transition is now said to saturate inhomogeneously, commonly referred to as *hole-burning*. These saturation formulas are consistent with the density matrix calculations [20]. Therefore, we see that Equation (2.24) correctly includes the saturation effects.

The objective of this work is to seed iodine into the reservoir of a flow facility and then to use laser-induced iodine fluorescence to measure the iodine number density at some point in the downstream compressible flowfield. Consequently, the desired outcome is to have the the fluorescence signal, S_F, be proportional to N_{I_2} alone. The complication that arises is that other factors are present in Equation (2.24) which depend on the total pressure and temperature, quantities that vary in a compressible flow in addition to the number density. The pressure and temperature dependence of these factors is considered in the next subsection. In order to use the fluorescence signal to measure the iodine number density, Equation (2.24) seems to require a knowledge of the gasdynamic pressure and temperature as well! Even if these measurements could be made at the same point in the flow, the correction of data would be nontrivial. What is desired is a way to use Equation (2.24) so that the signal could be related to the number density without the need for other measurements. Two ways to effect this simplification are examined in this work. One is to make the frequency detuning, D, very large so that the Voigt integral asymptotically approaches a simpler form. This approach will be considered in Section 2.3.3. The other is to use intense laser radiation to attempt saturation of the transition, as considered in Section 2.4. Before these are discussed, the pressure and temperature dependence of Equation (2.24) is examined in the next section.

2.3.2 Pressure and Temperature Dependence of Fluorescence Signal

There are four quantities in the expression for the fluorescence signal, Equation (2.24), that depend on the pressure and temperature. The first two are the collisional

quenching rate, Q, which appears in the Stern–Volmer factor, and the collisional linewidth, $\Delta\nu_c$, which occurs in the broadening parameter, B', of the Voigt integral. Since both of these parameters depend on the collision–number, they can be written as the product of a cross–section, a number density of collision partners, and the average molecular speed [25]. Therefore, the proper scaling to be used to calculate these quantities in a compressible flow are, given their values at a reference condition of one torr and 298 K,

$$Q = C_q \frac{p(\text{torr})}{(1\,\text{torr})} \sqrt{\frac{298\,\text{K}}{T(\text{K})}} \tag{2.27}$$

$$\Delta\nu_c = C_b \frac{p(\text{torr})}{(1\,\text{torr})} \sqrt{\frac{298\,\text{K}}{T(\text{K})}}, \tag{2.28}$$

where C_q and C_b are the collisional quenching and broadening cross–sections, respectively, and p and T are the pressure and temperature. The assumptions implicit in these equations are that the gas obeys the perfect gas law and that the cross–sections are not strongly temperature dependent. The final two pressure and temperature dependent parameters in Equation (2.24) are the Doppler linewidth, $\Delta\nu_D$, and the initial population fraction, f_1. The Doppler linewidth is purely temperature dependent and is given by Equation (2.15). Since the ground state is assumed to remain approximately Boltzmann during the laser–induced fluorescence process, the population fraction f_1 is given by the product of the vibration and rotational population fractions

$$f_1 = \frac{1}{Z_v} \exp\left[\frac{-E_v}{kT}\right] \frac{B(2J+1)}{kT} \exp\left[\frac{BJ(J+1)}{kT}\right]. \tag{2.29}$$

In this equation, B is the rotation constant, E_v is the vibrational energy, J and v are the angular momentum and vibrational quantum numbers of the state, and Z_v

is the vibrational partition function given by

$$Z_v = \sum_v \exp\left(\frac{-E_v}{kT}\right).$$

Values for the various molecular parameters appearing in Equation (2.29) for iodine are given in Appendix A. For reference purposes it is of value to note that for the iodine transition of interest in this work, the fractional population in the initial absorbing level is 0.34 % of the total molecular population at room temperature. At 70 K (the temperature in a compressible flow at Mach 4 with a room temperature reservior) the fraction increases to 1.9 % as the vibrational and rotational populations move to lower quantum numbers with decreasing temperature.

Substituting the above expressions into Equation (2.24) for the fluorescence signal, we find that the fluorescence is a complicated function of pressure and temperature in a compressible flow. We explore next an approach that allows a great simplication in this equation so that the signal can be directly related to the iodine number density without additional measurements or corrections.

2.3.3 Asymptotic (Large Frequency Detuning) Solution

The term in Equation (2.24) that most complicates the discussion of the pressure and temperature dependence of the fluorescence signal is the Voigt integral. If this integral could be simplified, perhaps an equation would result that would make the pressure and temperature dependence easier to understand. There are two parameters in the Voigt integral, the broadening parameter, B', and the detuning parameter, D. The broadening parameter is determined by the gasdynamic conditions of the flow. Without changing the parameters of the flowfield, the only way to change B' is by saturation, or power broadening, of the the transition. The saturation approach is discussed fully in the next section.

The other option available to the experimentalist is to change the detuning parameter, D, by detuning the narrow bandwidth laser away from the line center of the transition. In the asymptotic limit of large frequency detuning, the Voigt integral becomes [21]

$$\lim_{D \gg 1} V(D, B') = \frac{1}{\sqrt{\pi}} \frac{B'}{D^2 + B'^2} . \tag{2.30}$$

Assuming that the laser intensity is much less than the saturation intensity, $I \ll I^{sat}$, Equation (2.24) becomes

$$\lim_{\substack{D \gg 1 \\ I \ll I^{sat}}} S_F = C \frac{1}{A_{21} + Q} \frac{\Delta\nu_c}{4\Delta\nu^2 + \Delta\nu_c^2} f_1 N_{I_2} , \tag{2.31}$$

where

$$C = \eta h\nu \frac{\Omega}{2\pi^2} V_c \frac{B_{12}}{c} I A_{21}$$

is a constant (independent of temperature and pressure) and

$$\Delta\nu = \nu - \nu_L$$

is the laser detuning from the line center of the transition.

The equation is therefore simplified so that the pressure and temperature dependences are now clearly evident. Consider for a moment an experiment in a static cell with the temperature held constant and a narrow bandwidth laser detuned far enough for the asymptotic form, Equation (2.31), to be used. The quenching rate, Q, and the collision width, $\Delta\nu_c$, both vary linearly with the total pressure in the cell. At very low pressures we have $Q \ll A_{21}$, and the fluorescence signal increases linearly with pressure due to the pressure broadening term in the numerator (the collisional linewidth in the denominator is dominated by the laser detuning). At

higher pressures the quenching becomes larger than the spontaneous emission rate and, until the collision width in the denominator ceases to be negligible, the pressure dependence of the quenching is cancelled by the pressure broadening. In this range the signal is independent of the total pressure in the cell and directly proportional to the iodine number density. At still higher pressures the laser detuning starts to become negligible in the denominator and the signal then varies as the inverse square of the pressure.

Now consider a gasdynamic experiment. The pressures of interest in most gasdynamic situations are such that the quenching dominates the spontaneous emission rate, $Q \gg A_{21}$. If the narrowband laser is now detuned enough to make the collision width in the denominator negligible with respect to the laser detuning, $\Delta\nu \gg \Delta\nu_c/2$, the fluorescence signal becomes

$$S_F = C' f_1 N_{I_2}\,, \tag{2.32}$$

where, on using (2.27) and (2.28), we define

$$C' = C\frac{C_b}{C_q}\frac{1}{4\,\Delta\nu^2}\,.$$

Therefore, for sufficient detuning and pressures of interest in gasdynamics, the fluorescent signal is independent of pressure and depends on temperature only through the population factor f_1. The laser detuning has allowed a cancellation of the collisional quenching by the collisional broadening in the fluorescence expression. Thus, the fluorescence signal can now be easily related to the desired iodine number density using a very simple equation. This approach is considered to be an *extremely* interesting one in the usual situation where saturation is not practical. The obvious drawback to the use of large frequency detuning is that the signal decreases like $1/\Delta\nu^2$ (see the constant C' above). In the experimental section of this work this

approach is examined for the case of the iodine molecule to determine the amount of detuning needed in a real situation and the level of the signal strength that results.

A brief comment is in order concerning the remaining temperature dependence in Equation (2.32) above. The population factor f_1 depends on temperature as given in Equation (2.29). (Note the assumption that one may use the Boltzmann factor is very good in the limit $I \ll I^{sat}$.) It is possible to choose a molecular transition that will minimize the temperature dependence of this population factor. The desired value of the angular momentum quantum number, J, that will give a minimum temperature dependence is found by setting the derivative of Equation (2.29) with respect to temperature equal to zero. The equation for this J value is then given by

$$J^2 + J - \frac{k\overline{T}}{B} = 0, \tag{2.33}$$

where $\overline{T}$ is the mean temperature. Desired values for J at various mean temperatures are considered for the case of iodine in Appendix A.

The remaining section of this chapter will focus on the theoretical aspects of saturation by a broadband laser. Complications that arise in the practical situation will also be considered. In subsequent chapters the two approaches will be investigated experimentally.

2.4 Saturated Laser–Induced Fluorescence with a Broadband Laser

2.4.1 Iodine Saturation: Ideal Case

In this section the objective is to concentrate on the behavior of the fluorescence signal as the laser intensity approaches or exceeds the saturation intensity of the molecular transition, for the case of a broadband laser. The derivation of the

previous section applies to the case of excitation by a narrow bandwidth laser. The question naturally arises as to the difference in the behavior of the fluorescence signal in the saturated limit if the laser bandwidth is not negligible with respect to the molecular linewidth. It is easiest to study this question by first examining the expression for the fluorescence signal in the limit of a broadband laser. The derivation will start with a form of the stimulated rate coefficient, b_{ij}, appropriate to the case of a broadband laser. At the end it will be demonstrated that the solution is consistent with the narrow bandwidth solution in the appropriate limit. The differences between saturation with a broadband and a narrowband laser will also be discussed.

If the laser bandwidth is much larger than the molecular linewidth then the details of the line–broadening processes are not important. In effect the molecular lineshape is integrated by the broad laser spectral width. For this situation the stimulated rate coefficient, b_{ij}, is written as [24]

$$b_{ij} = \frac{1}{c} B_{ij} I_\nu \,, \tag{2.34}$$

where $I_\nu = I/\Delta\nu_L$ is the laser intensity per unit bandwidth and $\Delta\nu_L$ is the laser bandwidth. The molecular lineshape is thus replaced by the dominant laser bandwidth in this formulation. Solving the rate equations, (2.5) and (2.6), in steady state, with (2.11) and this expression for the stimulated rate coefficient, yields for the excited state number density

$$N_2 = \frac{1}{c} \frac{B_{12}}{A_{21} + Q} \frac{I_\nu}{1 + I_\nu / I_\nu^{sat}} f_1 N_{I_2} \,, \tag{2.35}$$

where the saturation intensity is defined, per unit bandwidth, as

$$I_\nu^{sat} = c \frac{A_{21} + Q}{B_{12}} \frac{1}{f_1 + f_2 g_1 / g_2} \,. \tag{2.36}$$

Substituting this expression into Equation (2.23) and assuming uniform excited state population over the observation volume (this assumption will be examined in the next subsection) gives the the following expression for the fluorescence signal

$$S_F = \eta h\nu \frac{\Omega}{4\pi} V_c \frac{A_{21}}{A_{21}+Q} \frac{B_{12}}{c} \frac{I_\nu}{1+I_\nu/I_\nu^{sat}} f_1 N_{I_2} . \tag{2.37}$$

The limiting form of Equation (2.37), both for small and large laser intensities, is of interest in this section. In the limit of small laser intensity, $I_\nu \ll I_\nu^{sat}$, the fluorescence signal becomes

$$S_F = \eta h\nu \frac{\Omega}{4\pi} V_c \frac{A_{21}}{A_{21}+Q} \frac{B_{12}}{c} I_\nu f_1 N_{I_2} . \tag{2.38}$$

Although the expression containing I_ν is simplified, the complication concerning the Stern–Volmer factor is still present. This is the usual problem in using laser–induced fluorescence to measure the number density of the fluorescing molecule: corrections must be made to the fluorescent signal for the collisional quenching. Pressure and temperature must also be measured (in order to calculate the collision number of the excited state molecule with other molecules) and the collisional cross–section must be known.

Various approaches have been proposed to avoid the need for quenching corrections [26] but the most desirable, theoretically, has been saturation. In the fully saturated limit, $I_\nu \gg I_\nu^{sat}$, the fluorescence signal is given by

$$S_F = \eta h\nu \frac{\Omega}{4\pi} V_c A_{21} \frac{f_1}{f_1 + f_2 g_1/g_2} N_{I_2} . \tag{2.39}$$

Therefore, in the saturated limit, the fluorescent signal is directly related to the number density, except for the temperature dependent population factor, f_1. The quenching dependence is completely removed by the saturation! This is an extremely interesting result and is the reason for much interest in saturated laser–induced fluorescence in recent years (see [24], for example). It is interesting to

compare this expression with Equation (2.32). The fluorescent signal in either the asymptotically–large detuning or in the saturation limit is independent of pressure and temperature, except for the population factor. Thus, both approaches are attractive for the measurement of number density, but there are disadvantages to each approach. The detuning approach yields a weaker signal and it varies linearly with laser intensity. The saturated signal is stronger and is independent of the laser intensity. However, the detuning limit may be more easily approached in practice, while full saturation of a molecule under gasdynamic conditions is difficult, if not impossible, to achieve. If partial saturation can be achieved, the number density can be determined by a measurement of the fluorescent signal at several laser intensities [27]. However, this technique limits the measurement to the time–averaged number density and assumes illumination by a uniform intensity, not a Gaussian laser beam. (This complication will be addressed momentarily.) The practical application of the saturation approach in the use of laser–induced iodine fluorescence will be examined in the next chapter.

The equations above express the results of saturation with a broadband laser in the ideal case. Several complications arise in the real case and these must be considered. The next section is devoted to a major complication that arises due to the laser intensity distribution. Before completing this section, however, we must consider the situation that arises if the laser bandwidth is not truly broadband, that is, if the laser bandwidth does not greatly exceed the molecular linewidth. What criterion can be used to decide when the broadband expression can be used to describe the saturation process and how do we theoretically treat the case when the broadband expression does not strictly apply? To answer these questions, let us examine the homogeneous form of the narrowband result, Equation (2.25), in the saturation limit. It is easily seen that the saturated fluorescent signal is given by an expression that is *exactly* the same as Equation (2.39), the saturation limit of the

broadband result. Therefore, if the transition is strongly homogeneously broadened, the narrowband and broadband developments agree (except for a slight difference in the definition of the saturation intensity, which will be considered momentarily). The reason the broadband expression agrees with the homogeneous limit of the narrowband expression is that the laser bandwidth adds to the collision linewidth to give the total homogeneous linewidth, as discussed in Reference 22. Therefore, a large laser bandwidth causes the homogeneous linewidth to greatly exceed the inhomogeneous, or Doppler, linewidth, and the homogeneous limit is obtained. We can write an approximate expression for calculating the total homogeneous linewidth that will illustrate that the saturation intensities also agree in the homogeneous limit. When considering the general case of a laser of arbitrary bandwidth, one must convolve the laser spectral distribution with the Lorentzian distribution in the stimulated rate coefficient, as given by Equation (2.8) [22]. In the usual case of a Gaussian laser spectral distribution, an approximate formula for the linewidth that results from the convolution of a Gaussian distribution with a Lorentzian distribution is given by [28]

$$\Delta\nu_H = \sqrt{\Delta\nu_L^2 + \Delta\nu_c^2},$$

where $\Delta\nu_H$ is the total homogeneous linewidth. However, in this section, we have been considering a broadband laser, that is, one whose spectral distribution is rectangular, with width $\Delta\nu_L$. The corresponding collision linewidth that must be used in the above equation is the width of a rectangle, having an area of unity and a height which is the value of the Lorentzian at its center, $2/\pi\,\Delta\nu_c$. This effective width is just $\pi\,\Delta\nu_c/2$. Therefore, the approximate expression that will be used for the total homogeneous linewidth is given as

$$\Delta\nu_H = \sqrt{\Delta\nu_L^2 + (\pi\,\Delta\nu_c/2)^2}. \tag{2.40}$$

We now see that if the saturation intensity is written as

$$I^{sat} = c\,\Delta\nu_H \frac{A_{21}+Q}{B_{12}} \frac{1}{f_1 + f_2 g_1/g_2}, \tag{2.41}$$

then Equation (2.13) is recovered in the narrowband limit and Equation (2.36) is obtained in the broadband limit. The criterion that can be applied for use of the broadband expression is, therefore, that the total homogeneous linewidth must be much larger than the Doppler linewidth, $\Delta\nu_H \gg \Delta\nu_D$. If this inequality holds, Equation (2.39) may be used to describe the saturation process, with the saturation intensity given by Equations (2.40) and (2.41).

An interesting observation can be made concerning the implication of Equation (2.41) for the saturation process. When inducing a molecular transition with a narrow bandwidth laser, the appropriate linewidth in the expression for the saturation intensity is the molecular collision width. If a broadband laser is employed, the laser bandwidth appears in the saturation intensity expression. In attempting to saturate a molecular transition, one would like to decrease the saturation intensity, if possible. One way to do this would, therefore, be to decrease the bandwidth of the laser. However, once the laser bandwidth becomes equal to the collision width of the transition, further reduction of the laser bandwidth will not cause further reduction of the saturation intensity.

The purpose of the saturation studies in this work is to measure the saturation intensity of the iodine molecule at the pressures of interest in gasdynamics (usually 100 torr to 1 atmosphere) and to evaluate the effectiveness of the saturation approach in eliminating the need for quenching corrections. For the pressure range of interest and for the bandwidth of the laser employed in the saturation studies in this work, the total homogeneous width varied from about 10 to 40 times the Doppler width. Therefore, in this work the iodine transition is always *predominately* homogeneously broadened and the broadband expression can be utilized with good

accuracy to describe the saturation process. The broadband expression is expected to be a better approximation at larger pressures and this will be seen to be the actual case in the next chapter. However, the effect of variable molecular lineshape is important to the saturation process (discussed in reference to Equations (2.25) and (2.26)) and must be included if the transition is only predominately homogeneously broadened. For a strongly homogeneous transition, Equation (2.25) shows that the saturated signal is completely independent of the laser intensity. However, for a strongly inhomogeneous transition, the saturated fluorescent signal varies as the square root of the laser intensity, according to (2.26). This effect can be included, in an approximate way, in the broadband laser equations of this section by writing Equation (2.35) for the excited state population as

$$N_2 = \frac{1}{c}\frac{B_{12}}{A_{21}+Q}\frac{I_\nu}{(1+I_\nu/I_\nu^{sat})^\alpha} f_1 N_{I_2}, \tag{2.42}$$

where α varies from 1 (homogeneous limit) to 0.5 (inhomogeneous limit). This equation can then be inserted into Equation (2.23) to give the corresponding fluorescence signal. The expression will turn out to be very useful in describing the saturation experiments of later sections when the laser bandwidth is large enough to enable the use of the broadband equations of this section but not so large as to totally dominate the molecular line broadening effects in the saturation limit.

If one is interested in studying the effects of saturation in the case when the transition is not predominately homogeneous (which occurs if both the laser bandwidth and the collision width are small compared to the Doppler width), the effects of non–negligible laser bandwidth can be included as follows. One must start with the narrowband laser expression for the stimulated rate coefficient, Equation (2.8), and convolve the laser spectral distribution with the Lorentzian distribution. One next proceeds with the development of Section 2.3 and convolves the homogeneous response with the inhomogeneous distribution, due to Doppler

broadening. The resulting expression involves nested convolutions, but could be numerically integrated to yield the fluorescent signal in the general case of arbitrary laser bandwidth and arbitrary molecular broadening. For the purposes of this work, this complexity is not required in evaluating the results of the saturation experiments.

2.4.2 Iodine Saturation: Gaussian Beam Complication

The previous derivations have assumed that the excited state population is uniform over the observation volume. In that case the integration of this population over the volume in Equation (2.23) becomes simply the product of the population and the observation volume. This case would apply if the laser intensity were uniform over the observation volume. This is a valid assumption in the dimension along the laser beam since only a small segment at the beam focus, about one confocal parameter, is collected by the optics. However, in the transverse dimension the laser intensity distribution is usually Gaussian shaped and not at all uniform, as previously assumed. The effect of this Gaussian transverse intensity distribution on the saturation process was first studied by Daily [24] and is considered here for the case of iodine.

The Gaussian transverse distribution of a laser beam, for the case of the fundamental TEM_{00} transverse mode (higher order transverse modes are not desired if saturation is the goal), is given by

$$I_\nu(r) = I_\nu^o \exp\left(-2r^2/\omega^2\right), \tag{2.43}$$

where I_ν^o is the intensity at the beam center and ω is the beam radius. Substituting this expression into Equation (2.35) shows that the excited state population is now a function of the transverse radial coordinate, r. We then substitute this radially-dependent population into the expression for the fluorescent signal, Equation (2.23),

and find that

$$S_F = \eta h\nu \frac{\Omega}{4\pi} \frac{A_{21}}{A_{21}+Q} \frac{B_{12}}{c} f_1 N_{I_2} \int_0^\infty \frac{I_\nu^o \exp\left(-2r^2/\omega^2\right)}{1+(I_\nu^o/I_\nu^{sat})\exp\left(-2r^2/\omega^2\right)} 2\pi\,\delta\, r\, dr\,, \tag{2.44}$$

where δ is the length of the observation volume along the laser beam. This integration is easily performed to give

$$S_F = \eta h\nu \frac{\Omega}{4\pi} V_c A_{21} \frac{f_1}{f_1 + f_2 g_1/g_2} N_{I_2} \ln\left(1 + I_\nu^o/I_\nu^{sat}\right), \tag{2.45}$$

where the observation volume is given by $V_c = \delta\pi\omega^2/2$ and $\pi\omega^2/2$ is the laser beam area.

It is now instructive to examine the limiting forms of this equation. In the limit of low laser intensity, $I_\nu^o \ll I_\nu^{sat}$, Equation (2.38) is recovered. However, in the saturated limit, $I_\nu^o \gg I_\nu^{sat}$, the fluorescence signal saturates logarithmically as

$$S_F = \eta h\nu \frac{\Omega}{4\pi} V_c A_{21} \frac{f_1}{f_1 + f_2 g_1/g_2} N_{I_2} \ln\left(I_\nu^o/I_\nu^{sat}\right). \tag{2.46}$$

It is thus seen that when attempting to saturate with a Gaussian laser beam, even in the fully saturated limit, the signal still depends on the laser intensity and that, due to I_ν^{sat}, the pressure and temperature dependence of the signal is not removed in the saturated limit. This is a practical and unfortunate complication in the saturation approach. It is important to note that this complication does not arise in the detuning approach, which was discussed in the previous section, since the laser intensity distribution is of no consequence as long as the intensity at the beam center is less than the molecular saturation intensity.

The above equations treat the Gaussian beam effect for the situation when the laser bandwidth is very large so that the homogeneous limit strictly applies. If the

laser employed in the saturation experiment has a bandwidth that is large enough to make the transition predominantly homogeneous, but not strongly so, then, as shown above, the effects of the molecular lineshape variation on the saturation behavior can be accounted for in an approximate way by the use of Equation (2.42) for the excited state number density. The real value in using this approximation instead of the exact approach of convolving the laser and molecular spectral distributions is that the very important Gaussian beam effect can then be treated in a closed analytical form.

Using this approximation for the excited state population and the Gaussian beam dependence of Equation (2.43), Equation (2.23) can then be integrated over the observation volume to give the fluorescence signal as

$$S_F = \eta h\nu \frac{\Omega}{4\pi} V_c A_{21} \frac{f_1}{f_1 + f_2 g_1/g_2} N_{I_2} \frac{1}{1-\alpha}\left[\left(1 + \frac{I_\nu^o}{I_\nu^{sat}}\right)^{1-\alpha} - 1\right]. \qquad (2.47)$$

This equation looks different from any of the previous equations but can be shown to be correct in the appropriate limits. In the homogeneous limit, $\alpha = 1$, it is easily seen that, using l'Hôpital's rule to evaluate the indeterminate expression, the homogeneous Equation (2.45) is recovered. In the limit of low laser intensity, Equation (2.47) reduces to Equation (2.38). In the saturated limit, Equation (2.46) results in the homogeneous case and the square root intensity dependence is obtained for the inhomogeneous limit. This expression is, therefore, a useful analytical expression that may be used to describe the saturation process, including the Gaussian beam effect, as long as the transition is predominately homogeneously broadened.

Chapter 3

Saturation of Iodine Fluorescence by a Multimode Argon Laser: Experiment and Results

3.1 Introduction

The objective of this chapter is to investigate the use of saturation for eliminating the need for quenching corrections when using laser–induced fluorescence to measure number density. As discussed in the introduction, iodine is a good choice for a seed molecule for these investigations due to its convenient visible absorption spectrum. In addition, it is pointed out in Appendix A that iodine is a good candidate molecule for saturation studies since estimates of the saturation intensity in the appendix show a predicted variation from about 2.2×10^4 watts per square cm at a pressure of 100 torr to about 1.5×10^5 watts per square cm at 800 torr. These intensities are readily obtainable with current cw lasers, focused to a small spot. Other molecules one might consider for use in making density measurements, such as biacetyl, have saturation intensities about four orders of magnitude larger than iodine, as also pointed out in Appendix A.

The laser source chosen for the saturation experiment is the argon laser. The 5145 Å argon line was employed since it is very intense and its gain profile coincides with several iodine transitions, as discussed in Appendix A. The laser was run

without a line–narrowing element (referred to as an etalon); for this case and the laser employed in this experiment the output consisted of many axial cavity modes, spaced by about 83 MHz over a 10 GHz wide gain profile. The laser spectral distribution was, thus, essentially continuous, with a bandwidth of about 5 GHz (FWHM), which is more than 10 Doppler widths for iodine at room temperature (see Appendix A). Therefore, the iodine transition is predominately homogeneously–broadened, even at very low pressures, and the broadband fluorescence expressions of the previous chapter can be used to explain the experimental results. The overlapping P13–R15 transitions contribute essentially all the fluorescence, since the other transitions mentioned in Appendix A are either at the extreme edge of the laser gain profile, and, therefore, see little laser intensity, or are hot–band transitions, and are, thus, very weak at room temperature.

In the next section, the experimental apparatus is described. Following that section is a discussion of the experimental procedure and the data collected. Next, the data are analysed and compared with the broadband fluorescence theory. Finally, a discussion is given of the results of the saturation experiment, of the values of measured parameters of interest, such as the saturation intensity, and of the effectiveness of the saturation approach in eliminating the quenching complication.

3.2 Experimental Apparatus

A diagram of the experimental setup is given in Figure 2. The laser source used was a Coherent Radiation Model CR–18 argon laser. The laser was run without an etalon, giving a multimode output with a bandwidth of about 5 GHz (FWHM). There are two reasons for carrying out the experiment with the laser running multimode instead of single–mode. The first is the tradeoff between output power and bandwidth. The output power is lowered by a factor of about two when the etalon is inserted into the laser cavity and maximum intensity is desired in the

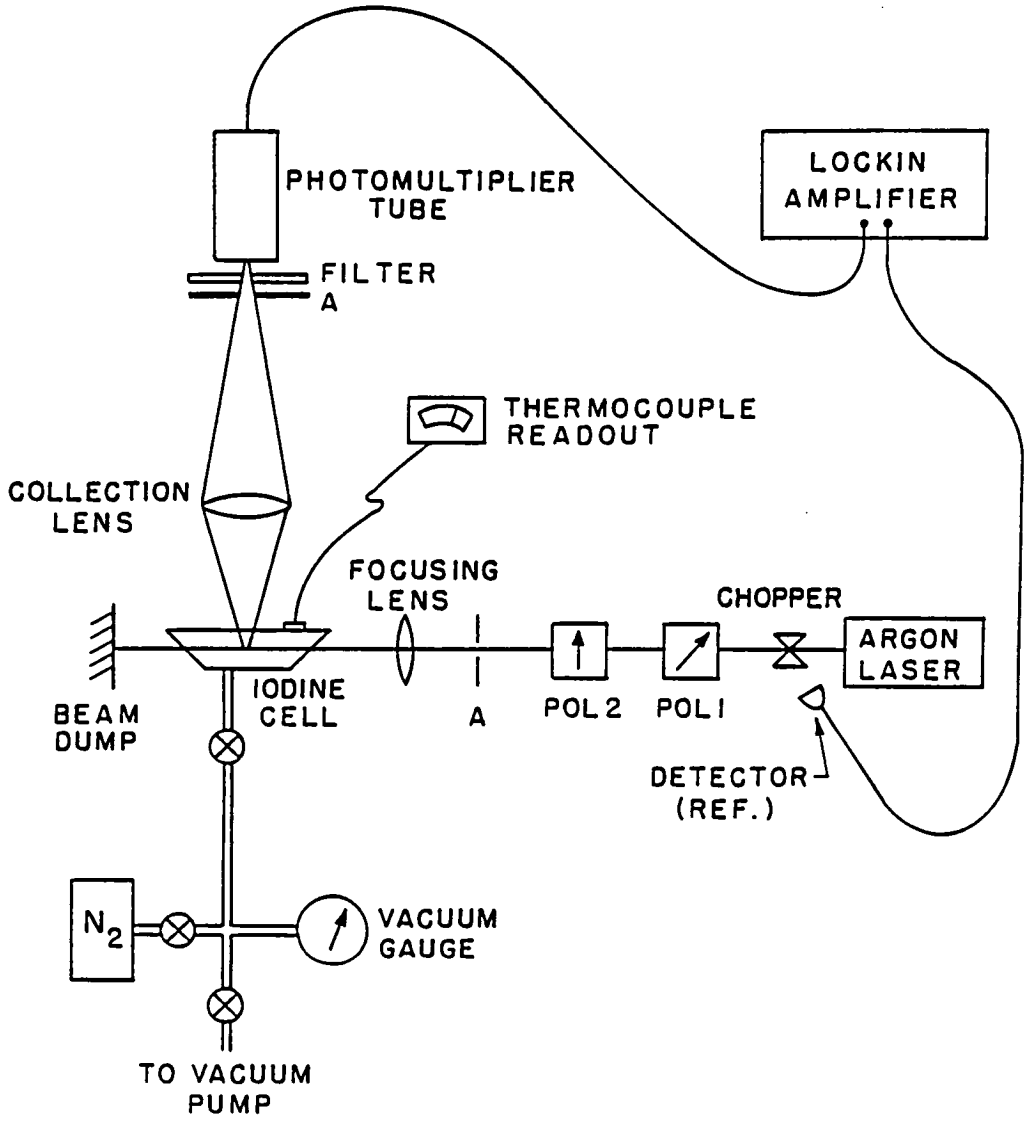

Fig. 2. Experimental Setup for the Saturation Studies

saturation experiments. However, we might recall from the previous chapter that the saturation intensity is lowered as the laser bandwidth is decreased. Noting that an etalon gives a single–mode linewidth of about 20 MHz, or 250 times less than the multimode bandwidth, it might appear the maximum value of I/I^{sat} would be 150 times larger for the single–mode operation than for multimode operation. This

is not entirely correct since it should be remembered that the total homogeneous linewidth is the term that appears in the expression for the saturation intensity (see Equation (2.41)). At 500 torr, an intermediate pressure in our experiment, the collision width is 6 GHz, greater than the multimode bandwidth. Therefore, decreasing the laser bandwidth reduces the saturation intensity only slightly (about 12 % at 500 torr). It is, thus, more desirable to run the laser multimode and make use of the factor of two increase in output power. The second reason is an important practical consideration. The saturation measurements are very time–consuming and the long–term frequency and power stability is much harder to maintain with an etalon in the cavity, due to the frequency drifts associated with an etalon. The experiment is, therefore, much more difficult to carry out if the laser is required to run single–mode, since one must carefully monitor the frequency and power drifts and correct the data whenever these occur. In the next chapter, we discuss single–mode experiments, but, fortunately, the procedure in that case is far less time–consuming than in the case of the saturation measurements.

The transverse mode quality of the laser beam is extremely important when focusing the beam down to a very small spot in order to achieve large intensities. Therefore, the internal aperture in the laser cavity was decreased in size until the higher–order transverse modes (which have a larger spatial extent) were totally rejected and the output was purely the fundamental TEM_{00} mode. In doing this, the output power was decreased somewhat and, for the laser used in this experiment, 3.4 watts was the maximum power available with optimum alignment of the laser cavity. For the tight focusing employed in the experiment, this power produced a maximum of about 4×10^6 watts per square cm, which was sufficient for the saturation studies.

In studying the saturation process, one would ultimately like a plot of fluorescent signal strength versus laser intensity, for various total pressures. The next

element needed in the experimental setup is, then, a device for attenuating the laser power. An alternate approach would be to change the focused spot size of the laser beam, but this would require realignment of the optics and is, therefore, less desirable. Since the laser output is linearly polarized, an efficient way to obtain attenuation is through the use of polarizers. A Glan–Air polarizer is a calcite crystal, cut parallel to the optic axis, which can be rotated to achieve varying attenuation (see Reference 29 for a complete description). Since the laser was not perfectly polarized, two such polarizers were employed, as shown in Figure 2, to increase the range of attenuation. It was found that this method gave more than five orders of magnitude of power attenuation with minimal beam steering. The polarizers were aligned as follows. Polarizer 2 was rotated for maximum power transmission and its angle fixed. Polarizer 1 was then inserted in the beam and aligned for maximum transmission, giving a maximum throughput of 78 % with both polarizers aligned with the laser polarization. Polarizer 1 could then be rotated to achieve more than five orders of magnitude power attenuation, as measured by a sensitive power meter. The rotation angle of polarizer 1 was calibrated versus transmitted power for ease in attenuation during the course of the experiment. However, whenever the laser cavity was aligned to optimize the output power, the laser beam pointing changed slightly and the calibration of the polarizers had to be repeated. It was confirmed that the attenuation varied as $\cos^4\Theta$, where Θ is the angle of the polarizer with respect to the laser polarization, as expected for two polarizers in series. It should be noted that it was essential to fix the angle of polarizer 2 and rotate polarizer 1 so that the transmitted laser beam was always of the same polarization. This was important since the reflection from optical elements beyond the polarizers, such as the Brewster angle window on the iodine cell, was a function of polarization and the actual power delivered to the iodine molecules would not be that given by the calibration of the crossed polarizers if polarizer 2 were rotated. A 5 mm diameter

aperature was used to block stray light scattered by the polarizers.

The beam was focused to a spot by a 5.1 cm focal length lens. The spot size was both calculated, using the laser beam parameters, and measured with a linear Reticon array detector. The two methods agreed well and showed the focused spot size to be 6 μm. This value is used in later calculations of the focused intensity. Reflection from the lens and from the cell window were measured and included in the calculation of the focused laser intensity inside the iodine cell.

A glass cell with Brewster angle windows to minimize reflection losses was placed at the beam focus. The cell contained a few iodine crystals and a valve for sealing off the contents of the cell. A thermocouple was placed on the cell to monitor the temperature of the crystals, since this determined the iodine vapor pressure in the cell. A gas-handling system was connected to the iodine cell to enable the cell to be filled with nitrogen at various pressures, as monitored by a vacuum gauge. The saturation experiments were all performed with a fixed iodine partial pressure of 0.3 torr at room temperature and various nitrogen pressures.

The iodine fluorescence was collected at 90 degrees to the laser beam by a 5 cm diameter lens with a focal length of 8 cm. The lens was placed 10.2 cm from the laser beam and aligned on the focal region. An aperature was placed 36.8 cm behind the collection lens and set for a diameter of 1.6 mm. Using the Gaussian lens formula [29], the magnification of the object at the aperature plane was calculated to be 3.6, in agreement with the measured magnification. The aperature size was chosen so that the fluorescence was collected from about one confocal parameter length of the focused beam. The confocal parameter is defined as twice the Rayleigh range of the Gaussian beam. The Rayleigh range is the distance from the focal plane to the plane at which the beam area has doubled and is given by $\pi\omega_o^2/\lambda$ [30], where ω_o is the focused spot size and λ is the laser wavelength. For a spot size of 6 μm and the 5145 Å wavelength, the confocal parameter is 440 μm. Applying the

magnification ratio of 3.6 shows that the magnified confocal parameter was 1.58 mm, so that the aperature passed fluorescence from approximately one confocal parameter at the focus of the laser beam. The fluorescence was then filtered by a 540 nm long pass filter to block scattered laser light, while passing the iodine fluorescence at wavelengths longer than 540 nm. The detector used was an Amperex photomultiplier tube with a photocathode that had a good response in the red part of the spectrum, where most of the iodine fluorescence is found at high pressures. The output of the detector was sent to a PAR lock–in amplifier. This amplifier provided the capability of phase–sensitive detection, which allowed the detection of extremely low fluorescent signal levels. The laser beam was chopped at 175 Hz and a reference detector was used to provide the reference signal to the amplifier for phase–sensitive detection. With this detection scheme the lowest fluorescent signals detected were still 10 times larger than the background limit set by fluorescence from the laser plasma tube, fluorescence from the long–pass filter (induced by the scattered laser light) and residual scattered light.

3.3 Experimental Procedure and Results

The experimental procedure for the collection of the saturation data consisted of the following. The argon laser was adjusted for maximum output power, consistent with good transverse mode quality (determined by adjustment of the internal aperature). The crossed Glan–Air attenuators were calibrated with a sensitive power meter so that desired transmitted laser intensities could be obtained by setting a predetermined polarizer rotation angle. The optics were aligned so that the beam focus occurred at the center of the iodine cell to optimize fluorescent signal collection. The collection lens was adjusted so that the image of the focal region coincided with the aperture in front of the photomultiplier tube. The detector was placed in a light–tight box so that light could enter only through the aperature.

The reference detector was positioned to receive reflected light from the chopper and the reference signal was established for the lock–in amplifier and its scales were calibrated. The output current of the photomultiplier tube was passed through a load resistor and the voltage across this resistor was provided as the signal for the lock–in amplifier.

In the initial stages of the experiment, difficulty was encountered with the long–term stability of the fluorescent signal. It was found that, if the iodine crystals were placed in a container outside the actual cell, their temperature could be well controlled by placing them in a constant temperature bath, but then diffusion times of the iodine vapor into the cell were prohibitively long, due partially to the small opening to the cell. However, if the crystals were inside the cell, the iodine vapor pressure was a sensitive function of the cell temperature, and this was determined by both the room temperature and by heating due to the laser beam. The best solution found was to place the crystals inside the cell and closely monitor the cell for temperature drifts. The laser beam heating effect was much smaller than room temperature drifts and is discussed below. Most of the data were collected late at night when the room temperature and laser cooling water temperature were more constant. The experiments discussed in the next chapter were carried out with an improved iodine cell which allowed the crystals to be placed inside the cell in a temperature–controlled bath and, in that case, room temperature changes did not affect the iodine vapor pressures. It was found that, if the crystals were placed in a clean cell, the fluorescent signal decayed until the iodine vapor coated the walls of the cell and, then, reached a steady–state vapor pressure in equilibrium with the crystals and the cell walls. Therefore, the crystals were placed in the cell the night before experiments were to be performed and the signal was checked for constancy before experiments were begun.

With the preliminary setup complete, the experiments were carried out as

follows. The gas lines connecting the nitrogen bottle, the vacuum gauge, the iodine cell and the vacuum pump were purged and evacuated. The vacuum pump was then isolated, the valve to the iodine cell opened and nitrogen added to the iodine in the cell to 800 torr total pressure, the highest pressure employed in these experiments. The cell valve was then closed and the iodine–nitrogen mixture allowed to mix until a constant fluorescent signal was obtained. At this point the experiment was set to begin. The attenuator was set for maximum power and a voltage was recorded on the lock–in amplifier, corresponding to the fluorescent signal from the iodine vapor in a background pressure of 800 torr nitrogen. The attenuator was then adjusted for lower laser intensity and the correspondingly lower signal level was recorded.

At this point the difficulty due to the very slight change in cell temperature (about 0.5 degrees, as recorded by the thermocouple) on the iodine vapor pressure and, therefore, on the signal level must be discussed. As the laser power is reduced the power absorbed by the glass cell and, to a lesser extent, by the iodine molecules, caused the glass and, therefore, the iodine crystals to cool slightly. Therefore, the iodine vapor pressure decreased slightly as the laser was attenuated, causing the fluorescent signal to decay slightly with time after attenuation. When the laser power was increased to the original level, the signal slowly increased to the original reading. The time constant for this process was on the order of minutes and, as the experiment should ideally be carried out as quickly as possible in order to minimize laser power and room temperature drift effects, the following experimental technique was employed to minimize the laser heating effects on the experimental data. The laser power was initially set at the maximum level and the fluorescent signal level checked. Next, the laser power was attenuated to the desired level and a reading of the fluorescent signal corresponding to that laser intensity was recorded, before significant cooling could occur. The maximum laser power was then reset and the signal level recorded immediately, before the increase to the steady–state value

occurred. The value used for the fluorescent signal corresponding to the reduced laser intensity was the actual signal recorded at that reduced level, adjusted by the ratio of the initial steady-state signal at maximum intensity to the reading recorded immediately after the laser power was readjusted to maximum. Using this procedure, the data were all recorded at essentially constant temperature, and the effect of heating due to the varying laser intensity was minimized. Before a reading was taken at the next laser intensity level, the signal was allowed to reach steady-state at the maximum laser power level. It was found that this procedure was extremely time-consuming, but was necessary in order to obtain consistent and repeatable data.

Once the fluorescent signals were recorded for the entire range of laser intensities at the 800 torr cell pressure, the cell was pumped down to 600 torr, resealed, and allowed to stabilize. The measurements were repeated as above, recording fluorescent signal versus laser intensity. The same procedure was repeated for cell pressures of 400, 200, 100, 50, and 0.9 torr total pressures. The linearity of the photomultiplier tube was checked often and found to be linear at all data points, except for the measurements at 0.9 torr, when the signals were the largest. For this set of measurements, a neutral density filter with a measured attenuation factor of 3.61 was employed to keep the photomultiplier tube in the linear regime. The data sets were repeated several times until the final set was obtained during the course of a single evening, when the laser output and the room temperature were very stable. After completing the data sets at the seven pressure levels chosen, the cell was pumped out and refilled to 800 torr and several data points were taken at this pressure level and each lower pressure level as a repeatability check. The data represented by the final set were repeatable to the accuracy shown in the subsequent listing.

The final set of saturation data that is used for subsequent evaluation is given

in Table 1. This table lists the fluorescent signal as recorded in mV on the lock–in amplifier at each laser intensity (in watts per square cm) at the beam focus, for the seven total cell pressures, in torr. The data table was normalized to account for slight laser power drifts that occurred during the time required to complete the measurements (using a nominal power level of 3.36 watts). The laser intensities were computed using the attenuation calibration, the laser beam focused spot size (6 μm) and the reflection losses that occurred between the attenuator and the iodine molecules inside the cell. This data set forms the basis for the subsequent analysis and discussion of the effects of saturation on the iodine fluorescent signal.

3.4 Analysis of Saturation Data

In this section we apply the theoretical development of Chapter 2 to the saturation data given in Table 1, in order to determine the effect of saturation on the iodine fluorescence in a laboratory situation. As mentioned previously, we apply the broadband laser expressions to analyse the data in this chapter since the bandwidth of the laser is more than 10 Doppler widths (at room temperature) and, therefore, the total homogeneous width, given by Equation (2.40) is 10 to 40 times the inhomogeneous, or Doppler, width. Thus, the broadband, or homogeneous, formulas of Section 2.4 will be employed throughout this analysis.

The data of Table 1 are plotted in Figure 3, for the pressure range of 200 to 800 torr, the range of greatest interest in gasdynamics. The first feature to be noticed from the data is that the fluorescent signal does become nonlinear at laser intensities of about 3×10^4 watts per square cm. Therefore, some saturation effects are clearly taking place above this intensity. The next feature that is obvious from the figure is that saturation is not complete at the highest intensities employed in the experiment. We recall from Chapter 2, Equation (2.39), that in the homogeneous limit represented by that equation, the signal should become independent of laser

Table 1

Flourescent Signal (in millivolts) at Measured Laser Intensities (in watts per square cm) and Total Cell Pressures (in torr)

Intensity	800 torr	600 torr	400 torr	200 torr	100 torr	50 torr	0.9 torr
3.88×10^{6}	10.3	16.0	22.8	52.3	143.	352.	1550
3.46×10^{6}	10.0	15.2	21.9	50.3	139.		
3.00×10^{6}	9.30	14.4	20.6	48.7	136.	331.	1410
2.52×10^{6}	8.70	13.6	19.4	46.6	131.		
2.04×10^{6}	7.90	12.6	18.3	44.1	125.	297.	1200
1.16×10^{6}	6.34	10.2	15.8	37.4	107.	240.	910.
5.16×10^{5}	4.66	7.55	11.8	28.7	77.0	158.	552.
1.76×10^{5}	2.86	4.60	7.13	16.7	40.7	71.1	239.
1.31×10^{5}	2.51	3.95	6.10	13.8	32.6		
9.92×10^{4}	2.12	3.30	4.94	11.1	26.2	44.0	142.
7.68×10^{4}	1.72	2.66	4.10	8.74	19.7		
4.91×10^{4}	1.32	1.99	2.97	6.33	14.4	22.9	69.3
3.19×10^{4}	.891	1.42	2.17	4.42	10.0		
1.93×10^{4}	.626	1.01	1.47	3.09	6.41	10.1	29.5
1.29×10^{4}	.416	.633	1.00	2.02	4.37		
7.68×10^{3}	.244	.372	.588	1.22	2.54	3.75	11.6
4.64×10^{3}	.119	.206	.328	.707	1.44		

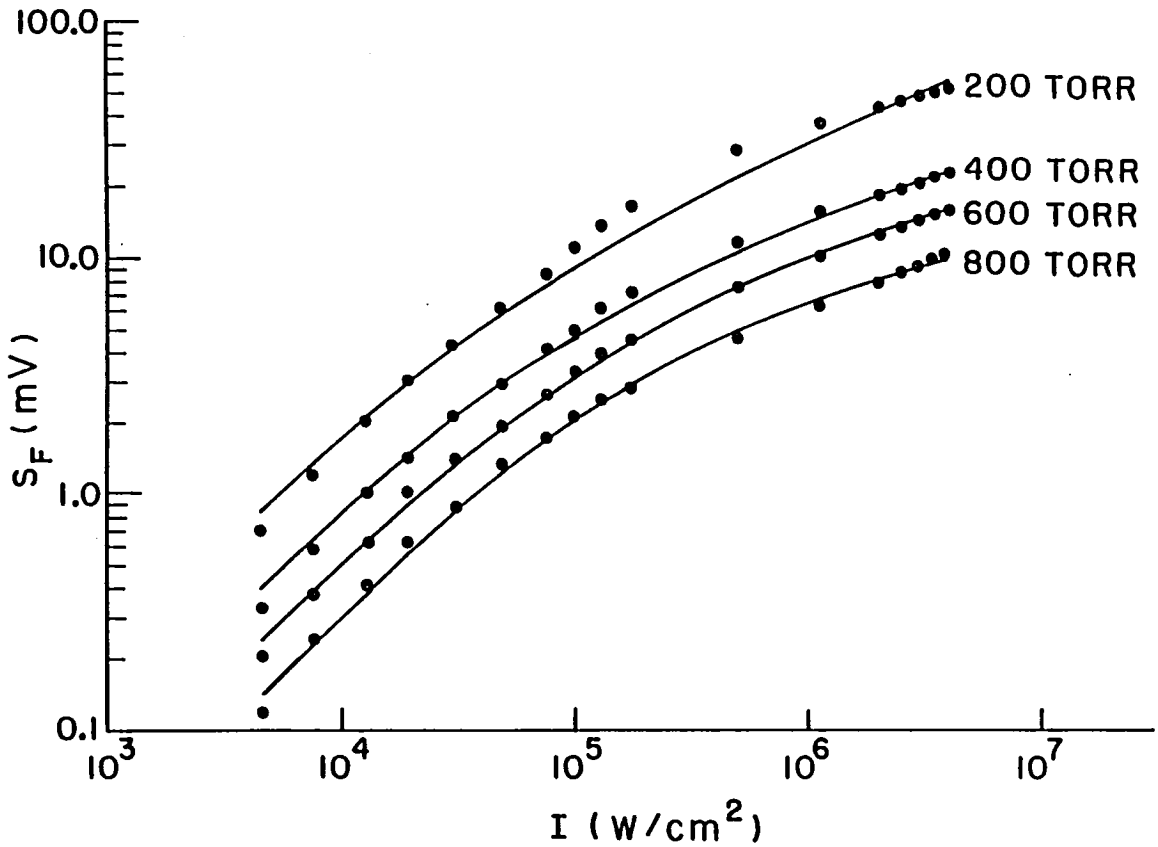

Fig. 3. Iodine Fluorescent Signal (in millivolts) versus Laser Intensity (in watts per square cm): Experimental Points and Theoretical Curves.

intensity, or have a slope approaching zero in Figure 3. This homogeneous limit is closely approached at the pressure of 800 torr where $\Delta\nu_H \approx 40\Delta\nu_D$, but there is still considerable slope in the data in this intensity range. This is precisely the Gaussian beam effect referred to in Section 2.4.2. It is, therefore, obvious that the effect of the transverse laser intensity distribution is of primary importance in describing the saturation effects exhibited by the data. Referring to Section 2.4.2, we see that there are two formulations that include the Gaussian beam effect: Equation (2.45) is employed when the homogeneous limit strictly applies, and Equation (2.47) is used as an approximate description of the effects of the molecular lineshape on

the saturation process when the transition is only predominately homogeneously broadened. We, therefore, expect Equation (2.45) to describe the data well at the highest pressures, but Equation (2.47) may be needed at the lower end of the pressure range of interest. The analysis is performed using both equations and the results compared.

We wish to compare the theoretical expressions with the data so that the saturation intensity may be deduced as a function of pressure, and to see if the theory includes all the physical phenomena of importance in the saturation process. The best way to make this comparison is to employ a numerical least–squares fitting routine to fit the theoretical expression to the experimental points. A grid search routine [31] was programmed in the Fortran language and the data were fit to the expressions given by Equations (2.45) and (2.47). In programming Equation (2.45), only one parameter, I_ν^{sat}, is a function of pressure (remember that f_2 is assumed to be pressure independent and that both temperature and N_{I_2} are constants in this static cell experiment). Therefore, for each curve at constant pressure, only a single parameter grid search routine was necessary. The resulting numerical fits using (2.45) were good at 800 torr but quickly deviated from the data at the lower pressures. In addition, the resulting saturation intensity did not decrease monotonically with decreasing pressure, as predicted in Chapter 2. The problem in using this expression is that the fit to the data for large laser intensities is poor for the lower cell pressures, since the assumption that the homogeneous limit strictly applies is less valid at these lower pressures. For the remainder of the discussion the expression given by Equation (2.47) will be used to analyse the data since the pressure range over which the homogeneous (or broadband) expression can be applied is greatly extended by the introduction of the parameter α. The resulting variation of the saturation intensity with pressure is then seen to agree with the predicted pressure dependence.

The equation to be used to explain the saturation data is rewritten from (2.47) as

$$S_F = \frac{A}{1-\alpha}\left[\left(1+\frac{I}{I^{sat}}\right)^{1-\alpha} - 1\right], \tag{3.1}$$

where

$$A = \eta h\nu \frac{\Omega}{4\pi} V_c A_{21} \frac{f_1}{f_1 + f_2 g_1/g_2} N_{I_2}, \tag{3.2}$$

and is assumed to be independent of pressure. This form of the equation is more convenient for the purposes of the analysis. It is seen that I_ν^o is replaced by I_ν and I_ν^{sat} is replaced by I^{sat}. Removing the superscript on the laser intensity means that the resulting saturation intensity, as determined by the numerical fits, is interpeted as the laser intensity at which the molecules at the center of the laser beam begin to saturate. This is the most useful way to think of the effect of the Gaussian beam on the saturation intensity. Dropping the subscripts is convenient since one is then dealing with the intensities as measured by a power meter, and is easier to visualize without the bandwidth factor. Dividing by the laser bandwidth only rescales the intensity axis and, therefore, rescales and changes the units of the measured value of the saturation intensity, but does not change the pressure dependence. The bandwidth factor that occurs in the resulting measured value of the saturation intensity will be discussed momentarily.

A grid search routine was used which contained two parameters, I^{sat} and α. The constant A in (3.2) was determined by a three parameter fit to the 800 torr data set, where the expression is most valid (data is most homogeneous) and then fixed at that value for the remainder of the fits. The results of the curve fits are given in Table 2, which lists the values of the parameters occurring in Equation (3.1) as determined by the least–squares fits to each of the four curves at different cell pressures. These three parameters are substituted into Equation (3.1) to generate

the theoretical curves, shown by solid lines in Figure 3. It is seen that the theoretical expression, Equation (3.1), fits the data quite well. The fit at 800 torr is very good, consistent with the fact that the total homogeneous width is about 40 Doppler widths at that pressure. It is also seen that the fits start to deviate from the data at the lower pressures, as expected since the total homogeneous width is only about 10 Doppler widths at 200 torr. At low laser intensities, both the data and the theoretical fits show a linear increase of the fluorescent signal with laser intensity. At the largest laser intensities the fits are good, due to the introduction of the lineshape parameter α. The important result of the introduction of this second parameter is that the large intensity data is fit very well and, as a result, the saturation intensity now decreases monotonically with decreasing pressure. It should be noted that the value of the lineshape parameter α, as determined by the numerical fits to the data, decreased from a value of 0.99 at 800 torr to 0.60 at 200 torr. This variation is entirely consistent with the expected range of values of this parameter, as originally introduced in Equation (2.42). The data sets at pressures below 200 torr were fit to the same expression. However, the fits were not nearly as good as the higher pressure fits shown in Figure 3, as expected, since the inhomogeneous

Table 2

Result of Numerical Fit of Equation (3.1) to Saturation Data

Pressure (torr)	A	α	I^{sat} (w/cm^2)
800	2.45	0.99	7.61×10^4
600	2.45	0.85	4.54×10^4
400	2.45	0.77	2.65×10^4
200	2.45	0.60	1.16×10^4

broadening contribution becomes more important at the lower pressures; in fact, at the lowest pressures, the value of α became less than 0.5. This is clearly the result of fitting a predominantly homogeneous expression to data that is starting to become intermediately broadened. This is of no consequence to this work since the objective is to evaluate the saturation approach at pressures of interest in gasdynamics and the 200 to 800 torr data is sufficient for this purpose. If one wanted to fit the lower pressure data, one would resort to the more exact approach outlined in Section 2.4.1.

The values of the saturation intensity determined by the numerical fits are shown in Figure 4 for the range of pressure of most interest in gasdynamic applications. It is seen that the saturation intensity increased in a nonlinear fashion from about 1×10^4 watts per square cm at 200 torr to about 7×10^4 watts per square cm at one atmosphere. The reason for the nonlinear behavior with pressure is that the saturation intensity expression, for the case of a 5 GHz bandwidth laser, contains two pressure dependent factors. Equation (2.41), along with (2.40), shows that the total homogeneous linewidth is pressure dependent (unless the laser bandwidth conpletely dominates the molecular collision width in (2.40)). The quenching rate is also pressure dependent (see Equation (2.27)). We have assumed that the factor f_2 is pressure independent. We can calculate the total homogeneous linewidth versus pressure, using (2.40) and (2.28), with a value for C_b of 12 MHz per torr at room temperature (determined in the next chapter), and divide the saturation intensity by $\Delta\nu_H$ to examine the resulting pressure dependence of the quantity I_ν^{sat}, given by Equation (2.36). The results of this calculation are shown in Figure 5. It is seen in this figure that I_ν^{sat} varies approximately linearly over this range. This result is entirely consistent with Equation (2.36) since $Q \gg A_{21}$ in this pressure range and Q is linear with pressure. This result also confirms the original assumption, and the conclusions of Reference 16, that the fraction f_2 is pressure independent.

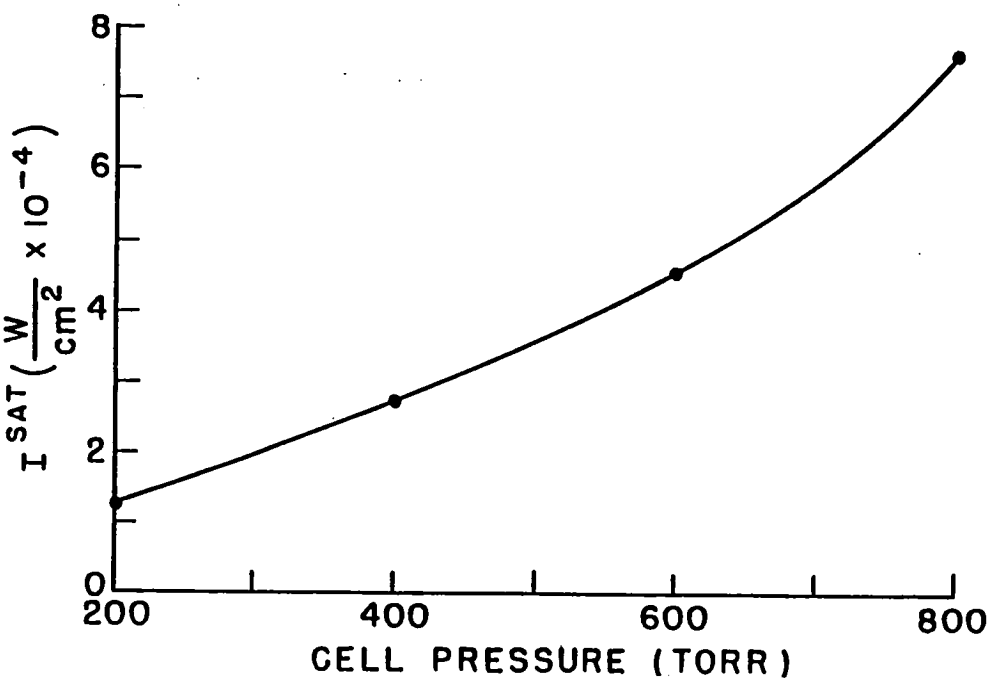

Fig. 4. Saturation Intensity (in watts per square cm $\times 10^{-4}$) versus Cell Pressure (in torr)

(The value of f_2 is not needed for the purposes of this work, but can be estimated using Equation (2.36) and the measured saturation intensity to be about 0.025). The pressure dependence of the saturation intensity, as given by (2.36) and (2.41), are, therefore, confirmed by the experimental data. The use of the predominately homogeneous formula (2.47), which includes the important Gaussian beam effect, is also validated.

3.5 Discussion

In the previous section is was shown that the experimental data for the saturation studies could be explained well by the theory of Section 2.4. It is, therefore, concluded that the model used in the theoretical development of Chapter 2 included all the physical processes of importance to the saturation studies of this work. It is

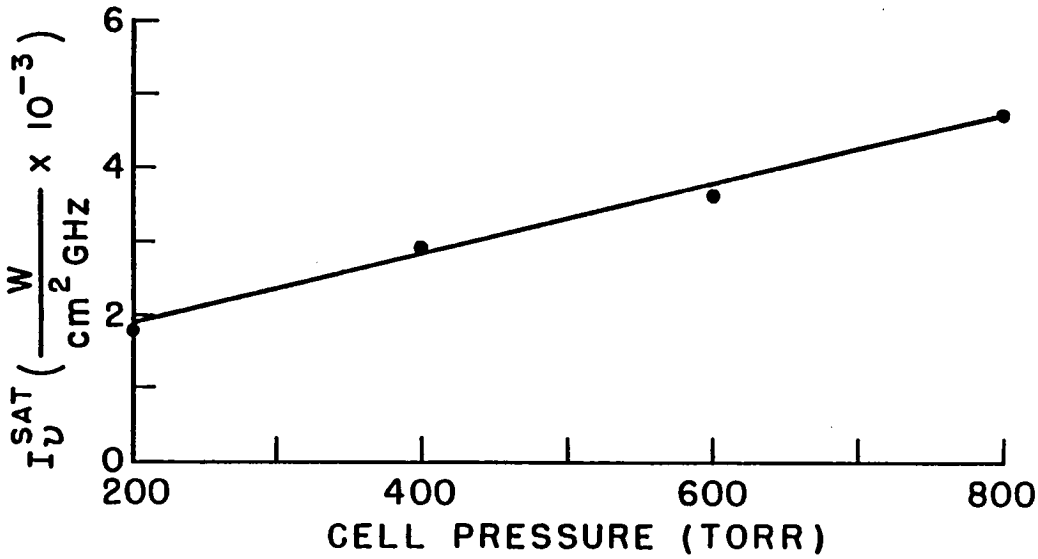

Fig. 5. Saturation Intensity per Bandwidth (in watts per square cm per GHz $\times 10^{-3}$) versus Cell Pressure (in torr)

also confirmed that the approximations made in establishing a rate equation model for the iodine molecule in Section 2.2 are consistent with the saturation data of this chapter. The values of the saturation intensity, as determined by numerical fits to the experimental data, are in agreement with the theoretical expressions of Chapter 2 for the static cell measurements.

The saturation intensities given in Figure 4 must be interpreted in relation to the important effect of the Gaussian transverse laser intensity distribution. The saturation intensity must be viewed as the laser intensity (as measured by a power meter for the entire beam) at which the molecules at the center of the beam, where the intensity is the greatest, begin to saturate. Therefore, due to the non–uniform laser intensity distribution, the molecules in the far wings of the laser intensity distribution experience an intensity that is always less than the intensity required to saturate them. This is the reason for the logarithmic dependence of the fluorescent signal with laser intensity. Saturation is never complete when one is employing a

Gaussian laser beam!

It is clear from the saturation data of Figure 3 that, for the degree of saturation achieved in this work, only a small percentage of the total number of molecules that contribute to the fluorescent signal are saturated, even though laser intensities of about 100 times the measured saturation intensities are achieved. If one observes the decay of the signal with increasing pressure, at a fixed laser intensity in Figure 3, it is clear that the quenching effect (Stern–Volmer factor), which causes this decay, is essentially the same at intensities below I^{sat} as at intensities 100 times above I^{sat}. Therefore, for the degree of saturation achieved in these measurements, as limited primarily by the Gaussian beam effect, the quenching dependence is essentially uneffected by the saturation approach. Greater laser intensities would move the fluorescent signal further along the logarithmic function and, therefore, somewhat reduce the effect of the quenching on the signal strength as a larger percentage of the fluorescing molecules become saturated. However, the quenching dependence would never be eliminated, even by much larger laser intensities, due to the Gaussian intensity distribution. Therefore, it is concluded that the saturation approach, although very attractive in theory, is not a viable scheme for eliminating the quenching complication when using laser–induced fluorescence in order to determine number density. The next chapter is devoted to a second approach, which was discussed theoretically in Chapter 2, for using laser–induced fluorescence for measuring number density in a compressible flow.

Chapter 4

Iodine Fluorescence Induced by a Singlemode Argon Laser: Experiment and Results

4.1 Introduction

In this chapter we discuss an experimental study of detuning for cancelling the quenching dependence of the laser–induced fluorescence signal in the measurement of number density. The theory for this approach was discussed in Section 2.3.3, where it was shown that, for asymptotically–large values of frequency detuning of a narrow bandwidth laser from the line center of a transition, the signal becomes independent of pressure and temperature, except for the temperature dependence of the line strength. The question to be answered by the experimental results reviewed in this chapter is, how well does this approach work in the laboratory? In order to provide a measure of the practical value in using this approach, the iodine molecule is again chosen as the test molecular system and the argon laser is employed as the radiation source. In this chapter, however, we consider a reduced linewidth of the laser output by the insertion of an etalon inside the laser cavity. By angle–tuning the etalon, the narrow bandwidth radiation can be tuned across the 10 GHz argon gain profile at 5145 Å. The resulting fluorescent signal can then be studied as a function of frequency detuning from the three iodine transitions located within this

tuning range (see Appendix A) and compared with the narrow bandwidth theory of Chapter 2. We are primarily interested in studying the pressure and temperature dependence and the magnitude of the fluorescent signal for the frequency detunings that are possible with the available argon laser and the accessible iodine transitions.

In Section 4.2, an experiment that was performed in a static cell is described. The resulting data are analysed using the theory of Chapter 2 and values for pertinent molecular iodine constants are derived by numerical fits to the data. A gasdynamic experiment is described in Section 4.3. Using the theoretical expressions of Chapter 2 and the molecular constants derived from the static cell measurements, the computed variation of the fluorescent signal with position in the gasdynamic flow is compared with the experimental values. This section concludes with a discussion of the application of the detuning approach based on our studies employing the iodine molecule and the argon laser.

4.2 Static Cell Experiment

4.2.1 Experimental Apparatus

A diagram of the experimental setup is given in Figure 6. The laser source was the same Coherent Radiation Model CR–18 argon laser used for the saturation measurements of the last chapter. Since a narrow bandwidth was required in this study for frequency detuning the laser near a single iodine transition, the bandwidth of the output was reduced to about 20 MHz by the use of an etalon in the laser cavity. The etalon is, essentially, a narrow bandpass filter, whose passband may be shifted in frequency by tilting its angle in the laser cavity. The argon output was, therefore, reduced in bandwidth until only a single axial cavity mode oscillated and was frequency tunable across the many cavity modes that lie under the 10 GHz

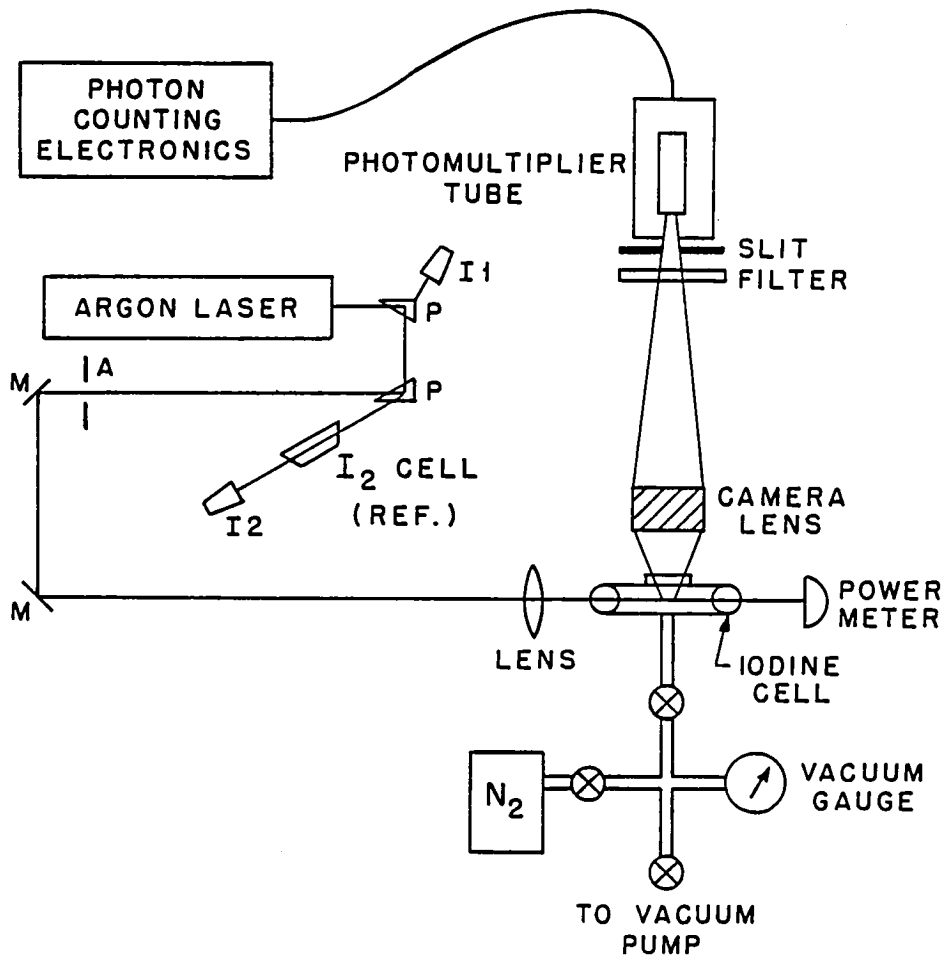

Fig. 6. Experimental Setup for Detuning Studies

argon gain profile at 5145 Å. The output power of the laser was reduced by the insertion of the etalon due to the etalon reflection losses, but with new laser mirrors, 2.6 watts of tunable singlemode output was obtained. The internal aperature was set for single transverse mode, TEM_{oo}, output. Two confocal interferometers, shown as I1 and I2 in Figure 6, were employed to monitor the bandwidth of the laser for single-mode output and to display the frequency detuning as the etalon angle was adjusted. Interferometer I1 had a 10 GHz free spectral range (separation between adjacent orders) and was used as a monitor of tuning across the entire 10 GHz argon

tuning range. Interferometer I2 was a 2 GHz free spectral range device which was useful for fine monitoring of the laser bandwidth and frequency. An evacuated cell containing 0.3 torr of iodine was used as an absolute frequency reference for the detunings of the etalon from a particular iodine transition. The interferometers and the reference cell were aligned on reflections from the prisms which were used to turn the laser beam.

When detuning away from the line center of a molecular transition, the resulting signal level decreases. In addition, due the the Stern–Volmer quenching factor, the fluorescent signal is considerably lower at pressures near one atmosphere than at one torr. The resulting signal level, when detuning at large pressures, can be quite low. Therefore, the detection scheme employed in the detuning experiments was more sophisticated than in the saturation experiments of the last chapter. When collecting small signals, any stray light must be suppressed. In addition, the plasma tube fluorescence from the laser cavity, which is collinear with the laser beam, must be separated and blocked. A portion of the plasma fluorescence is in the red part of the spectrum and this is precisely where the iodine fluorescence is to be collected. An efficient way to separate the undesirable plasma fluorescence from the 5145 Å radiation is to use dispersive optical elements in the beam path. The arrangement shown in Figure 6 used two prisms to provide the necessary dispersion and, therefore, spatial separation of the frequency components of the laser output. By placing an aperture two meters beyond the second prism, the plasma light at about 600 nm was separated by 5.5 cm from the 5145 Å radiation and the plasma light at about 480 nm was separated to the other side of the beam center by 5 cm. The aperture was aligned to pass the desired 5145 Å light and block the two primary components of argon plasma light in the red and violet parts of the spectrum. This component of the background noise, which is normally collinear with the laser beam and difficult to remove from the collected signal, was effectively removed by the prisms and the

blocking aperature. The laser beam was directed by two high–reflector mirrors to the opposite end of the table where the fluorescent experiment was set up.

The laser beam was focused by a 12.2 cm focal length, anti–reflection coated lens to a spot size of about 13.5 μm. The beam passed through the iodine cell and was dumped into a power meter for monitoring of the laser output power. A pyrex iodine cell was constructed for this experiment that allowed iodine crystals to be placed in a temperature–controlled reservoir located at the bottom of the cell. With this cell, room temperature drifts and laser heating effects did not change the iodine partial pressure in the cell and the experimental procedure did not have to account for this effect. The cell contained high quality optical windows, both for access by the laser beam and for collection of the fluorescent signal. The laser access windows were set at Brewster's angle to minimize scattered laser light and maximize the laser power reaching the iodine molecules inside the cell. The cell was isolated by a vacuum valve from a gas–handling system that allowed evacuation of the cell, filling of the cell with variable nitrogen pressures, and monitoring of the cell pressure by a vacuum gauge.

The cell was placed at the focus of the laser beam and collection optics were aligned, through the optical viewing window, onto the beam focus. The fluorescent signal was collected by a 4 cm diameter Nikon camera lens, placed 7 cm from the beam focus. The lens produced a magnified image, with measured magnification of 3.7, of the beam focus on a vertical slit placed 39.5 cm from the camera lens. The slit was set to a width of 555 μm so that a 150 μm length of the laser beam at the focus was observed. This resolution was chosen for the gasdynamic experiment of Section 4.3 and used here so that no realignment of the optics would be necessary in the transition from the static to the gasdynamic experiment. A 540 nm long pass filter was placed between the collection lens and the slit to block scattered laser light and pass the iodine fluorescent signal. The fluorescent signal passed

through the slit onto the photocathode of a photomultiplier, which was used as the detection device. The photomultiplier tube was placed in a housing which was cooled both thermoelectrically and by flowing methanol to reduce the dark count of the tube. Dry nitrogen was maintained at the front window of the tube to prevent condensation of water vapor on the cooled window. The output of the photomultiplier tube was sent to photon counting electronics, which contained a discriminator and an amplifier to enable counting of individual photons incident on the photocathode. In using this *extremely* sensitive detector, stray light from any sources in the laboratory had to be minimized. Light–tight boxes were constructed around the entire collection system, enclosing the lens and detector. Light blocks were set up at various locations on the optical table to block any stray laser reflections or light from instrumentation. With these precautions, the background signal was very small, as discussed in the next section.

4.2.2 Experimental Procedure and Results

The experimental procedure for the collection of the fluorescent data is now described. The procedure began several days prior to the recording of data, due to the need for the photomultiplier tube to cool and reduce the dark count of the detector sufficiently. The thermoelectric and methanol coolers were turned on to lower the tube temperature to about 0 degrees centigrade. Several days were then required for the dark count to stabilize. On the day of the experiment, the methanol cooler was further reduced to –20 degrees centigrade. Within a couple of hours, the dark count stabilized and the background was read as 50 counts per second, with the laser blocked completely. With the laser detuned outside the 5145 Å gain profile, so that only plasma light was emitted, the background signal increased to 55 counts per second. When the laser was tuned to oscillate at 5145 Å and the iodine cell removed, the signal level was 300 counts per second, due to scattering from the

room air. With the iodine cell in place, but completely evacuated (no iodine), the signal was recorded as 70 counts per second. The slight increase from the 55 counts per second was due to some scatter from the cell windows. Since the smallest signal level recorded was 1880 counts per second, it is seen that the background signal was a small percentage of the total fluorescent signal. Iodine crystals were added to the cell reservoir, the cell was evacuated, and the reservoir maintained at 15 degrees centigrade by the methanol cooler, producing a vapor pressure of about 0.2 torr. The crystals were allowed to come into equilibirum with the cell walls as described in Chapter 3 so that a steady-state iodine vapor resulted, in equilibrium with the crystal reservoir and cell walls.

The laser was aligned for optimum power, transverse mode quality, and single-mode operation. The optics were aligned as shown in Figure 6. The laser was tuned to coincide with the primary iodine transition as indicated by the iodine reference cell and the photon counting output. There are three transitions, as indicated in Appendix A, but, unless otherwise noted, we will refer to the P13–R15 pair as the *primary* iodine transition. The signal was checked for linearity by inserting an ND 0.3 filter in the collection path. The resulting factor of two signal decrease proved the detector was linear at the signal level corresponding to zero detuning and zero nitrogen pressure. Since this is the largest signal to be collected, the detector was linear over the entire range of measurements. With the laser tuned onto the iodine transition, signal levels were recorded as nitrogen pressure was added to the iodine cell. A complete set of pressure measurements were made from 1 to 760 torr nitrogen. The laser was then tuned away from the iodine transition by 1 GHz, as indicated by the interferometers, the power recorded, and the pressure measurements repeated. This procedure was repeated for detunings of 2, 3, and 4 GHz, by tuning the etalon and monitoring the frequency on the interferometers. The complete set of static cell detuning data is given in Table 3, normalized to a

laser power of 800 milliwatts, the power delivered to the molecules inside the cell with the laser tuned to the iodine transition. The detuning values are within 100 MHz of the nominal values listed in the table, due to inevitable laser frequency drifts during the course of collection of a data set. The data of Table 3 are used as the basis of the analysis of the following section.

4.2.3 Analysis

We now apply the narrow bandwidth laser theory of Section 2.3 to the static cell detuning data in order to investigate the effects of the detuning on the fluorescent signal. In this process, we use numerical least-square fits of the theory to the data in order to deduce molecular iodine constants at the room temperature reference condition in the static cell. These constants will be useful for the gasdynamic experiments to be discussed.

The theoretical expression for the fluorescent signal under narrow bandwidth laser excitation is given by Equation (2.24). The parameters in this equation that vary in the static cell experiments must first be identified. The saturation effects can be neglected in fitting this equation to the data, for the following reason. The calculated intensity at the beam focus is reduced to 2.8×10^5 watts per square cm, due to the lower laser output power with the placement of the etalon in the cavity and to the larger laser beam spot size used in this experiment. This intensity is slightly greater than the measured saturation intensity of Chapter 2, but, due to the Gaussian beam effect, this means that only a small percentage of the fluorescing molecules are saturated. Therefore, we will use $I \ll I^{sat}$ and replace B' by B in Equation (2.24). (It should be noted that the numerical fits were performed with saturation effects included and the results indicated that these effects were, in fact, entirely negligible.) With this simplification, the only two variables in the equation are the laser detuning, which occurs in the Voigt integral, and the cell pressure,

Table 3

Fluorescent Signal (in photons per second) at Measured Total Cell Pressures (in torr) and Laser Frequency Detunings (in GHz from iodine line center). (Data normalized to 800 mW laser power.)

Pressure (torr)	$\Delta\nu$=0 GHz	$\Delta\nu$=1 GHz	$\Delta\nu$=2 GHz	$\Delta\nu$=3 GHz	$\Delta\nu$=4 GHz
1	1.00×10^{6}	8.70×10^{3}	3.63×10^{3}	2.99×10^{3}	6.00×10^{2}
1.8	1.05×10^{6}	1.30×10^{4}	3.98×10^{3}	3.07×10^{3}	1.01×10^{3}
3	1.05×10^{6}	1.67×10^{4}	4.40×10^{3}	3.24×10^{3}	1.40×10^{3}
6	8.70×10^{5}	2.05×10^{4}	5.10×10^{3}	3.72×10^{3}	2.00×10^{3}
10	6.50×10^{5}	2.31×10^{4}	5.67×10^{3}	4.09×10^{3}	2.54×10^{3}
18	4.20×10^{5}	2.54×10^{4}	6.20×10^{3}	4.31×10^{3}	3.09×10^{3}
30	2.42×10^{5}	2.65×10^{4}	6.75×10^{3}	4.53×10^{3}	3.54×10^{3}
60	1.14×10^{5}	2.50×10^{4}	7.20×10^{3}	4.67×10^{3}	3.83×10^{3}
100	5.80×10^{4}	2.03×10^{4}	7.50×10^{3}	4.60×10^{3}	3.79×10^{3}
180	2.35×10^{4}	1.42×10^{4}	7.70×10^{3}	4.38×10^{3}	3.53×10^{3}
300	1.05×10^{4}	8.89×10^{3}	6.05×10^{3}	3.77×10^{3}	2.98×10^{3}
600	3.90×10^{3}	4.28×10^{3}	3.60×10^{3}	2.85×10^{3}	2.06×10^{3}
760	2.80×10^{3}	2.78×10^{3}	2.55×10^{3}	2.12×10^{3}	1.88×10^{3}

which occurs in the broadening parameter, B, of the Voigt integral and in the quenching rate, Q. There is a third parameter that also appears which will be discussed momentarily. Since the experiment is performed at constant temperature and constant iodine number density, the equation can be written as

$$S_F = (Constant)\frac{1}{1+Q/A_{21}}V(D,B), \tag{4.1}$$

where *Constant* is a fixed number for all the static cell data. The quenching rate, Q, and the broadening parameter, B, are both linear in pressure, as given by Equations (2.27), (2.19) and (2.28), respectively. Here, the Stern–Volmer factor is rewritten in nondimensional form with the quenching rate normalized by the stimulated emission rate and defined as

$$\frac{Q}{A_{21}} = C_{qa}\frac{p(\text{torr})}{(1\,\text{torr})}\sqrt{\frac{298\,\text{K}}{T(\text{K})}},$$

where C_{qa} is a dimensionless number and the ratio is referenced to a pressure of one torr and a temperature of 298 K. Using this definition and the definitions given in Chapter 2 for D and B, numerical least–square fitting routines can be used to determine the constants in these definitions, C_{qa} and C_b, at the reference temperature of 298 K. Such a numerical fitting routine must be able to efficiently evaluate the function given by the above equation and this is nontrivial due to the complexity of the Voigt integral. The method employed in this work for the evaluation of the Voigt integral is outlined in Reference 32 and involves conversion of the integration to a summation of terms of a series expansion. It is shown in that reference that 31 terms yields an accuracy of at least eight significant figures. A short Fortran subroutine was used in a grid search routine to numerically fit the above expression to the data.

The numerical fits proceeded as follows. The zero detuning data set was fit to the above expression with the D parameter set to zero. The resulting fit produced

a value for the *Constant* in Equation (4.1) and approximate values of the quenching constant, C_{qa}, and the broadening constant, C_b. In performing the fit to this data set, a room temperature Doppler width of 440 MHz was used in the definition of the B parameter. Next, the 1 GHz data set was fitted with a value of D corresponding to a $\Delta\nu$ of 1 GHz and the room temperature Doppler width. It was noted that this value of D was too large, since the 1 GHz theoretical fit detuned much more quickly than the data at that value of laser detuning. The reason for the discrepancy is as follows. The detuning D is normalized by the Doppler width (see Equation (2.18)). The Doppler width is the inhomogeneous width of the transition, due to the spreading of the resonant frequency of the transition by the velocity of the molecules. There is another effect that must be considered in the case of the iodine molecule. In Appendix A it is noted that the primary iodine transition has a hyperfine width of about one GHz. The P13 and R15 rotational transitions are actually split into 21 hyperfine components each, due to the coupling of the rotational and nuclear angular momenta. These hyperfine components vary in frequency by a total of about 1.2 GHz for this iodine transition. This hyperfine splitting has the same effect as the Doppler broadening, that is, to smear the center frequency of the transition. However, the hyperfine width is not temperature dependent, so that, even at the lowest possible tempertures, the width of this iodine transition is limited by the hyperfine width. Therefore, a constant value of the hyperfine width must be added to the Doppler width wherever the Doppler width occurs in the expression for the fluorescent signal. The value of the hyperfine width, denoted as $\Delta\nu_{hyp}$, to be added to the Doppler width is determined as follows. Numerical fits are performed on the two data sets corresponding to 0 and 1 GHz detuning. The resulting hyperfine width, $\Delta\nu_{hyp}$, is the value that produces a decrease in signal level, when the laser is detuned by 1 GHz, that corresponds to the observed decrease in signal level. The results of the curve fits to the zero and one GHz detuning data sets are the

four parameters given in Table 4. The constant should have a value of about the magnitude of the fluorescent signal at zero detuning and a pressure of one torr, since the Stern–Volmer factor and the Voigt integral both have values very close to unity for these conditions. The broadening parameter was determined to be 12 MHz at one torr and room temperature, a value consistent with typical broadening parameters of a few MHz per torr. The quenching parameter is consistent with the measured Stern–Volmer quenching constant given in Appendix A. The hyperfine width to be used must be the effective hyperfine width at half maximum and the value of 333.5 MHz is reasonable. Therefore, it is concluded that the values of the parameters determined by the fits to the zero and one GHz detuning data curves are consistent with their expected values.

Using the values of the parameters given in Table 4 and Equation (4.1) (with $\Delta\nu_{hyp}$ added to $\Delta\nu_D$), theoretical curves were generated that predict the fluorescent signal versus cell pressure for the detuning values used in the experiment. Figure 7 is a plot of the theoretical curves for detuning values of 0, 1, 2, and 3 GHz from the primary iodine transition. Also included in this figure are the experimental data for the same values of detuning. It is seen that the parameters determined in the fits to the 0 and 1 GHz detuning curves fit the data quite well. However, the calculated fluorescent signal curves for the 2 and 3 GHz detuning values fall well below the corresponding data. The reason for this behavior is that the theory, to this point, only included contribution to the fluorescent signal from the primary

Table 4

Parameters Determined From Static Cell Detuning Data

Constant	C_b(MHz)	C_{qa}	$\Delta\nu_{hyp}$(MHz)
1.02×10^6	12.0	0.055	333.5

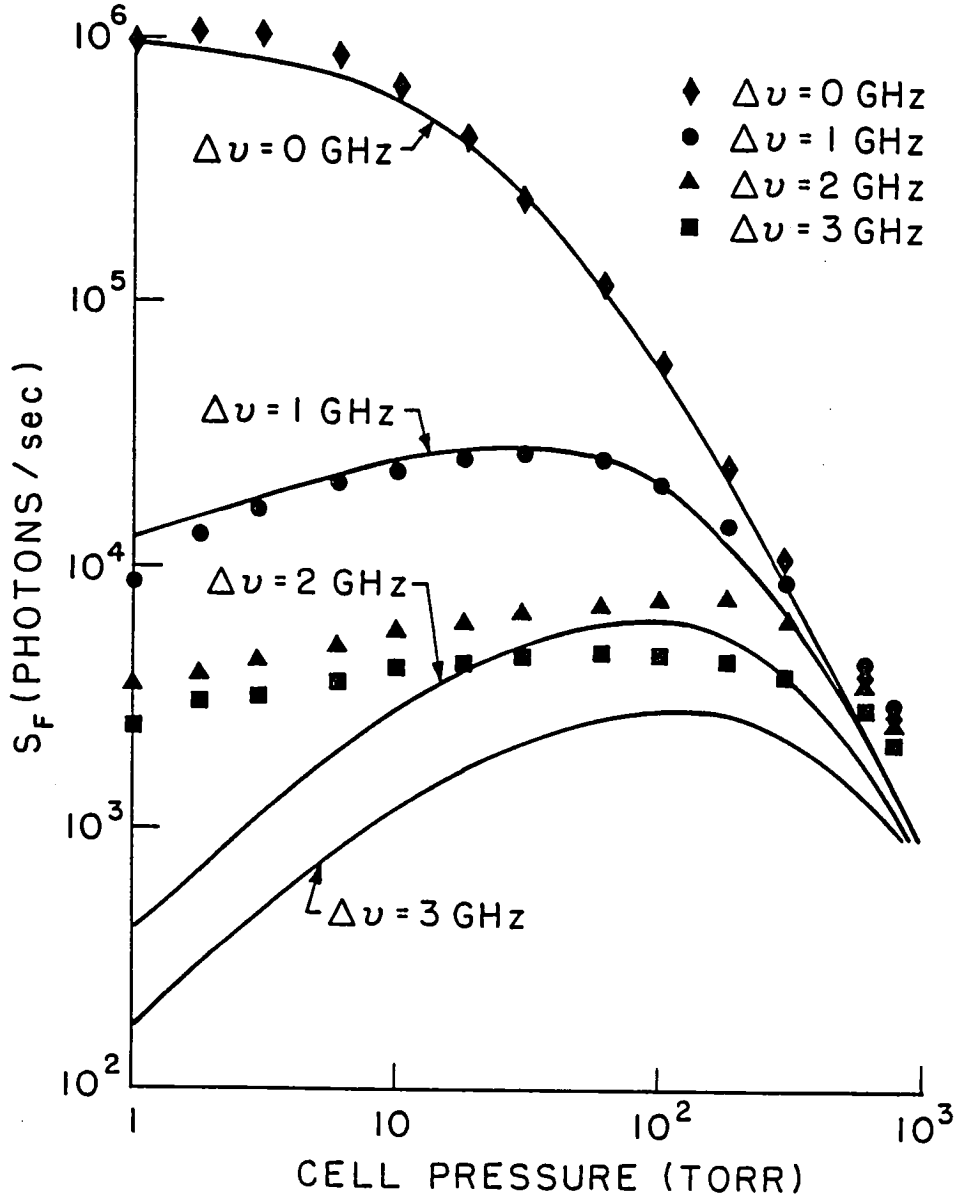

Fig. 7. Static Cell Detuning Curves: Fluorescent Signal (in photons per second) versus Cell Pressure (in torr)

iodine transition. There is a hot–band transition located 2.47 GHz from the primary transition, as noted in Appendix A. At room temperature the strength of this hot–band transition is 0.9 % of the primary transition strength [33] and, therefore,

its contribution cannot be ignored when the fluorescent signal due to the primary transition has decreased by more than two orders of magnitude for 2 and 3 GHz detunings. The model is extended to include the hot-band transition, located 2.47 GHz from the primary transition with a 0.009 weighing factor and the same broadening and quenching parameters as determined for the primary transition. The third transition mentioned in Appendix A and located 6.42 GHz from the primary transition is also included, with a relative strength at room temperature of 1.04 [34] and the same broadening and quenching parameters as the primary transition. The resulting theoretical curves are shown in Figure 8, along with the corresponding experimental data. It is clear from this figure that, with the addition of the other two iodine transitions, the theoretical curves fit the data quite well for detunings of 0 to 3 GHz from the primary transition. Fits were also done to the 4 GHz detuning data and it was found that this data could also be explained well by the theory, but is not discussed further, since the optimum results will be obtained in the gasdynamic experiment for the 3 GHz detuning value. Larger detunings from the primary transition effectively decrease the detuning, due to the third iodine transition located 6.42 GHz from it. It is precisely this problem of closely-spaced iodine transitions at 5145 Å that will be seen to be a limiting factor in the gasdynamic measurements.

4.2.4 Discussion

The preceeding analysis has shown that the narrow bandwidth fluorescence theory of Chapter 2, as expressed in Equation (4.1) for the static cell conditions, provides a good description of the behavior of the fluorescence signal at varying pressure and laser detunings. The parameters that were obtained from the numerical fits, and listed in Table 4, will form the basis for the analysis of the gasdynamic experiment of the next section. In this sense, it is viewed as a calibration experiment.

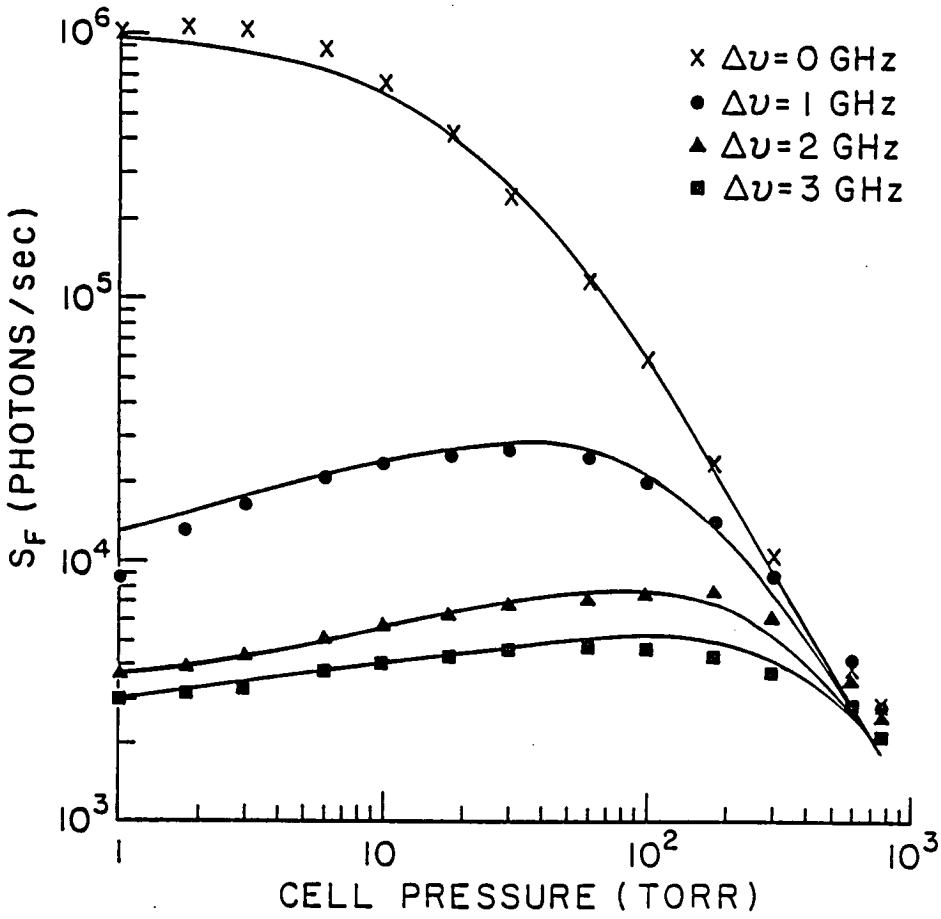

Fig. 8. Static Cell Detuning Curves Including Three Iodine Transitions: Fluorescent Signal (in photons per second) vs Cell Pressure (in torr)

In addition, the static cell experiment demonstrated the decrease in fluorescent signal to be expected for detuning values of a few GHz. The resulting signal level at 3 GHz detuning is well above the background limit in the present experiment and is only a factor of two lower than the zero detuning signal level at a pressure of about one–half an atmosphere.

The resulting data curves at 2 and 3 GHz are somewhat misleading, however, since they seem to indicate that the fluorescent signal is roughly independent of

pressure, from one torr up to pressures of about 200 torr. This is precisely the desired result: to use large enough detuning values that the fluorescence expression simplifies, as discussed in Chapter 2, and the signal becomes pressure independent. The computed value of the detuning parameter D is 6.5 for 3 GHz in the static cell. This number is somewhat greater than unity and large enough to make the asymptotic solution given in Section 2.3.3 nearly valid. However, the asymptotic solution exhibits an increase in signal level with pressure at low pressures. This behavior is not exhibited by the 2 and 3 GHz detuning data. The real reason for the flat response of these two data curves with pressure is the presence of the hot-band transition at 2.47 GHz. Extrapolating these results to a gasdynamic experiment can be somewhat misleading since one might be led to expect such pressure independence in the dynamic situation. As will be seen in the next section, this is not a valid extrapolation since the static cell experiment is performed at room temperature and constant iodine number density. The effects of these two additional variables must be accounted for when extrapolating the static cell results to a gasdynamic situation. The primary results of the static cell calibration experiment are the determination of the molecular broadening, quenching and hyperfine-width constants at a reference temperature and the indication of the signal levels to be expected for typical values of detuning from the primary iodine transition.

4.3 Gasdynamic Experiment

The static cell experiment of the preceeding section was conducted under the conditions of constant temperature and constant iodine number density. The pressure was varied over a range of 1 to 760 torr and the detuning values ranged from 0 to 4 GHz. A typical gasdynamic experiment would be conducted within this pressure range, but the temperature would also vary greatly as the Mach number varied in the flowfield. For the purposes of this initial investigation, we will

concentrate on flows which are steady and isentropic, so that all the thermodynamic variables in the flowfield may be calculated once the Mach number distribution is known. In this section, we investigate the fluorescent signal distribution in a compressible (gasdynamic) flowfield which contains a large variation of both pressure and temperature. The iodine gas will be added to the flowfield in a reservoir, so that the mole fraction mixed in the reservoir is maintained throughout the flowfield. Therefore, the iodine number density will vary, unlike the static cell experiment. The analysis of the previous section must be extended to account for the variable temperature and iodine density to describe the fluorescent signal distribution in such a compressible flow. All the essential ingredients needed in the analysis are contained in the theoretical expressions of Section 2.3 of Chapter 2. The formulas of that section already contain the proper temperature dependence for the parameters occurring in Equation (2.24), which describes the fluorescent signal as a function of pressure, temperature, and iodine number density. The static cell experiment provided a measure of the quenching, broadening and hyperfine-width constants, which occur in those definitions, at a reference temperature of 298 K. Extending the analysis to a compressible flowfield is a straightforward procedure and will be further discussed in a later section.

The choice of what compressible flowfield to employ in this investigation must be considered. In evaluating a new diagnostic technique like laser-induced fluorescence for the measurement of density, one would like to employ a compressible flowfield that provides a good test of the theoretical model of the technique, containing a large variation of pressure, temperature and density. The flowfield must also be well predicted from compressible flow theory, so that a comparison can be made between the results of the diagnostic technique and the variables in a known flowfield. Since this experimental work was performed in an optical laboratory, and not a fluid mechanics laboratory, an additional constraint was that the flow be

of relatively simple construction. Since we wish to study compressible flows, the flow rates are necessarily large, and, therefore, the flow device must be quite small since the only available reservoir was a standard compressed gas bottle. The compressible flowfield chosen that satisfied these critera was the underexpanded flow from an axisymmetric sonic nozzle. In such a flowfield if the pressure outside the nozzle is sufficiently low compared to the reservoir pressure (less than half as large for a nitrogen flow), the flow accelerates to a Mach number of one at the exit of the nozzle, and then continues to accelerate supersonically outside the nozzle. As the Mach number increases in the flowfield, the pressure, temperature and density all decrease with distance downstream from the nozzle exit. Such a flowfield is simple to construct, provides a large range of thermodynamic variables if the Mach number range is large, is easily probed by a laser beam, can be well predicted by compressible flow theory and can be run from a standard compressed gas bottle, providing that the nozzle exit diameter is kept small.

Photographs of the experimental setup are shown in Figure 9. The positioning of the laser and optical components was the same as that for the static cell experiment, as shown in Figure 6, except that the underexpanded jet apparatus replaced the static cell at the focus of the laser beam.

A schematic of the underexpanded jet flow facility is shown in Figure 10. The nozzle was machined from stainless steel, which is less reactive to iodine than other metals, and contained a smooth conical internal contour with an exit diameter of 1.5 mm. This is an *extremely* small nozzle to study with conventional probes, but with a laser beam focused to a few μm it can be probed with good resolution and without concern for the size of a physical probe. The small exit diameter enabled the flow to be run for a duration of about 8 hours from a single bottle of compressed nitrogen. The high pressure nitrogen was reduced by a pressure regulator to 22 psia, the reservoir pressure for the nozzle flow to be studied. The nitrogen

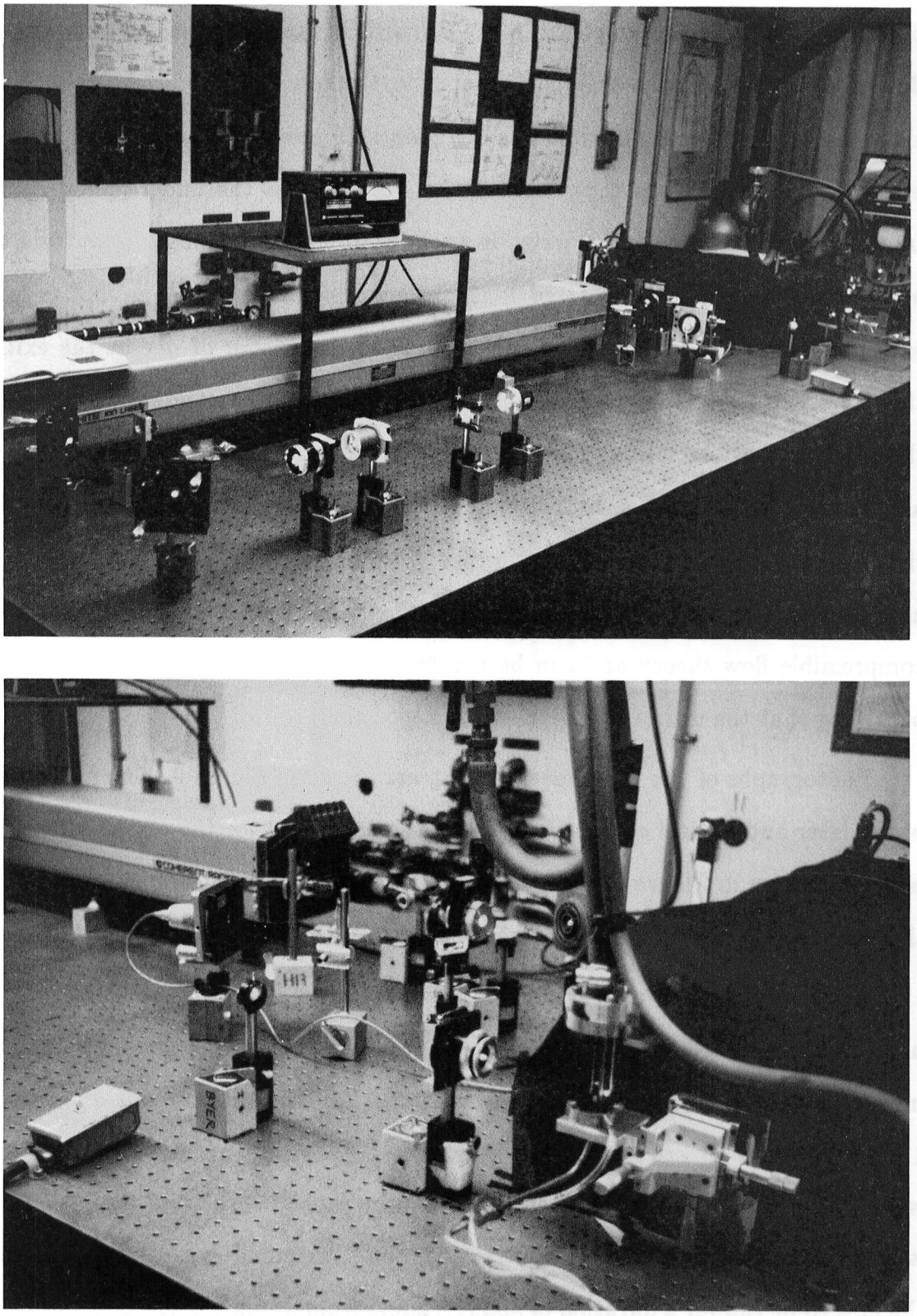

Fig. 9. Photographs of the Optical Setup for the Gasdynamic Experiment

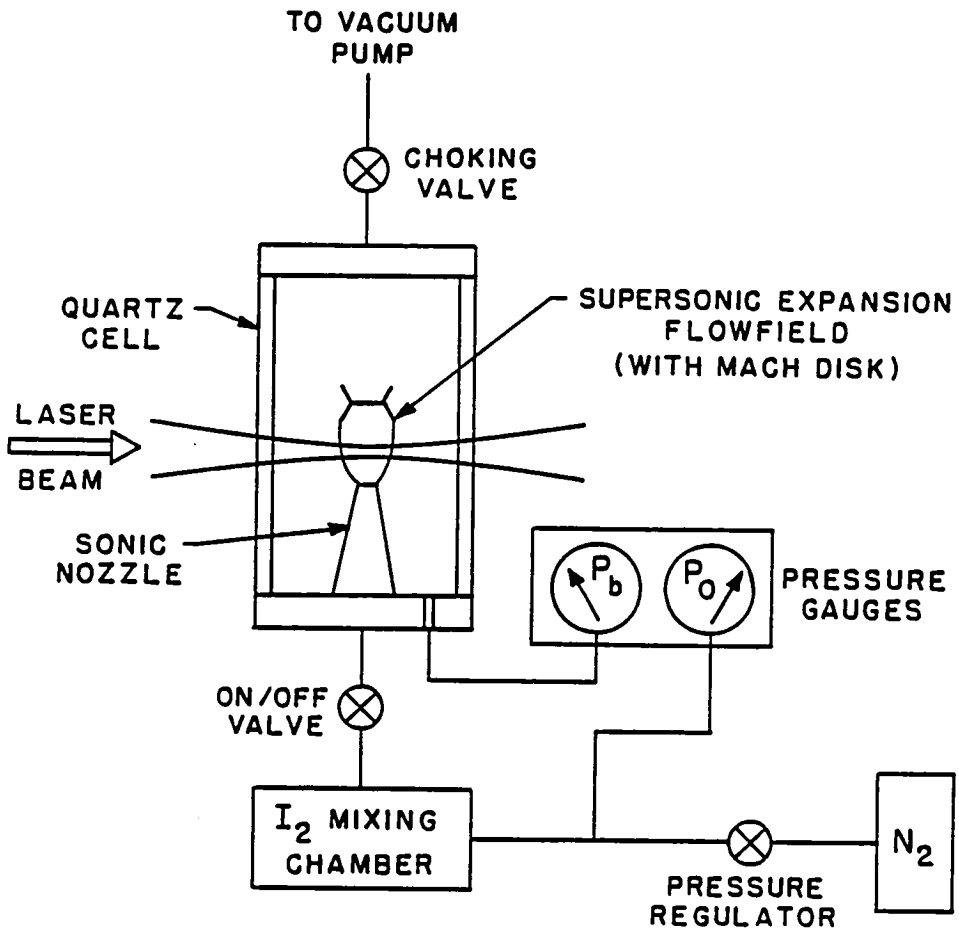

Fig. 10. Iodine–Seeded Underexpanded Nitrogen Jet Flow Facility

flowed into a chamber containing iodine crystals, for the seeding of iodine into the nitrogen flowfield. The iodine mixing chamber was maintained at approximately room temperature, so that the seeding mole fraction was about 0.3 torr of iodine in 1137 torr of nitrogen, a seeding fraction of 2.6×10^{-4} parts iodine to one part nitrogen. This seeding technique worked very well in the experiment and the fluorescent signal at any point in the flowfield was constant both for long and short periods of time, indicating that the seeding fraction was constant in time. An on–off valve was located between the iodine mixing chamber and the nozzle to enable

quick shutoff of the flow in order that the nitrogen bottle gas could be conserved. The nozzle exhausted into a vacuum–tight, rectangular, fused quartz cell, with a 2 cm square cross section and a length of 7 cm. The cell windows were optically polished to minimize scatter of laser radiation. A 6.4 mm hole in the end of the cell opposite the nozzle provided an exit for the flow from the cell. Downstream of the cell was located a valve, whose internal area could be well controlled. This valve was used as a choking valve, to maintain a desired pressure inside the quartz cell by decreasing the area of the valve until the flow became sonic inside the valve. Once the valve area was small enough to cause it to become sonic, or choke, the mass flow rate through the system and, therefore, the pressure inside the quartz cell could be controlled by varying this area. The maximum mass flow rate for the flow system is fixed by the sonic nozzle. A vacuum line ran from the choking valve to a vacuum pump, located on the roof of the laboratory for safe exhausting of the iodine–seeded gas. Pressure gauges were used to monitor the input reservoir pressure to the nozzle and the back pressure inside the quartz cell. The nozzle and quartz cell chamber were located on translation stages that allowed three degree of freedom movement of the flow chamber with respect to the optical table. In this manner, the laser beam and optics were always fixed and the jet flowfield was moved in order to probe different spatial locations in the flowfield.

Before proceeding to discuss the experiment further, some background is needed concerning the fluid mechanics of the underexpanded jet. The flow inside the nozzle can be described by one-dimensional, steady, isentropic equations. Reference 35 contains a complete discussion of the operation of a Laval nozzle. For the nozzle used in this work, the minimum area was at the exit plane. For sufficiently low back pressure (the pressure in the quartz cell in this work), the flow reaches a Mach number of one at the nozzle exit and continues to accelerate beyond the nozzle in order to further reduce the pressure to match the back pressure. To describe

the fluid mechanics of the flowfield beyond the exit plane, one must relax the one-dimensional assumption and assume, additionally, that the flow is irrotational. An equation results for the velocity potential that is a second order, nonlinear, partial differential equation. For the case of supersonic flows (Mach number greater than unity) this equation is hyperbolic and is solved by the method of characteristics. Given the reservoir pressure and the back pressure, one then generates the solution for the flowfield as the Mach number increases beyond the exit plane of the nozzle. One finds that the flow overexpands to pressures less than the back pressure and then undergoes a sudden recompression, in the form of a shock wave, to increase the pressure in the flow. The details of such a solution for the case of rectangular geometry is given in Reference 36.

Using the results of the method of characteristics solution, Ashkenas and Sherman [37] have given an extremely accurate fitting formula for the Mach number variation along the centerline of the underexpanded jet flowfield. For the purposes of this work, all measurements will be made along the jet centerline, from the nozzle exit plane to beyond the shock wave. Therefore, the Ashkenas and Sherman formula is employed to calculate the Mach number variation along the jet centerline and the isentropic relations then produce the distribution of pressure, temperature and density along the centerline, once the Mach number distribution is calculated. The Ashkenas and Sherman formula gives good results as close as one nozzle diameter to the jet, for the case of nitrogen with a specific heat ratio of 1.40. From one nozzle diameter to the exit plane, the Ashkenas and Sherman calculations are extrapolated to the sonic conditions at the exit plane. The results of these calculations are given in Table 5, which lists the Mach number, pressure, temperature and density, normalized to the sonic value at the nozzle exit, versus position along the jet centerline. The calculations are based on a reservoir pressure of 22 psia and a cell, or back, pressure of 53 torr, values used in the experiment. The Mach number

Table 5

Variation of Gasdynamic Parameters with Position along Centerline of Underexpanded Jet Flowfield (reservior pressure = 22 psia, cell pressure = 53 torr, nozzle exit diameter = 1.5mm)

X(mm)	Mach No.	p(torr)	T(K)	$N_{I_2}/N^*_{I_2}$
0.000	1.00	600	248	1.000
0.254	1.32	400	222	0.700
0.508	1.54	294	201	0.495
0.762	1.74	218	184	0.370
1.016	1.95	158	165	0.282
1.270	2.17	113	150	0.216
1.524	2.39	82	133	0.172
1.778	2.67	51	119	0.138
2.032	2.96	33	108	0.112
2.286	3.23	22	97	0.090
2.540	3.45	16	88	0.075
2.794	3.68	12	81	0.060
3.048	3.87	8.9	74	0.049
3.302	4.07	6.9	69	0.041
3.556	4.25	5.4	65	0.035
3.683	4.34	4.8	63	0.032
4.064	0.427	105	290	0.152

increases and the thermodynamic variables decrease isentropically until about 3.7 mm from the nozzle exit. At this point the shock wave is encountered and the Mach number suddenly becomes less than one and the other variables increase as the flow is recompressed. The calculated location of the normal shock wave using the formula of Reference 37 is 4.57 mm from the exit. This formula is based on a free jet, without an enclosure. The shock occurs closer to the exit in this case due to the proximity of the walls of the quartz cell. This table gives the distribution of thermodynamic variables in the jet flowfield for subsequent calculation of the fluorescent signal distribution and comparison with the actual density distribution. It is seen that a large range of variation exists in the pressure, temperature and density in this flowfield, making it a good test flow for this diagnostic technique.

4.3.1 Experimental Procedure and Results

As mentioned in the previous section, the jet flowfield was located at the focus of the laser beam, replacing the static cell of the previous experiment. The remainder of the optical setup and the instrumentation was the same as in the static cell experiment. When the flow was turned on and the laser tuned onto the primary iodine transition as indicated by the reference iodine cell, a bright fluorescing line was easily observed as the laser beam penetrated the iodine-seeded flow. It was, therefore, easy to visually align the jet with respect to the laser beam and the collection optics, by using the three translation stages on which the jet was mounted, so that measurements could be obtained along the jet centerline. Figure 11 contains two photographs of the fluorescence induced by the focused laser beam in the quartz cell and jet flowfield. The top photograph in the figure was taken at the zero reference point which was located a few μm above the level at which the laser beam began to intersect and scatter from the nozzle exit. This photograph illustrates the high spatial resolution possible with the focused laser beam, even

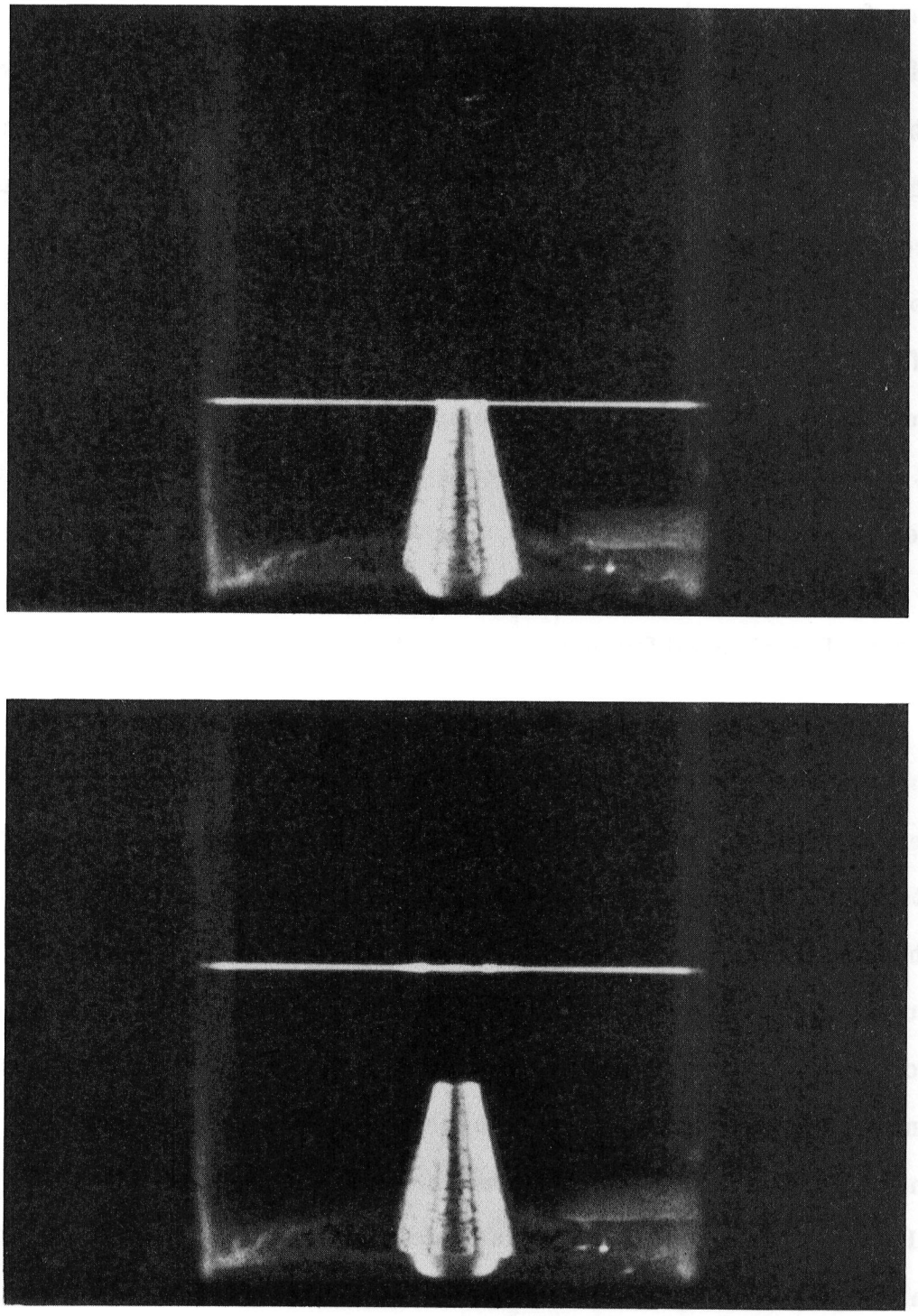

Fig. 11. Photographs of the Fluorescence Induced by a Focused Laser Beam in the Iodine–Seeded Jet Flow Facility

in such a small flowfield. The bottom photograph in Figure 11 was taken with the laser beam located 3.5 mm above the zero reference point and just before the location of the normal shock wave. The modulation of the fluorescence in the jet flowfield by the shock structure of the Mach disc is visible in this photograph. These photographs illustrate that optical alignment could be accomplished visually to good accuracy, even considering that the total length of the isentropic part of the flow from the exit to the Mach disk was less than 4 mm. The slit in the collection optics remained open to 555 μm so that a 150 μm length of the fluorescing laser beam was observed. This length was 10 % of the nozzle diameter and was considered to be a reasonable resolution in the transverse dimension of the flowfield. The data points were collected at 254 μm increments from the nozzle exit. This increment is about 10 laser beam diameters for the focused spot size of 13.5 μm.

The procedure used to collect the data in the jet flowfield was as follows. The alignment of the jet with respect to the optics was completed as above. The etalon was tuned onto the primary iodine transition, as indicated by the iodine reference cell and noted on the interferometers. The fluorescent signal was then recorded as a function of position at 254 μm intervals, by lowering the jet with respect to the laser beam. The detector was checked for linearity and the laser power noted. The etalon was then detuned from the iodine transition by 1 GHz, as indicated by the interferometers, and the procedure repeated. Measurements were also recorded for detunings of 2 and 3 GHz from the primary iodine transtion. The laser was carefully monitored for power and frequency drifts.

The resulting fluorescent signals for the various locations in the jet flowfield and laser detuning values are given in Table 6. The values in this table are normalized to a laser power of 735 milliwatts, the power delivered to the iodine molecules when the laser was tuned onto the primary iodine transition. The data in Table 6 is also adjusted by subtracting a background signal, produced primarily by the scatter of

the laser beam as it struck the quartz cell at a normal angle. The background signal was measured with the quartz cell completely evacuated and found to be 7.69×10^3 photons per second. This background signal is much larger than in the static cell measurements which employed a high quality optical window set at Brewster's angle for the laser beam access. Some scattered laser radiation was collected by the camera lens and was absorbed by the long pass filter, which then fluoresced at longer wavelengths and was collected by the detector, appearing as background signal. Improvements to the experiment would include the use of Brewster angle windows for laser access and dielectric long pass filters that would reflect the scattered laser light. Even with this large background signal, the signal–to–background ratio was adequate to make repeatable measurements throughout the flowfield for the desired values of detuning from the primary iodine transition. Table 6 is the data set to be used for the analysis of the detuning approach for measuring density in the underexpanded jet flowfield in the following section.

4.3.2 Analysis

The analysis of the fluorescent signal in the compressible flowfield is based on the theory of Section 2.3, as was the static cell analysis. Two additional considerations must be discussed that did not occur in the static cell analysis. All the considerations that arise in the analysis of the fluorescence data are included in the theory of Section 2.3. The difference in the static cell and gasdynamic analysis sections occurs in the parameters that must be allowed to vary in fitting the theoretical expression, Equation (2.24), to the experimental data. The first primary difference in the two experiments is that, in the jet flowfield, the iodine density is variable, since it remains a constant fraction of the total density. This is, of course, included in Equation (2.24) in the variable N_{I_2}. The second consideration in the gasdynamic experiment is the effect of the temperature variation. The temperature

Table 6

Fluorescent Signal (in photons per second) vs Distance, X (in mm), Along Centerline of Underexpanded Jet Flowfield At Indicated Values of Laser Detuning (in GHz). (Data normalized to 735 mW and adjusted by background signal of 7.69×10^3 photons per second.)

X(mm)	$\Delta\nu$=0 GHz	$\Delta\nu$=1 GHz	$\Delta\nu$=2 GHz	$\Delta\nu$=3 GHz
0.000	7.58×10^4	7.28×10^4	5.50×10^4	5.06×10^4
0.254	1.23×10^5	1.17×10^5	7.83×10^4	6.35×10^4
0.508	2.02×10^5	1.71×10^5	1.00×10^5	7.28×10^4
0.762	3.22×10^5	2.50×10^5	1.17×10^5	7.51×10^4
1.016	5.42×10^5	3.00×10^5	1.17×10^5	7.11×10^4
1.270	8.02×10^5	3.45×10^5	1.04×10^5	6.11×10^4
1.524	1.04×10^6	3.40×10^5	9.09×10^4	4.95×10^4
1.778	1.24×10^6	3.10×10^5	7.75×10^4	3.90×10^4
2.032	1.29×10^6	2.70×10^5	6.04×10^4	3.20×10^4
2.286	1.39×10^6	2.30×10^5	5.06×10^4	2.53×10^4
2.540	1.34×10^6	1.91×10^5	3.89×10^4	1.97×10^4
2.794	1.29×10^6	1.63×10^5	3.26×10^4	1.59×10^4
3.048	1.19×10^6	1.41×10^5	2.73×10^4	1.21×10^4
3.302	1.21×10^6	1.19×10^5	2.14×10^4	9.91×10^3
3.556	1.19×10^6	9.63×10^4	1.83×10^4	6.91×10^3
4.064	2.62×10^5	9.16×10^4	2.46×10^4	1.43×10^4

dependence is included in the theory of Section 2.3 and one needs only to include this variation in the numerical calculations. The temperature appears in several places in Equation (2.24). It appears in the Doppler width, in the population fraction f_1, in the quenching rate and in the collision width. The quenching and broadening constants were measured at a reference temperature of 298 K and are scaled according to Equations (2.27) and (2.28) to any other temperature. The Doppler width is easily calculated as a function of temperature using Equation (2.15), with the constant $\Delta\nu_{hyp}$, measured in the static cell, added to give the correct normalized detuning parameter D. The population fraction f_1 is calculated from Equation (2.29), using the molecular constants given in Appendix A.

Since it was found to be necessary to include more than the single primary iodine transition in detuning as much as 2 or 3 GHz in the static cell, the other two transitions occurring under the argon gain profile were also included in the numerical calculation. The relative strengths, or weighing factors, of the three transitions must be ascertained. At room temperature the line strengths are in the ratio 1 : 0.009 : 1.04, where the primary transition has unit strength. These line strengths are the product of the population, which is temperature dependent, and a constant, which is the Frank–Condon factor for the transition. At room temperture, the product of the population and Frank–Condon factors gives the ratio quoted above. At other temperatures the line strengths must include the appropriate Frank–Condon factors, which really occur in the B_{12} parameter of Equation (2.24), when adding contributions from several adjacent transitions. Taking this into account, the temperature–independent weighing factor ratios for the three transitions becomes, 1 : 0.023 : 0.32, with the primary transition again having unit strength. These ratios agree qualitatively with the Frank–Condon factor ratios calculated in Reference 38. Multiplying this weighing factor by the temperature–dependent population factor f_1, gives the correct line strength contribution for the three separate transitions.

Except for this distinction, and the different molecular constants appearing in the population factor, the three transitions are treated equally in the numerical calculations. That is, the same values of quenching, broadening and hyperfine-width constants are used for each transition and the resulting contribution from each transition is calculated according to (2.24) and the result summed to give the total fluorescent signal. It was found that the three iodine transitions must be included in the calculation of the fluorescence distribution in the jet flowfield since the contributions from the two secondary transitions were significant for the large values of detuning from the primary transition that were used in the experiment.

In doing the numerical calculations, and in interpeting the results, it is convenient to rewrite Equation (2.24) for the fluorescent signal as

$$S_F = (Constant)\ Factor(p,\ T,\ \Delta\nu)\ N_{I_2}\,, \tag{4.2}$$

where

$$Factor = \frac{f_1}{\Delta\nu_D}\,\frac{1}{1+Q/A_{21}}\,V(D,B) \tag{4.3}$$

and

$$Constant = \eta h\nu \frac{\Omega}{4\pi} V_c \sqrt{\frac{4(\ln 2)}{\pi}}\,\frac{B_{12}}{c}\,I\,.$$

Writing the equation in this manner places all the complications of variable pressure and temperature in the fluorescence *Factor*. Note that it is assumed that the saturation effects are small in the writing of Equation (4.2), as in the static cell case. Actually, the full expression (2.24) was numerically evaluated and it was confirmed that saturation effects were, in fact, negligible in the jet flow as in the static cell. A Fortran program was written that employed the above expression for the fluorescent signal, with the constants determined from the static cell curve fits and the pressure,

temperature and density variation given in Table 5. It is most straightforward to calculate a normalized fluorescent signal. One way to do the normalization is to ratio the fluorescent signal at a location in the flowfield and at a given value of laser detuning to the value of the fluorescent signal at the nozzle exit for that same value of detuning. This was done numerically as follows. The flourescence *Factor* was calculated at the nozzle exit plane for a given value of the laser detuning. The value of *Factor* at subsequent locations downstream of the nozzle exit were then divided by the exit plane value of *Factor*. The iodine density then appears in the normalized fluorescent signal expression as the ratio $N_{I_2}/N^*_{I_2}$, where $N^*_{I_2}$ is the density at the sonic point, or at the nozzle exit. In this way the fluorescent signal is normalized and the *Constant* cancels out, such that for each value of laser detuning the calculated fluorescent signal starts with a value of unity at the nozzle exit. The results of these calculations are given in Figure 12. The experimental data is also included in the figure and is normalized in the same fashion, so that each detuning curve begins with a value of unity at the nozzle exit. The horizontal axis is rescaled by dividing the downstream distance X, in mm, by the jet diameter, 1.5 mm. These curves are simply the product of the fluorescent *Factor* and the iodine density, but normalized by their values at the nozzle exit. This figure is discussed in detail in the following section.

4.3.3 Discussion

The fluorescence distribution curves in the compressible jet flowfield are very interesting and serve to illustrate both the problem imposed by quenching when using laser–induced fluorescence to measure density and the consequences of detuning in cancelling this quenching dependence. It is evident from Figure 12 that the theory used to predict the fluorescent signal and the constants derived in the static cell measurement do a fairly good job of predicting the fluorescence distribution in

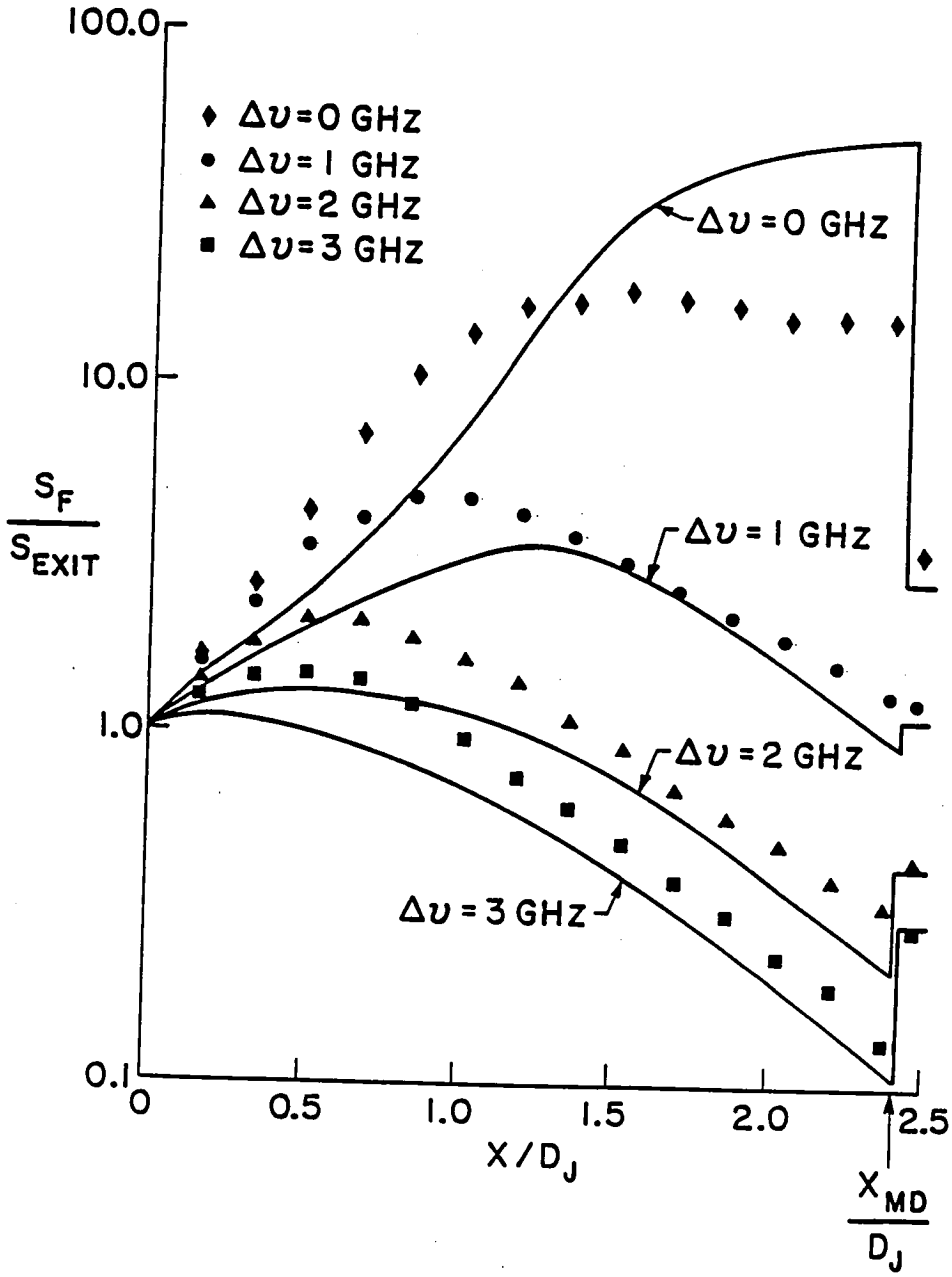

Fig. 12. Normalized Fluorescent Signal versus Position in Jet for Four Values of Laser Detuning from Primary Iodine Transition. (Theory shown by solid lines and data by points.)

the jet flowfield. There is some discrepancy between the theory and the data near

the jet exit. This discrepancy agrees with the discrepancy that occurred in the static cell fits at pressures above about 200 torr, where the theory underpredicted the data (see Figure 8). Therefore, the constants derived from the static cell experiment fit the data well at lower pressures but are slightly in error at the higher pressures. Since the pressures in the jet are above 200 torr until about $X/D_J = 0.6$, the theory does not match the data in the jet as well in this region. The other discrepancy one notices is that the theory overpredicts the data for zero detuning in the high Mach number region of the flowfield. The experimental data is inconclusive about the reason for this discrepancy. However, it is felt that the major reason was the measured laser frequency drift of about 100 MHz that occurred duing the collection of the data for the zero detuning curve. Since the iodine linewidths are on the order of 260 MHz in the high Mach number region of the flow this much laser drift would account for the factor of three reduction in fluorescent signal from the desired case of zero detuning. Overall, the agreement between the theory and the data is good, considering the large variation in the flowfield parameters (see Table 5) and the very small jet flow being probed in the experiment. Note that the abrupt change in the signal across the sudden recompression represented by the shock wave is even well predicted by the theory. It is obvious that the agreement is good enough to draw some conclusions from the theory as to why the signal behaves as it does in the jet flowfield as the laser is detuned. This is the subject of the remainder of this section.

For a zero value of detuning, the fluorescent signal is seen to increase rapidly downstream from the jet exit. However, the density is known to decrease monotonically with this distance along the jet centerline. This is a dramatic illustration of the effect of quenching on the fluorescent signal in a compressible flow. The reason for the discrepancy between the known decrease in density and the increase in fluorescent signal is seen most easily by reference to the fluorescence *Factor* given in Equation (4.3). The variation of this *Factor* with position in the jet is given in

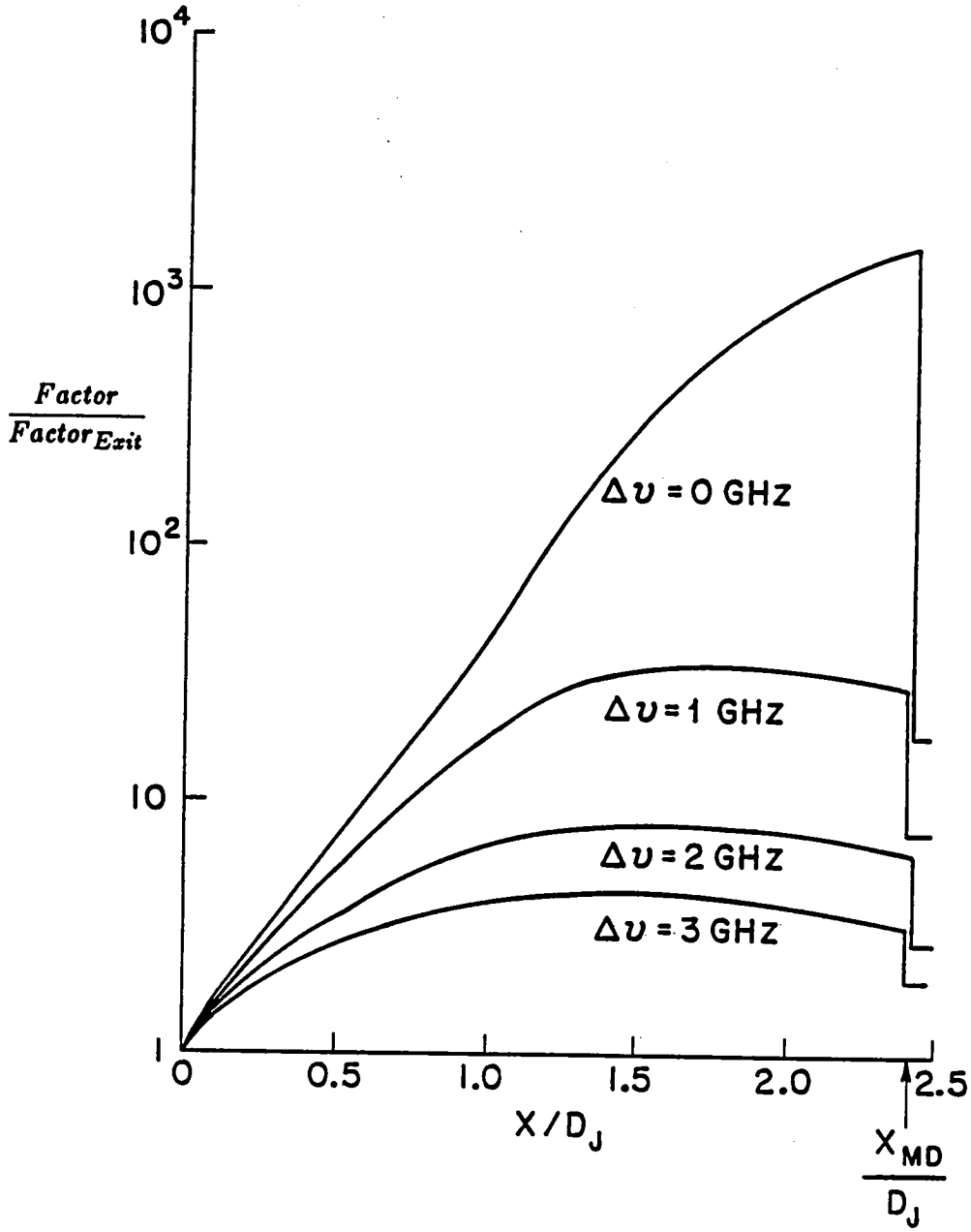

Fig. 13. Normalized Fluorescence *Factor* versus Position in Jet for Four Values of Laser Detuning (theory)

Figure 13. It is this *Factor* that multiplies the density to produce the fluorescent signal. For a value of zero detuning, this normalized *Factor* increases from unity at the jet exit to about 1500 just before the shock wave. The density decreases

by a factor of about 30 over this distance. Therefore, the signal will not track the density at all, but will increase due to the dominant fluorescence *Factor*. The reason the *Factor* increases so rapidly as the pressure decreases in the jet is that both the Stern–Volmer factor and the Voigt integral vary roughly inversely with pressure for zero laser detuning (in the high pressure regime where $Q/A_{21} \gg 1$). Thus, the *Factor* varies approximately as the inverse square of the pressure from the jet exit and this dominants the density decrease. In this discussion it is easiest to think of the pressure dependence of the *Factor*, much as in the static cell, even though the temperature varys as well. One can do this since the temperature variation in the jet is less than the pressure variation and the temperature dependence of the fluorescent signal is weaker than the pressure dependence. The *Factor* increases more slowly in the more rarefied part of the jet where $Q \approx A_{21}$.

The effect of detuning on the fluorescent signal is seen most easily by reference to the asymptotic form of the *Factor* for large detuning, D. Using the limiting form for the Voigt integral given in Equation (2.30), we can write (4.3) for the *Factor* for large laser detuning as

$$\lim_{D \gg 1} Factor = \frac{1}{\sqrt{\pi(\ln 2)}} f_1 \frac{1}{1 + Q/A_{21}} \frac{\Delta\nu_c}{4\Delta\nu^2 + \Delta\nu_c^2}. \tag{4.4}$$

This, of course, agrees with Equation (2.31), with the added definition of *Factor* for convenience in the discussion in this chapter. For large enough values of the laser detuning, $\Delta\nu$, the pressure and temperature dependence of the quenching and the broadening cancel and the *Factor* becomes a constant in the jet flowfield. This is precisely what is seen to occur for the detuning of 3 GHz in Figure 13. The *Factor* is roughly constant over the central half of the jet flowfield. The *Factor* is not constant near the jet exit since the pressure is high there and this value of detuning is not sufficient to dominant the collision width in the denominator of

(4.4). Also, the *Factor* decreases slightly in the rarefied part of the jet where $Q \approx A_{21}$. Therefore, as the laser detuning is increased, the *Factor* becomes constant for a major portion of the flowfield, and the fluorescent signal becomes proportional to the density directly. It is for this reason that the fluorescence distribution in Figure 12 begins to show a decrease with distance from the nozzle exit, in accordance with the decrease in the density.

The agreement between the fluorescence signal decrease and the density decrease with distance along the jet centerline, for a laser detuning of 3 GHz, is shown in Figure 14. In this figure the fluorescent signal and the data are renormalized to the point in the flowfield where the *Factor* is most nearly constant ($X/D_J = 1.35$), since it is in this region that the signal tracks the density. It is seen that both the theory and the data agree well with the calculated density variation in the jet flowfield for values of X/D_J greater than about one. The fluorescence would agree with the density distribution closer to the jet exit, where the pressures are greater, if the value of the laser detuning could be increased. However, beyond 3 GHz from the primary iodine transition, one approaches the other strong transition (located 6.42 GHz away) and the detuning effectively begins to decrease. Therefore, for this portion of the iodine spectrum at 5145 Å, one is limited to about 3 GHz detuning and density measurements at Mach numbers greater than about 2.0 (at $X/D_J \approx 1.0$) in this flowfield.

We have, up to this point in the discussion, concentrated on the pressure dependence of the *Factor* and the resulting effect of laser detuning on cancelling the quenching and broadening effects. The temperature and velocity variations in this jet flowfield also have very important effects on the fluorescent signal. The temperature decrease in the jet flow has two primary effects on the fluorescence. First, it affects the strengths of the iodine transitions through the fraction, f_1, which gives the fractional population of the initial level of the particular transition. It was

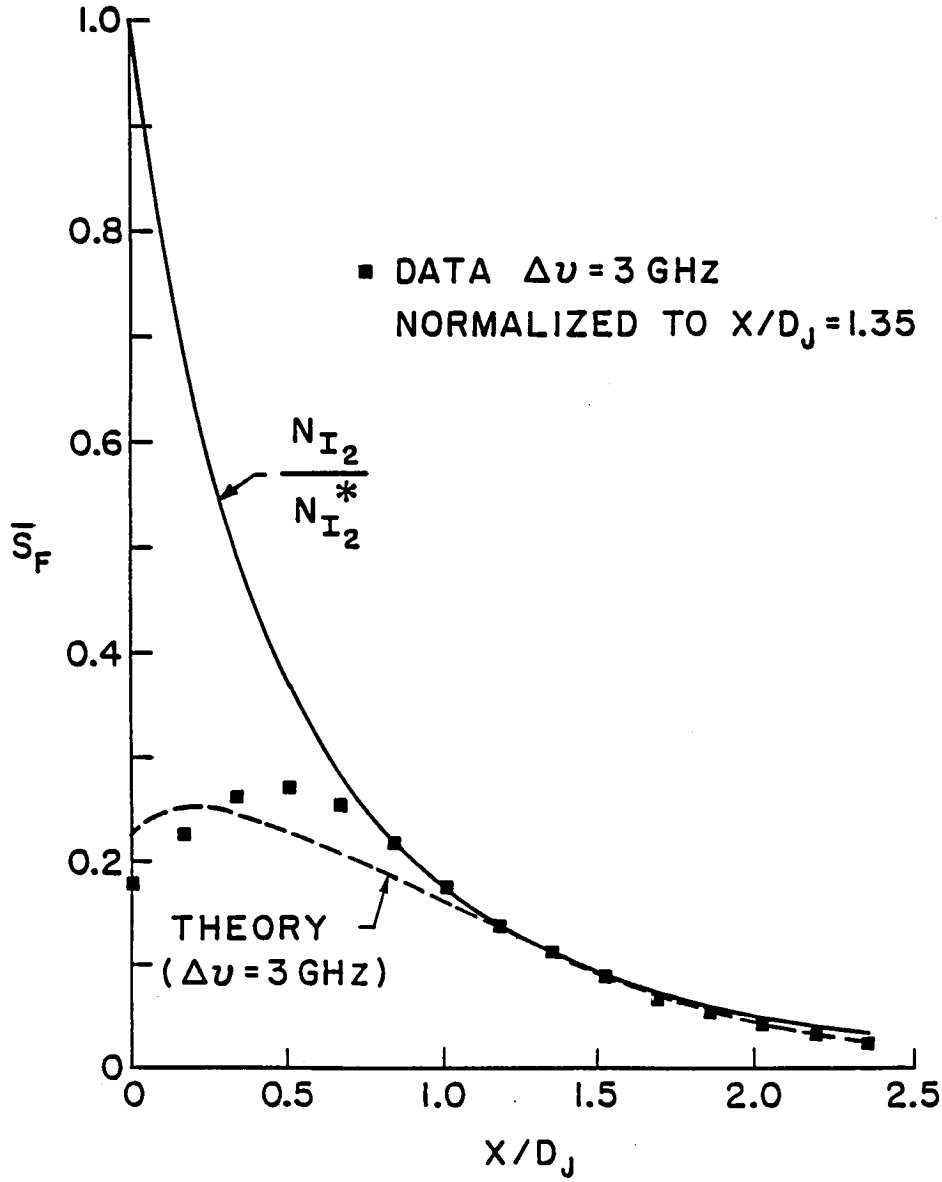

Fig. 14. Fluorescent Signal and Density versus Position in Jet ($\Delta\nu = 3$ GHz, normalized to $X/D_J = 1.35$)

noted in the static cell analysis that the hot–band transition had to be accounted for in explaining the room temperature data. In the jet flowfield this hot–band rapidly depopulates as the temperature decreases and the calculations show that, for the 2 and 3 GHz detunings, this transition contributes five orders of magnitude less than

the primary transition to the total signal. Therefore, the hot-band transition has essentially no affect in the data taken in the cold flowfield, whereas it was important in the static cell. It should also be noted that the factional population in the primary transition grows by a factor of about 10 as the temperature decreases in the jet. The second temperature effect in the jet is *very* important. The reason that the asymptotic form of the *Factor* is a good description of the data at a detuning of 3 GHz is that the detuning D is normalized by the Doppler width. Since the Doppler width decreases as the square root of the temperature, the effective detuning in the jet, corresponding to an actual laser detuning of 3 GHz from line center, becomes 9.3 in the coldest part of the jet flowfield. As pointed out in Reference 21, the asymptotic approximation to the Voigt integral is good to two significant figures for D=10. The cold temperatures, therefore, serve to increase the detuning parameter D and make the asymptotic approximation very accurate at a laser detuning of 3 GHz in the jet flowfield.

The distribution of the convective velocity in the jet flowfield does not enter into the expression for the fluorescent signal. (The thermal velocity distribution was accounted for by the inhomogeneous broadening represented by the Doppler width.) The convective velocity can have at least two important effects on the resulting fluorescent signal, however. The preceeding discussions have assumed that the convective velocities in the flowing jet are all normal to the laser beam. If the molecules have components of their convective velocity in the direction of the laser beam, a Doppler shift of the entire transition occurs. For the purposes of this work, all measurements were made along the jet centerline and, therefore, the convective velocities of the molecules probed were all normal to the laser beam. Therefore, no Doppler shift of the transition need be considered in analysing the data. The Doppler shift will, however, be illustrated in a figure at the end of this section. The other effect of the convective velocity in the jet is a bit more subtle. It concerns

the effective pumping time of the molecules by the laser beam as they convect past the focused laser beam at high velocities. The velocity in the jet flowfield varies from 321 m/sec at the jet exit to 699 m/sec just before the shock wave. One can easily calculate the transit time of the molecules as they pass through the laser beam focused to a diameter of about 27 μm. The transit times vary from about 84 nsec at the jet exit to 39 nsec just before the shock wave. The lifetime of the iodine molecule depends on pressure and temperature in the jet and is estimated to vary from a few nsec at the exit to a few hundred nsec before the shock wave. Therefore, the ratio of the transit time to the molecular lifetime varys from more than ten at the exit to slightly less than one at the shock wave. This is simply the ratio of the laser pumping time to the molecular lifetime and is the ratio to be considered when deciding when the steady–state solution to the rate equations applies. The steady–state solution is valid as long as the laser pumping time is much longer than the molecular lifetime. If the velocities are high and the lifetimes long, the steady–state solution must be reexamined. In effect, one is then using a short pulse to excite the molecules and the fluorescence may not have reached its steady–state value, due to the short laser pumping times. The short–pumping effect is not important in this work since the laser pumping times were on the order of, or greater than, the molecular lifetimes in the underexpanded jet flowfield. However, one must consider this effect of the convective velocity when probing very high velocity flows with tightly focused laser beams, when the molecular lifetimes are relatively long.

The distribution of the fluorescent signal with position in the underexpanded jet flowfield is now understood. For zero values of laser detuning, the fluorescence *Factor* grows rapidly, since it varies approximatedly as $1/p^2$ near the jet exit. The fluorescent signal, therefore, increases while the density decreases with distance downstream from the jet exit. For a detuning of 3 GHz, the maximum possible detuning for this part of the iodine spectrum, the fluorescence *Factor* becomes nearly

independent of pressure and temperature, as predicted by the asymptotic form, Equation (4.4). The asymptotic formulation is an excellent approximation at this value of detuning due to the reduced temperature in the flowfield. The resulting fluorescent distribution was seen to agree well with the density distribution for downstream distances greater than about one nozzle diameter, a limit placed by the available laser detuning at 5145 Å.

All of these results show good agreement with the theory of Chapter 2, but, as it is certainly true that a picture is worth a thousand words, photographs were taken of the jet flowfield that clearly illustrate the preceeding discussion. By replacing the spherical focusing lens in the experimental setup by a cylindrical lens, a sheet of laser light was used to excite fluorescence in a cross-sectional plane of the jet flowfield and photographed using a camera equipped with a macro lens. The results are shown in Figure 15. The top photograph at zero detuning illustrates very clearly that the fluorescent signal is not proportional to the iodine density when the laser is tuned to line center. The signal is seen to increase with distance downstream and then suddenly decrease as the molecules cross the shock wave and the fluorescence is quenched. The bottom photograph at 3 GHz shows that the signal does, in this case, decrease with distance from the nozzle, and, as discussed above, is representative of the density distribution in the jet cross section, except near the nozzle. Additionally, the fluorescent signal in the bottom photograph increases across the shock wave, in step with the density. The dramatic difference in these two photographs, for a laser detuning of only 3 GHz, illustrates well the effectiveness of the detuning approach for cancelling the quenching effect when using laser-induced fluorescence for the measurement of density in compressible flows.

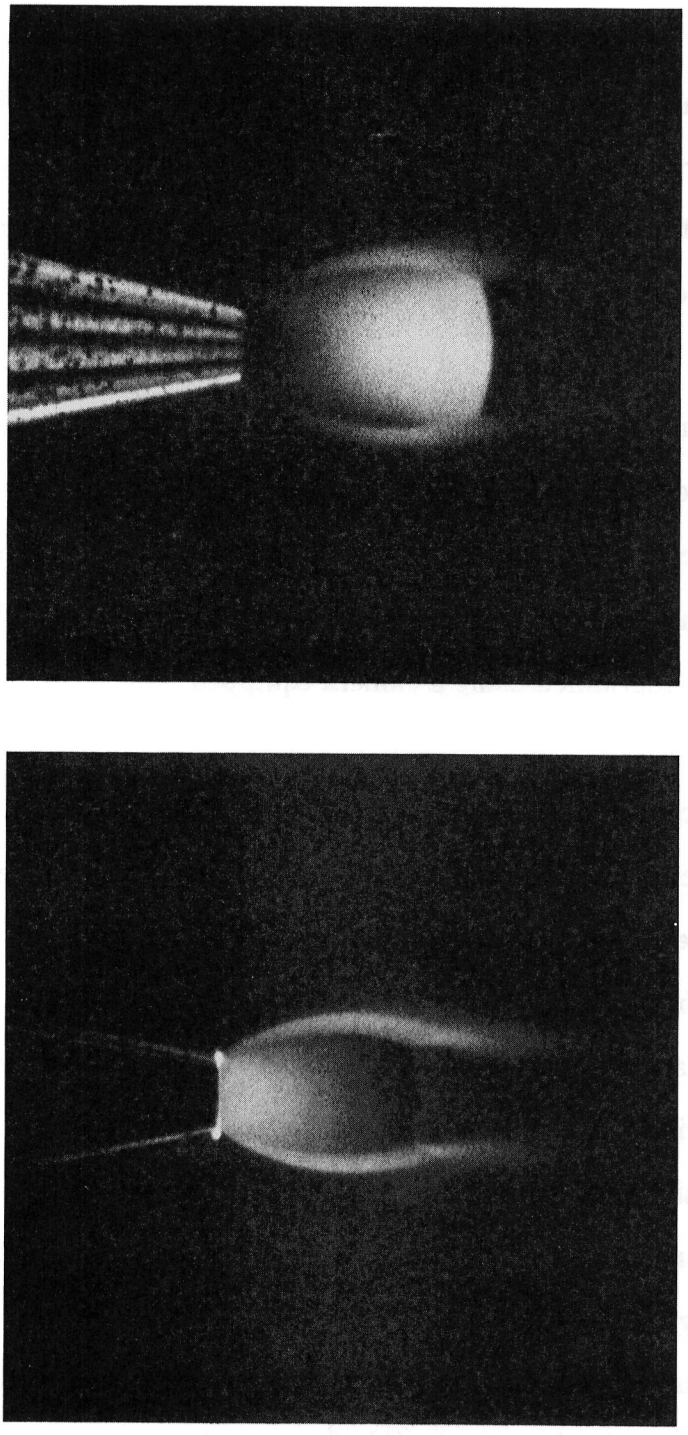

Fig. 15. Photographs of a Cross–Section of an Underexpanded Nitrogen Jet, Seeded with Iodine, for Laser Detunings of Zero (top photo) and Three (bottom photo) GHz

Figure 16 illustrates the effect on the fluorescence distribution of detuning the laser frequency by ± 500 MHz from the iodine line center. At the lower frequency the half of the jet nearest the laser emits a much stronger fluorescence. This effect is due to the Doppler shift of the iodine transition resulting from the velocity component of the iodine molecules in the direction opposite to the laser beam and produces a shift of their transition to higher frequencies. For a velocity of 700 m/sec at an angle of 20 degrees with respect to the jet centerline, the magnitude of the Doppler shift is about 500 MHz, or about half the iodine linewidth. These molecules are Doppler shifted by +500 MHZ, thereby cancelling the –500 MHz detuning and, thus, emit a bright fluorescence characteristic of line center excitation. The molecules in the other half of the jet are Doppler shifted by 500 MHz also, but to lower frequency. They experience an effective detuning of –1 GHz, or about one iodine linewidth and, thus, emit a lower fluorescent signal. The opposite effect occurs for a detuning of the laser to higher frequency. The molecules moving along the jet centerline have no component of velocity in the direction of the laser beam and, therefore, experience no Doppler shift. The Doppler shift of the fluorescence spectrum of sodium has been used by Zimmerman and Miles [39] to measure the velocity in a hypersonic flow of helium seeded with sodium molecules.

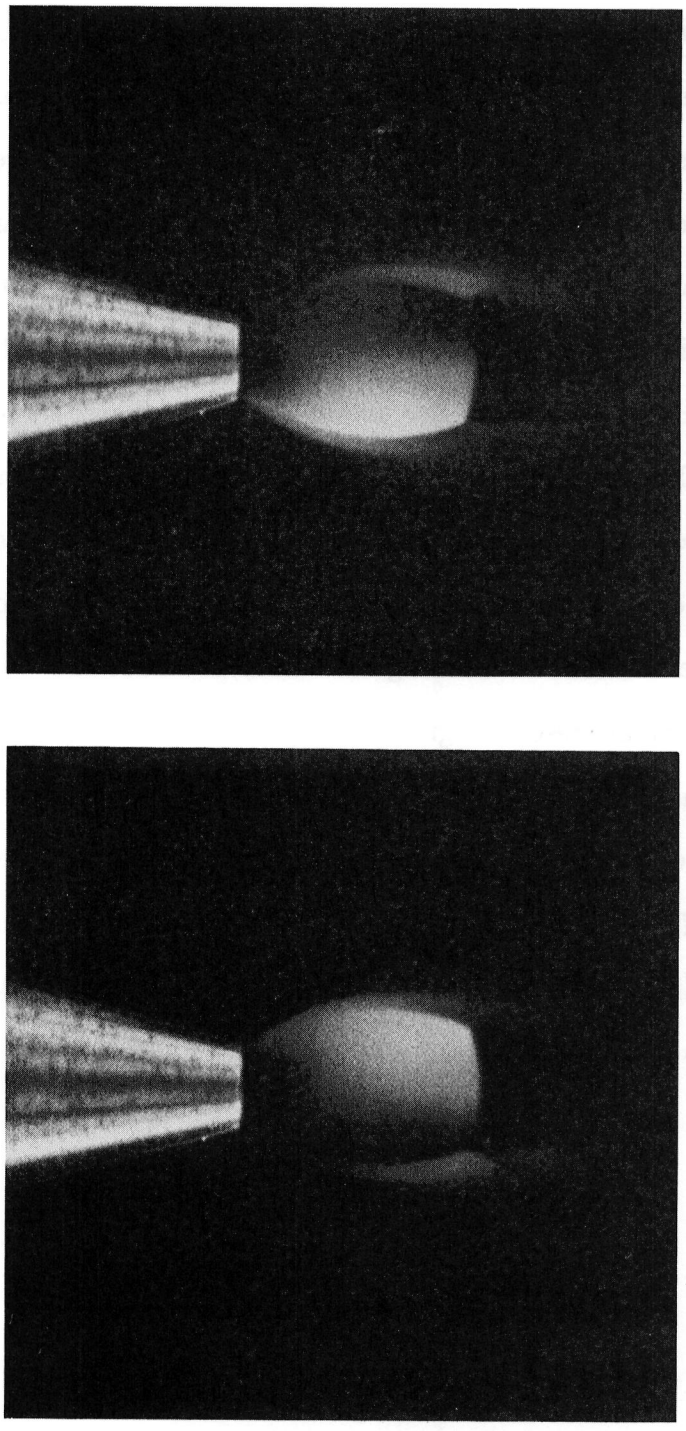

Fig. 16. Photographs of a Cross–Section of an Underexpanded Nitrogen Jet, Seeded with Iodine, for Laser Detunings of ± 500 MHz

Chapter 5

Conclusions and Recommendations

The application of laser–induced iodine fluorescence has been investigated in this work. A theory was developed in Chapter 2 for the fluorescence induced in iodine by a laser of arbitrary bandwidth and intensity. The complication of quenching in interpeting the fluorescent signal in terms of the iodine density in a compressible flowfield was discussed. Two solutions to the quenching problem were examined in that chapter: saturation and frequency detuning. Chapter 3 discussed a comparison of experimental results for the saturation approach with the theoretical predictions. In Chapter 4, additional experiments were compared with theory which allowed an evaluation of the application of the frequency detuning approach to the elimination of the quenching problem.

Conclusions about the usefulness of laser–induced fluorescence for the measurement of density in compressible flows resulted from a comparison of the experimental results in Chapters 3 and 4 with the theory of Chapter 2. The saturation approach, although very attractive theoretically, since the quenching is completely eliminated at full saturation, appears in practice not to be a viable approach for measurements at pressures of interest in gasdynamics and with laser beams of Gaussian transverse intensity distribution. The saturation intensities are relatively large for pressures near one atmosphere (even for the case of iodine, which has a modest saturation

intensity compared to most molecules) and only a small percentage of the molecules at the center of the laser beam are saturated, due to the Gaussian beam effect. Therefore, in practice, the quenching dependence is not significantly altered by the saturation approach, for the conditions of interest in this work.

The detuning approach was shown to produce a cancellation of the quenching by the collisional broadening, as predicted by the theory for asymptotically large frequency detunings. For a detuning of 3 GHz in the test compressible flowfield, the fluorescent signal was seen to be proportional to the iodine density over a significant portion of the flowfield. The low temperatures that exist in high Mach number flows serve to effectively increase the laser detuning by reducing the Doppler width, making the asymptotic solution a good approximation for a detuning of even 3 GHz. The detuning was limited in this work to 3 GHz, due to the closely–spaced iodine transitions under the 5145 Å argon laser gain profile. As a result, the quenching dependence was cancelled by the broadening only for pressures less than about 200 torr in the compressible flowfield. The signal strength resulting from detuning 3 GHz was only about a factor of five less than the zero detuning value, at a pressure of 200 torr. Therefore, it was found that the pressure and temperature dependence of the fluorescent signal could be removed and reasonable signal levels retained by the detuning method. The scheme of frequency detuning a narrow bandwidth laser from the line center of a seed molecule is, thus, concluded to be an attractive approach for the measurement of density in compressible flows using the laser–induced fluorescence technique.

It is further concluded that iodine is an attractive seed molecule since it is easy to insert into a flowfield and has a convenient visible absorption spectrum. The toxicity and reactivity of the molecule can be easily dealt with in the laboratory situation.

It is recommended that laser–induced fluorescence be further explored as a

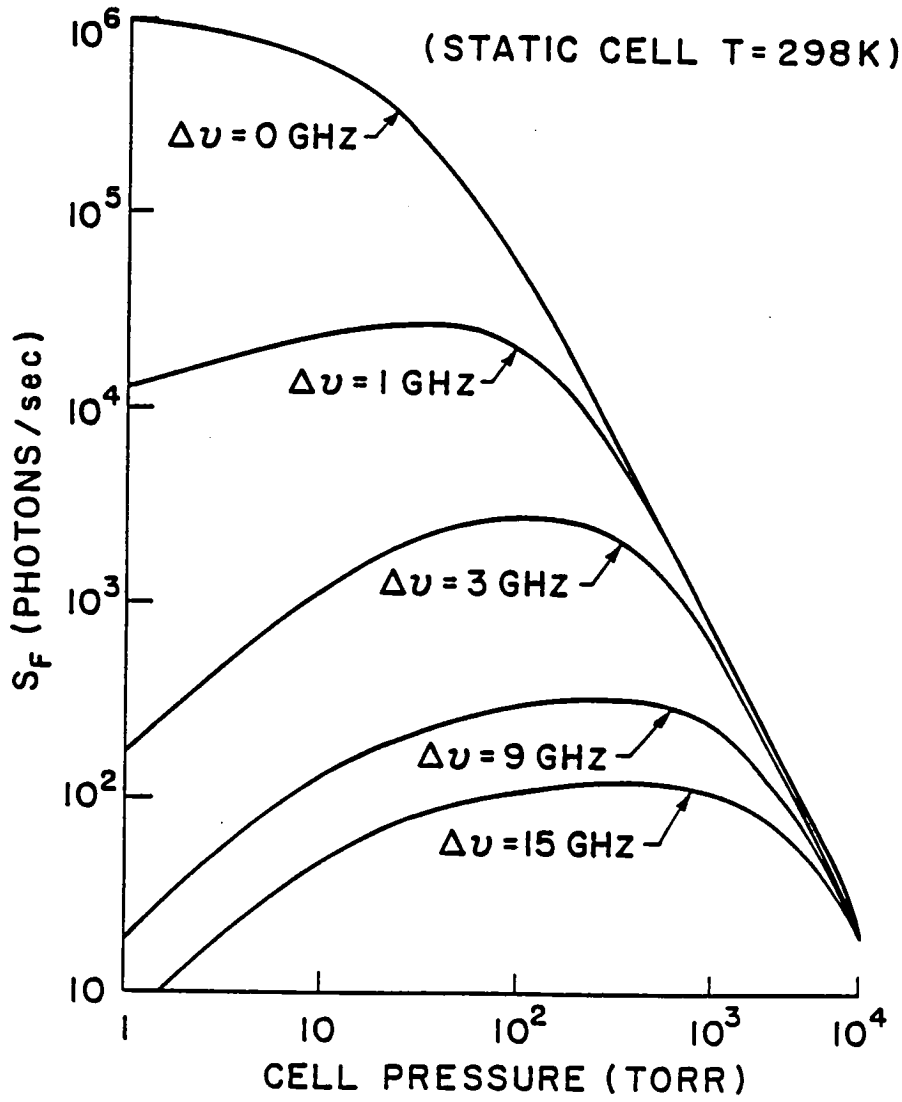

Fig. 17. Detuning Calculations from an Isolated Iodine Transition

diagnostic technique for the measurement of density in iodine-seeded compressible flows. The frequency detuning approach can be made more effective and the measurement capability extended to higher pressures than possible in this work by using iodine transitions that are more isolated, allowing greater values of detuning to be employed. Figure 17 shows calculations of the fluorescent signal for larger

detunings from a single isolated iodine transition. It is seen in this figure that a detuning of 15 GHz in a room temperature flow causes the fluorescent signal to be proportional to the density over a pressure range of about 100 to 1000 torr. In addition, at one atmosphere less than an order of magnitude signal decrease occurs compared to the case of line center excitation.

Strong iodine transitions with more spectral isolation are available [40] and are accessible with tunable dye lasers. In selecting an iodine transition for this application, one must consider the quantum numbers of the transition. A ground state vibrational transition is desired (to avoid depopulation in cold flows) and a value of the rotational quantum number is desired that will minimize the temperature dependence of the line strength that remains in the asymptotic solution to the fluorescent signal for large detuning. By employing a cw tunable dye laser, detuned several GHz from an isolated iodine transition, measurements of density and density fluctuations can be made at a point in a compressible flowfield. For the measurement of the density distribution in a plane of an iodine–seeded compressible flowfield, pulsed dye lasers would provide higher peak powers and allow the use of gated detection for the taking of instantaneous two–dimensional photographs with good signal–to–noise ratios.

In addition to tunable dye lasers, the second harmonic of the solid state Nd:Yag laser, at 5320 Å, is *very* attractive for density measurements in iodine–seeded compressible flows. The iodine spectrum at 5320 Å, within the tuning range of such a laser (containing an etalon in the laser cavity for narrowing the laser bandwidth and providing tunability), contains two strong ground vibrational transitions with rotational quantum numbers of about 53 (ideal values for flows at about Mach 2). These iodine transitions are separated by about 44 GHz [41], allowing detunings of up to about 20 GHz with large laser peak powers. There are several weak transitions in between the two strong transitions but these all have large rotational quantum

numbers and, therefore, will depopulate in cold, high Mach number flows and not restrict the available detuning of 20 GHz. Such a laser system can be run pulsed at high repetition rates for density measurements with temporal resolution at a point or in a plane. Other laser systems (such as metal vapor and excimer lasers) are becoming available that possess large peak powers and high repetition rates and should be considered for this application. The critical characteristics of these laser systems that must be examined are the portion of the iodine spectrum that they can access and the laser bandwidth and tunability possible.

Ultimately, one would like to use tunable UV lasers for laser–induced fluorescence measurements in oxygen or nitrogen. Once such laser sources are available with adequate power, density measurements will become a possibility without the need to seed the air flow with other molecules. Until that time, the seeding of iodine and the use of the detuning approach with available laser sources is an attractive approach for measuring density in compressible flows while avoiding the quenching complication. This work is considered an initial investigation of the approach and a verification that the approach is viable, both in theory and in practice.

Appendix A

Basic Spectroscopy of the Iodine Molecule

Introduction

This appendix contains the basic information about the spectroscopy of the iodine molecule that is needed in this work. The content of this appendix is based on an extensive literature search and on spectrally–resolved measurements of the fluorescence from iodine when excited by 5145 Å radiation from the argon ion laser.

Energy Level Scheme

The visible absorption spectrum of the iodine molecule is due to a transition in the electronic structure from the ground state, $X^1\Sigma_g^+$, to an excited state, $B^3\Pi_u^+$. Figure 18 shows the potential energy curves for the bound X and B electronic states and the unbound D state. The B–X transition is between states of different electronic spin and is, therefore, weakly allowed. This is the reason for the relatively long radiative lifetime of the B state (about 10^{-6} seconds) compared to a typical visible radiative lifetime (about 10^{-8} seconds).

The electronic states are composed of many vibrational and rotational substates. The energy of the various vibrational and rotational substates can be expressed as the sum of the electronic term energy, the vibrational energy (harmonic

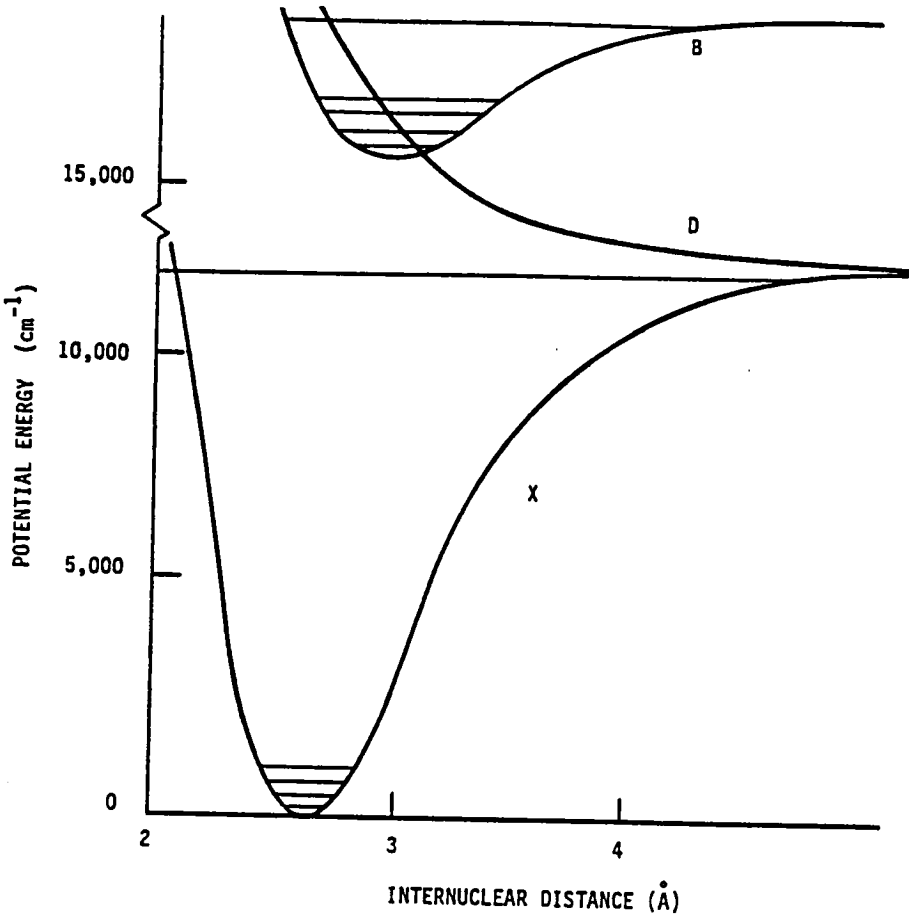

Fig. 18. Potential Energy Curves of the X, B, and D States of Iodine

form plus anharmonic correction), and the rotational energy (rigid rotor form plus vibrational–rotational coupling correction). The expression for the energy of a X or B substate which has a vibrational quantum number v and a rotational quantum number J is written as

$$E = T_o + w_o v - w_o x_o v^2 + B_e J(J+1) - \alpha_e (v + 1/2) J(J+1),$$

where T_o is the electronic term energy, w_o is the harmonic vibrational constant, $w_o x_o$ is the anharmonic vibrational constant, B_e is the rigid rotor rotational constant

and α_e is the vibrational–rotational coupling constant. Values for these various molecular constants for the X and B states of the iodine molecule are tabulated in Table 7 [42],[43]. Using these molecular constants and the above expression, the energy in wavenumbers above the lowest energy X state can be calculated for any X or B vibrational and rotational substate.

At thermal equilibrium each energy mode (electronic, vibrational, and rotational) is in a Boltzmann equilibrium, with the populations of the various energy levels being determined by the energy level spacing and the temperature. The fraction of the total population that is in a particular sublevel of the ground electronic state is given by Equation (2.29), where the vibrational energy is given by $E_v = w_o v - w_o x_o v^2$ and the rotational constant is given by $B = B_e - \alpha_e(v+1/2)$ with the X state constants from Table 7. At room temperature 66 % of the vibrational population is in the ground vibrational level, 23 % in the first excited vibrational level, 8 % in the second excited level and the other 3 % in the higher levels. The rotational level with maximum population at a given temperature is given approximately by

$$J_{max} = 0.59\sqrt{\frac{T(\mathrm{K})}{B(\mathrm{cm}^{-1})}}.$$

At room temperature J_{max}=53 and at T=50 K, J_{max}=22, as the population shifts toward lower J levels with decreasing temperature. Equation (2.33) determines the value of J which is least sensitive to temperature changes around a mean

Table 7

Iodine Molecular Constants for the X and B States (in cm^{-1})

Electronic State	T_o	w_o	$w_o x_o$	B_e	α_e
X	0.0	214.5	0.615	0.0374	1.13×10^{-4}
B	15770.5	125.0	0.693	0.0290	1.56×10^{-4}

temperature $\overline{T}$. Using the value for the rotational constant of the X state indicates that J=73 is the least temperature–sensitive level at T=298 K and J=30 is least sensitive at T=50 K. The rotational distribution also contains a 7:5 population alteration for J odd:even, due to the nuclear statistical weights, which is not included above.

Spectra

Absorption Spectrum (general)

Absorption can occur from any populated ground vibrational and rotational substate to an excited substate, as allowed by the selection rules and with a transition strength determined by the overlap of the vibrational wavefunctions (Frank–Condon factors). The rotational selection rule for a homonuclear diatomic, such as iodine, is $\Delta J = \pm 1$. Each transition is, therefore, made up of a P ($\Delta J = -1$) and a R ($\Delta J = +1$) branch. At room temperature there are about 150 rotational levels with significant population, each producing a P and a R absorption line. With population in the first three vibrational levels of the X state, there are thus about 70,000 absorption lines in the visible (500–650 nm) B–X absorption spectrum of iodine. The density of the spectrum derives from the closely–spaced vibrational and rotational energy levels for this heavy diatomic molecule.

At room temperature the absorption lines are Doppler–broadened with a Doppler linewidth given approximately by

$$\Delta\nu_D = 7.0 \times 10^{-7} \sqrt{\frac{T(\mathrm{K})}{m(\mathrm{amu})}}\, \nu_o ,$$

where ν_o is the frequency of the absorption transition. For iodine, $m = 254$ amu and the room temperature Doppler width is 442 MHz at 5145 Å. In a sub–Doppler

absorption spectrum [44], it is seen that each even J level is split into 15 hyperfine components and each odd J level into 21 components due to the interaction of the total nuclear spin, I, and the rotational quantum number, J.

Fluorescence Spectrum (general)

For each excited vibrational level that is populated by absorption, a vibrational progression of fluorescent bands to the various ground vibrational levels will occur with strengths determined by the Frank–Condon factors. Each excited rotational component gives rise to a P and R fluorescent doublet spaced by about one wavenumber in energy. The fluorescent spectrum is thus very complicated if several vibrational and rotational levels are populated in the excited B state.

Spectra at 5145 Å

The part of the iodine absorption spectrum which coincides with the 10 GHz argon ion laser gain profile at 5145 Å is shown in Figure 19. Within this argon tuning range lies three ground vibrational state transitions and one hot–band transition. The ground state (43,0) transition is located 2.0 GHz to the high frequency side of the argon line center. This transition consists of the overlapping P13 and R15 rotational components. Located 2.47 GHz to the lower frequency side of this transition is the R98 (58,1) hot–band transition. At the far low frequency edge of the argon gain profile are two overlapping ground vibrational state transitions, the P48 (44,0) and P103 (49,0), located 6.42 GHz from the other ground state absorption line. The overlapping (43,0) transitions are strong and, fortunately, occur near the center of the argon gain profile so that the available argon output power at this frequency is large. This absorption line is the one of primary interest in this work. The P13 and R15 transitions, which overlap to make up this line, each have 21

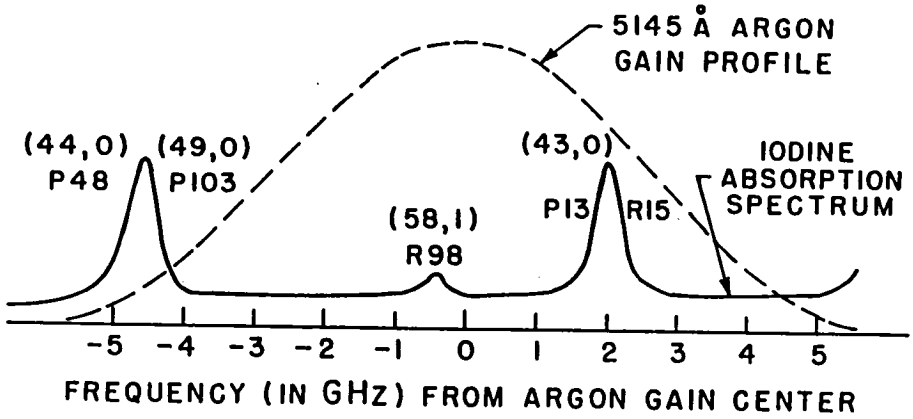

Fig. 19. Iodine Transitions under Argon Gain Profile at 5145 Å

hyperfine components spread over about 1.2 GHz [44]. This hyperfine width adds to the room temperature Doppler width to give the line an overall linewidth of about 1.6 GHz. Each component also pressure broadens at about 12 MHz per torr, giving a total linewidth of about 10 GHz (FWHM) at one atmosphere pressure and room temperature.

The low pressure fluorescence spectrum of iodine due to the pumping of the (43,0) transitions contains a progression of vibrational bands. Figure 20 shows the 5145 Å–excited progression, through the second Stokes fluorescence band, from a room temperature iodine cell with no background pressure. The transitions are very sharp and are spaced by the vibrational spacing of the ground state. Each Stokes band under high resolution is seen to appear as a triplet, as shown in Figure 21 for the second Stokes band at 5260 Å. There are actually four fluorescent transitions that make up this Stokes band: a P and R fluorescent transition for both the P13 and R15 absorption lines; however, the P13 and R15 fluorescent transitions overlap to within the resolution of the spectrometer used to record the spectrum, giving the band the appearance of a triplet. Figure 20 also shows the affect on the fluorescent

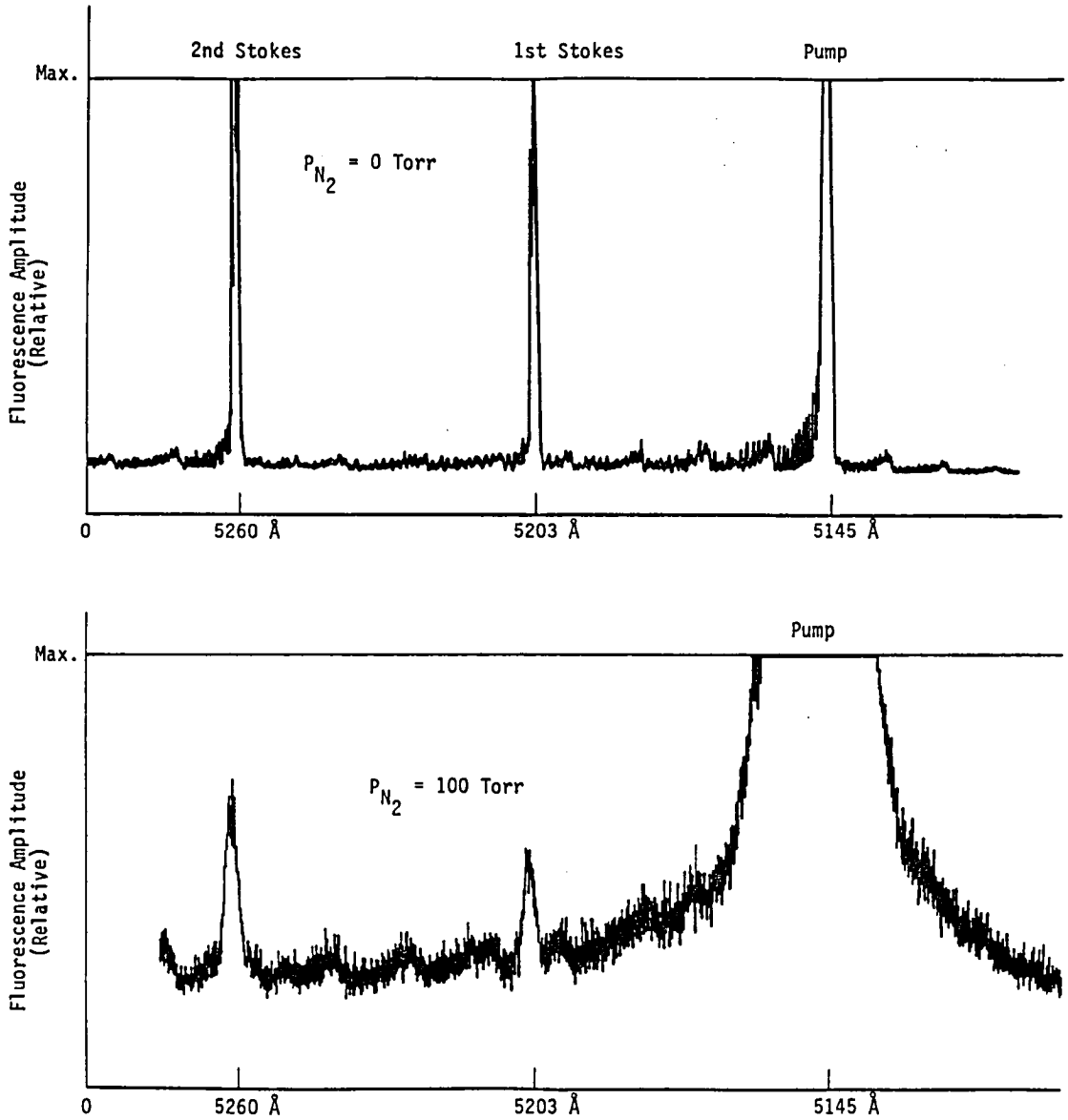

Fig. 20. Iodine Fluorescence Spectrum Through Second Stokes Component for Zero Nitrogen Pressure (upper trace) and 100 Torr Nitrogen (lower trace)

spectrum of adding buffer gas to the iodine cell. The lower spectrum was recorded after 100 torr of nitrogen gas was added to the iodine cell. At this higher pressure, collisions transfer population to many rotational and vibrational levels adjacent

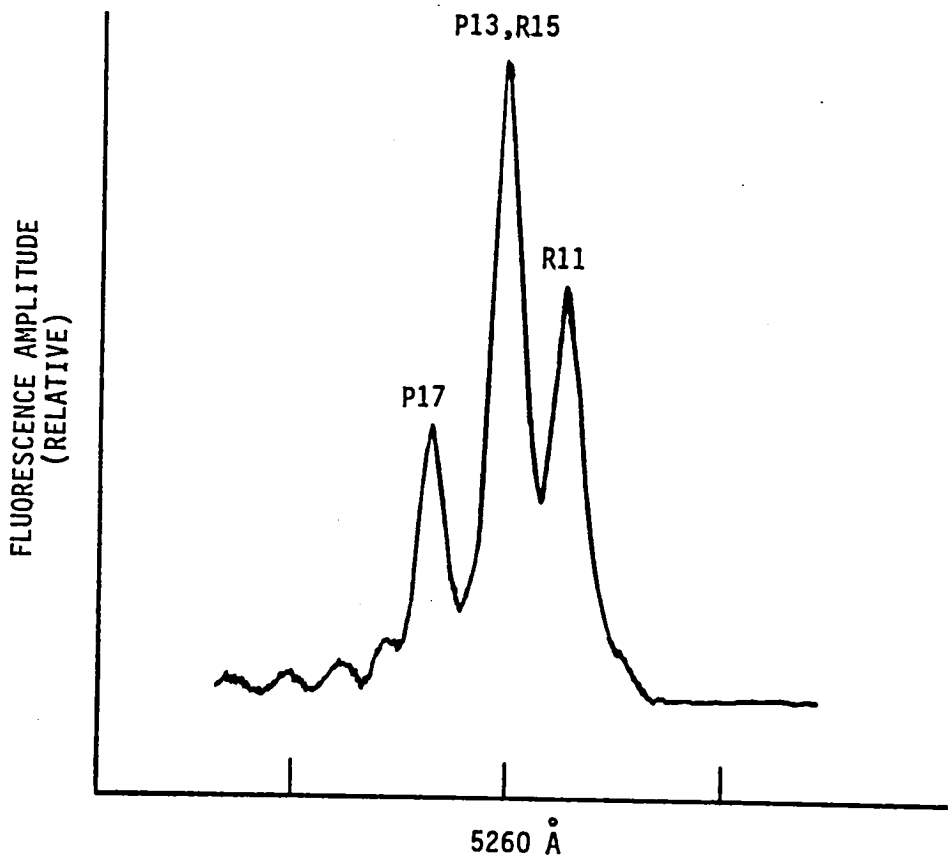

Fig. 21. Triplet Structure of Second Stokes Fluorescence Band at 5260 Å Due to P13 and R15 (43,0) Absorption Transitions at 5145 Å

to the excited-state level which is pumped by the laser radiation. Molecules then fluoresce from these levels, giving rise to the "transfer spectrum". The ratio of transfer to primary fluorescence increases until at about 500 torr of nitrogen the the primary progression is almost lost in the transfer spectrum.

Quenching Mechanisms in the X–B Fluorescent Transitions

Addition of buffer gas causes transfer of population among the excited states

and also causes a decrease of the total fluorescent output. This is due to mechanisms that compete with radiative decay in the iodine molecule. In iodine there are two primary quenching mechanisms. Through collisions with other molecules, some excited-state iodine molecules transfer their energy to their colliding partner and return to the ground state directly. The other quenching mechanism is called *predissociation* and occurs due to the crossing of the B state by the repulsive, or dissociating, D state (as shown in Figure 18). Excitation into the stable B state gives the molecule more than enough energy to dissociate; dissociation will occur if some internal or external mechanism induces a transfer to the unbound D state. Two such predissociation mechanisms exist in iodine: natural, or spontaneous, predissociation and collisionally-induced predissociation. Natural predissociation occurs within an isolated molecule; transfer to the repulsive state is induced by the rotation of the molecule. Collisions with other molecules are also effective in inducing transfer to the repulsive state. Self-quenching by collisions with other iodine molecules and natural predissociation are both negligible compared to foreign gas quenching, for the iodine seeding levels and total pressures of interest in this work.

A parameter of interest is the total electronic quenching rate of the excited state due to foreign gas collisions. This quenching rate is not available in the literature for the specific case of excitation at 5145 Å and collection of the resulting broadband fluorescent emission. An estimate of the value of the quenching rate can be made by measuring the effect on the broadband fluorescent yield of increasing the foreign gas pressure. Using the saturation data given in Table 1, the quenching rate is deduced by plotting S_o/S versus pressure, where S is the fluorescent signal and S_o is the fluorescent signal extrapolated to zero pressure [25]. This plot is shown in Figure 22 for a laser intensity of 7.68×10^3 watts per square cm, so that power broadening effects are negligible. The resulting data points are linear up to a pressure of about 200 torr of nitrogen. The slope of the linear part of the curve is the ratio Q/A_{21},

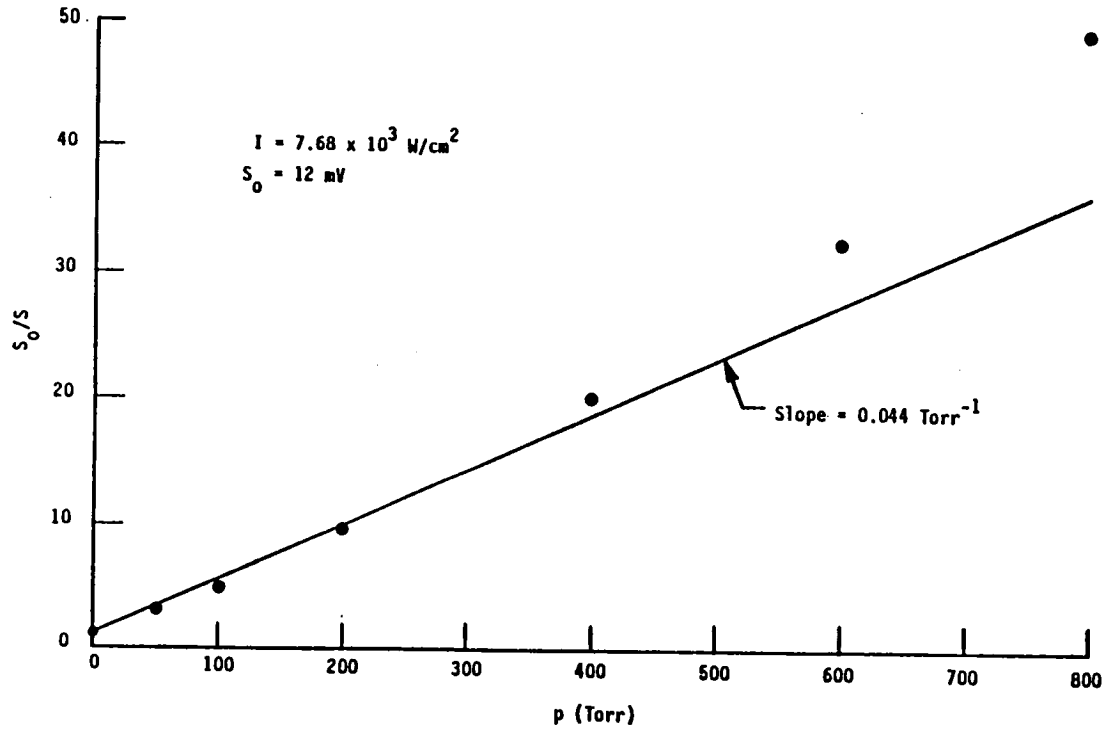

Fig. 22. Stern–Volmer Quenching of Excited Electronic State due to Foreign Gas Collisions: Zero–Pressure Fluorescent Signal / Fluorescent Signal versus Nitrogen Pressure, in torr. (Laser intensity = 7.68 $\times 10^3$ watts per square cm. S_o = 12 mV.)

per torr of nitrogen, and is numerically given as 0.044, per torr. Above 200 torr the effect of pressure broadening becomes important and the curve becomes nonlinear. Therefore, we may write

$$\frac{Q}{A_{21}} = 0.044\, p(\text{torr}).$$

Using a radiative lifetime of 2 microseconds [45], or A_{21} = 0.5 MHz, gives a value for the quenching rate, per unit nitrogen concentration, of 6.82×10^{-13} cm^3/molecule-second. This is the value to be used for the total electronic quenching rate in this work. It is of interest to note that the quenching and spontaneous

emission rates are equal at a pressure of about 23 torr for iodine. At one atmosphere of nitrogen pressure, the quenching rate is about 33 times the spontaneous emission rate.

Lifetimes and Saturation Intensities versus Pressure

The observed decay rate of the excited state is increased as a result of quenching. For zero pressure, the decay rate is given by the spontaneous decay rate, A_{21}, neglecting the effects of natural predissociation and iodine self-quenching. At non-zero pressures the observed decay rate is given by the sum of the spontaneous emission and quenching rates. The observed iodine lifetime, τ_{obs}, may thus be calculated as

$$\frac{1}{\tau_{obs}} = A_{21} + Q \,.$$

Using the above values for these two rates shows that the iodine lifetime decreases from about 0.37 microseconds at 100 torr of nitrogen to about 55 nanoseconds at 800 torr.

The variation of saturation intensity with pressure may be estimated by using the formula

$$I^{sat} = \frac{h\nu}{\sigma \tau_{obs}} \,,$$

where σ is the absorption cross-section and the variation of τ_{obs} with pressure is given above. For an iodine cross-section of 5×10^{-17} square cm, the saturation intensity is estimated to vary from 2.2×10^4 watts/square cm at 100 torr to 1.5×10^5 watts/square cm at 800 torr. These values are approximately four orders of magnitude lower than the corresponding saturation intensities of biacetyl, for example, due to the much lower cross-section and shorter lifetime of the biacetyl

molecule. For this reason the iodine molecule is an attractive molecule with which to carry out saturation studies.

Three–Body Recombination Rate Constant

The recombination of iodine atoms in the presence of various foreign gases has been studied by Rabinowitch and Wood [46]. By measuring the change in transmitted intensity of radiation from a small lamp due to predissociation caused by illumination with an intense lamp, they measured the recombination rate constant to be 6.6×10^{-32} cm^6/molecule^2-second, per unit concentration of nitrogen.

Appendix B

Nonlinear Rate Equation Solution

The solution to the coupled set of nonlinear rate equations derived from the rate equation model for the iodine molecule in Section 2.2 is developed in this appendix. The solution is used to estimate an upper bound on the steady-state atomic population under intense laser pumping of the iodine molecule.

The rate equation model for the iodine molecule under laser excitation led to Equations (2.1)-(2.4) in Section 2.2. A steady-state solution to these equations for the excited-state number density, N_2, is developed and used to calculate the atomic number density, N_3, as follows. Solving for N_1 from Equation (2.1) and for N_3 from Equation (2.3) and inserting these expressions into Equation (2.4) gives

$$\beta \frac{2N_2}{N_I} + \sqrt{\frac{Q_{23}}{2RN_I}}\sqrt{\frac{2N_2}{N_I}} = 1 ,$$

where

$$\beta = \frac{b_{12}f_1 + b_{21}f_2 + A_{21} + Q_{21} + Q_{23}}{b_{12}f_1} .$$

Solving this equation for the fraction of the total number of iodine atoms that appear as excited-state iodine molecules gives

$$\frac{2N_2}{N_I} = \frac{1}{\beta} + \frac{Q_{23}}{4RN_I\beta^2}\left(1 \pm \sqrt{1 + \frac{8\beta RN_I}{Q_{23}}}\right).$$

In order to express this formula for the fractional population of atoms in the excited molecular state in terms of the laser intensity, an expression for the stimulated rate coefficients and the saturation intensity must be employed. The broadband formulas of Section 2.4 are used since they are algebraically simpler than the narrow bandwidth relations and since the resulting expression is compared with the saturation data obtained with a broadband argon laser. Using Equations (2.34) and (2.11) for the stimulated rate coefficients and Equation (2.36) for the saturation intensity gives

$$\beta = \left(1 + \frac{f_2 g_1}{f_1 g_2}\right)\frac{1+\tilde{I}}{\tilde{I}},$$

where $\tilde{I} = I_\nu / I_\nu^{sat}$ and $Q = Q_{21} + Q_{23}$. Using this expression for β gives the final solution for the fractional population of atoms in the excited molecular state as

$$\frac{2N_2}{N_I} = \left(\frac{f_1}{f_1 + f_2 g_1/g_2}\right)\frac{\tilde{I}}{1+\tilde{I}} + \left(\frac{f_1}{f_1 + f_2 g_1/g_2}\right)^2 \left(\frac{\tilde{I}}{1+\tilde{I}}\right)^2 \frac{Q_{23}}{4RN_I}\left[1 \pm \sqrt{1 + \frac{8RN_I}{Q_{23}}\left(1 + \frac{f_2 g_1}{f_1 g_2}\right)\frac{1+\tilde{I}}{\tilde{I}}}\right].$$

Is is seen that the solution for the fractional population of atoms in the excited molecular state consists of two terms. The first term is the solution obtained, Equation (2.35), when the atomic population, N_3, is neglected in the atom conservation equation, (2.4), and the resulting linear equations are solved. The second term is the nonlinear contribution obtained when the atomic population is not neglected when developing the solution to the full nonlinear set of rate equations. The assumption that the atomic population, N_3, can be neglected in Equation (2.4) is, therefore, equivalent to assuming that the second term in the nonlinear rate equation solution is negligible compared to the first. The validity of this assumption is evaluated in the remainder of this appendix by comparing the nonlinear solution to the saturation data of Section 3.3.

A comparison of the size of the two terms in the above solution can be made by calculating $2N_2/N_I$ as a function of $\tilde{I}$. In doing this calculation, all the parameters that occur in the expression are either available from the literature or from the results of the main body of this work, except for the quenching rate constant, Q_{23}. The ratio of degeneracies of the levels is taken as unity. The total number of iodine atoms, N_I, is calculated from the room temperature vapor pressure to be 1.95×10^{16} atoms/cm^3. The initial population fraction, f_1, is given in Section 2.3.2 as 0.0034 at room temperature and the excited population fraction, f_2, is found in Section 3.3 to be 0.025. Values for the three–body recombination rate, R, and the total electronic quenching rate, Q, are given in Appendix A. However, a value for the quenching rate constant Q_{23} is needed to calculate the second term of the above expression and this value is not available in the literature. The ratio Q_{21}/Q_{23} is, therefore, taken as an unknown parameter to be determined by comparing calculations based on the above equation, for various values of the ratio, to experimental data.

The results of the calculation of $2N_2/N_I$ versus $\tilde{I}$ for various values of Q_{21}/Q_{23} is shown in Figure 23. (There is a choice of signs in the above expression; the minus sign must be used since the plus sign gives values of $2N_2/N_I$ greater than unity for large values of $\tilde{I}$.) A lower bound on the value of this ratio can be deduced by comparison of the calculated curves with the experimental saturation data of Figure 3. The data in Figure 3 show that the fluorescent signal (which is proportional to the excited–state number density) is linear with laser intensity for intensities up to an $\tilde{I}$ of at least 0.1. (For example, the 800 torr data curve is still linear at an intensity of 7.61×10^3 watts per square cm, corresponding to an $\tilde{I}$ value of 0.1.) However, for small values of the ratio, Q_{21}/Q_{23}, the calculated curves are far from linear at this nondimensional intensity. In order for the calculated curve to be linear up to an $\tilde{I}$ of 0.1, as indicated by the experimental data, the ratio Q_{21}/Q_{23} must be on the order of 10^4 in Figure 23. This means that Q_{23} must have a numerical value

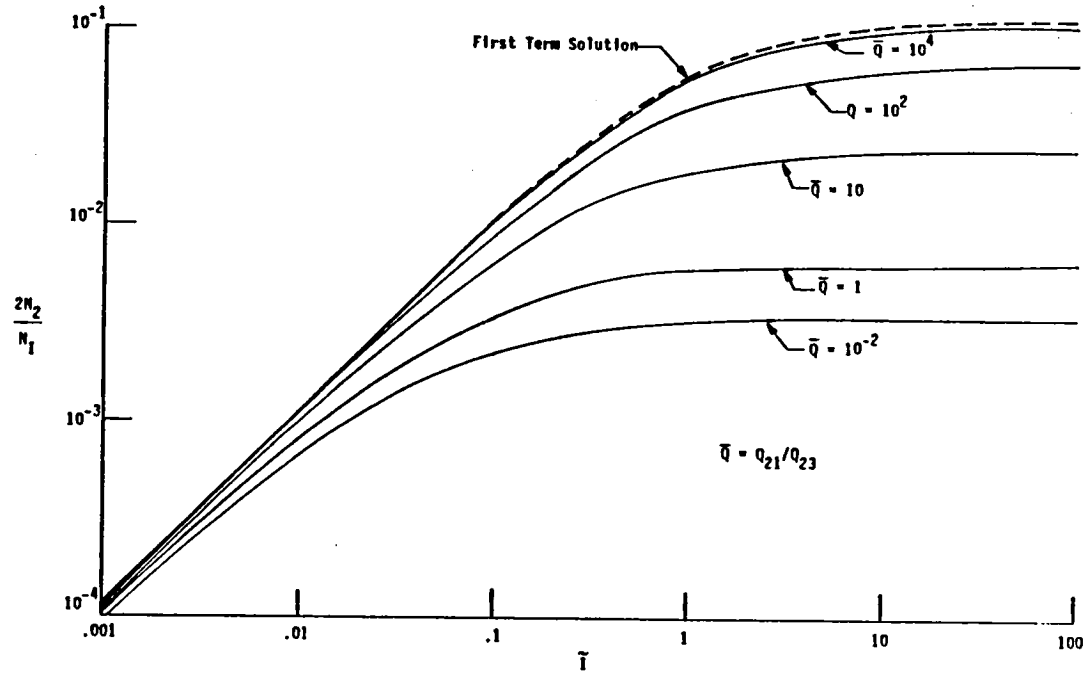

Fig. 23. Fraction of Total Number of Iodine Atoms in Excited Molecular State versus Nondimensional Laser Intensity for Various Values of the Excited-State Quenching Ratio

on the order of 6.8×10^{-17} cm^3/molecule-second. For this value of Q_{23}, the difference in the full solution and the first term (also shown in the figure) is 5.9 % for $\tilde{I} = 100$. The corresponding steady-state population of atoms in the atomic state, N_3/N_I, is calculated from Equation (2.3) to be 5.4 % for $\tilde{I} = 100$. This is the maximum atomic population under the most intense laser illumination used in this work and is also the maximum error that is made in the atom conservation equation when the atomic population is neglected.

It is therefore concluded that, due to the small value of Q_{23} relative to the total electronic quenching rate, Q, the atomic population, N_3, in the atom conservation

equation, (2.4), can be neglected and the resulting solution will be accurate to better than about 5 %, even at the largest laser intensities employed in this work. This means that since only one out of every ten thousand excited-state iodine molecules is quenched via predissociation, the atomic population never becomes appreciable, even though the three-body recombination rate is very small and the laser pumping rate can be large. This conclusion is consistent with the experimental evidence of Reference 18 that a negligible percentage of iodine molecules are dissociated into atoms under intense steady-state illumination.

References

[1] M. Hugenschmidt and K. Vollrath, "Light Sources and Recording Methods," in *Methods of Experimental Physics,* volume 18, part B, Academic Press, New York, 1981, pp. 739–753.

[2] R. Goulard and P.J. Emmerman, "Multiangular Absorption Diagnostics in Combustion," in *Inverse Scattering in Optics,* Springer–Verlag, New York, 1980.

[3] T.M. Dyer, "Rayleigh Scattering Measurements of Time–Resolved Concentration in a Turbulent Propane Jet," AIAA Journal, volume 17, number 8, 1978, p. 912.

[4] R.W. Dibble, R.E. Hollenbach and G.D. Rambach, "Temperature Measurement in Turbulent Flames via Rayliegh Scattering," in *Laser Probes for Combustion Chemistry,* American Chemical Society, Washington D.C., 1980, p. 435.

[5] M.B. Long, B.T. Chu and R.K. Chang, "Instantaneous Two–Dimensional Gas Concentration Measurement by Light Scattering," AIAA Journal, volume 19, number 9, 1981, p. 1151.

[6] M. Lapp and C.M. Penny, editors, *Laser Raman Gas Diagnostics,* Plenum Press, New York, 1974.

[7] D.R. Crosley, editor, *Laser Probes for Combustion Chemistry,* American Chemical Society, Washington D.C., 1980, pp. 61–203.

[8] J.C. McDaniel and D. Baganoff, "Density Measurement with a Bleaching Seed Gas," Bulletin of the American Physical Society, volume 23, number 9, 1978.

[9] R.L. Farrow and L.A. Rahn, "Spatially Resolved Infrared Absorption Measurement: Application of an Optical Stark Effect," Optics Letters, volume 6, number 3, 1981, p. 108.

[10] G. Kychakoff and R.K. Hanson, "Tunable Laser Fiberoptic Probe for Absorption–Fluorescence Combustion Measurements," paper 81–50, Western States Section, The Combustion Institute 1981 Fall Meeting, October 1981.

[11] R.F. Begley, A.B. Harvey, R.L. Byer and B.S. Hudson, "A New Spectroscopic Tool: Coherent anti–Stokes Raman Spectroscopy," American Laboratory, November 1974.

[12] A.C. Eckbreth, P.A. Bonczyk and J.A. Shirley, "Investigation of Saturated Laser Fluorescence and CARS Spectroscopic Techniques for Combustion Diagnostics," EPA–600/7–78–104, June 1978.

[13] A.H. Epstein, "Quantitative Density Visualization in a Transonic Compressor Rotor," Journal of Engineering for Power, volume 99, number 3, 1977, p.460.

[14] R.L. McKenzie, D.J. Monson and R.J. Exberger, "Time–Dependent Local Density Measurements in Unsteady Flows," NASA TM 78555, February 1979.

[15] J.W. Daily, "Use of Rate Equations to describe Laser Excitation in Flames," Applied Optics, volume 16, number 8, 1977, p. 2322.

[16] R.P. Lucht and N.M. Laurendeau, "Two–Level Model for Near Saturated Fluorescence in Diatomic Molecules," Applied Optics, volume 18, number 6, 1979, p. 856.

[17] D.R. Olivares and G.M. Hieftje, "Saturation of Energy Levels in Analytic Atomic Fluorescence Spectroscopy–I. Theory," Spectrochimica Acta., volume 33B, 1978, p. 79.

[18] E. Rabinowitch and W.C. Wood, "Dissociation of Excited Iodine Molecules," Journal of Chemical Physics, volume 4, 1936, p. 358.

[19] E.H. Piepmeier, "Theory of Laser Saturated Atomic Resonance Fluorescence," Spectrochimica Acta., volume 27B, 1972, p. 431.

[20] A. Yariv, *Quantum Electronics,* Wiley and Sons, New York, 1975.

[21] B.H. Armstrong, "Spectrum Line Profiles: The Voigt Function," J. Quant. Spectrosc. Radiat. Transfer, volume 7, 1967, p. 61.

[22] H. Greenstein, "Line–Width and Tuning Effects in Resonant Excitation," Journal of the Optical Society of America, volume 65, number 1, 1975, p. 33.

[23] C. Young, "Tables for Calculating the Voigt Profile," NASA TR 05863–7–T, July 1965.

[24] J.W. Daily, "Saturation of Fluorescence in Flames with a Gaussian Laser Beam," Applied Optics, volume 17, number 2, 1978, p. 225.

[25] R.L. Brown and W. Klemperer, "Energy Transfer in the Fluorescence of Iodine Excited by the Sodium D Lines," Journal of Chemical Physics, volume 41, number 10, 1964, p. 3072.

[26] D. Stepowski and M.J. Cottereau, "Direct Measurement of OH Local Concentration in a Flame from the Fluorescence induced by a Single Laser Pulse," Applied Optics, volume 18, number 3, 1979, p. 354.

[27] A.P. Baronavski and J.R. McDonald, "Application of Saturation Spectroscopy to the Measurement of C_2 Concentrations in Oxy–Acetylene Flames," Applied Optics, volume 16, number 7, 1977, p. 1897.

[28] D.W. Posener, "The Shape of Spectral Lines: Tables of the Voigt Profile," Australian Journal of Physics, volume 12, 1959, p. 184.

[29] E. Hecht and A. Zajac, *Optics,* Addison–Wesley, Reading, Ma., 1979.

[30] A.E. Siegman, *An Introduction to Lasers and Masers,* McGraw–Hill, New York, 1971.

[31] P.R. Bevington, *Data Reduction and Error Analysis for the Physical Sciences,* McGraw–Hill, New York, 1969.

[32] B.H. Armstrong and R.W. Nicholls, *Emission, Absorption and Transfer of Radiation in Heated Atmospheres,* Pergamon Press, New York, 1972.

[33] M. Kroll and D. Swanson, "The Resonance Fluorescence of I_2 excited by a Single Mode Laser," Chemical Physics Letters, volume 9, number 2, 1971, p. 115.

[34] S. Gerstenkorn and P. Luc, "Assignments of Several Groups of Iodine Lines in the B–X System," Journal of Molecular Spectroscopy, volume 77, 1979, p. 310.

[35] H.W. Liepman and A. Roshko, *Elements of Gasdynamics,* Wiley and Sons, New York, 1957.

[36] P.A. Thompson, *Compressible-Fluid Dynamics,* McGraw-Hill, New York, 1972.

[37] H. Askenas and F.S. Sherman, "The Structure and Utilization of Supersonic Free Jets in Low Density Wind Tunnels," in *Rarefied Gas Dynamics,* volume 2, Academic Press, New York, 1966, p.84.

[38] J. Tellinghuisen, "Intensity Factors for the I_2 B–X Band System," J. Quant. Spectrosc. Radiat. Transfer, volume 19, 1978, p. 149.

[39] M. Zimmerman and R.B. Miles, "Hypersonic-Helium-Flow-Field Measurements with the Resonant Doppler Velocimeter," Applied Physics Letters, volume 37, number 10, 1980, p. 885.

[40] S. Gerstenkorn and P. Luc, "Atlas du Spectre de la Molecule de l'Iode," unpublished

[41] J.D. Simmons and J.T. Hougen, "Atlas of the I_2 Spectrum from 19000 to 18000 cm^{-1}," Journal of Research of the NBS–A, volume 81A, number 1, 1977, p. 25.

[42] S.N. Suchard and J.E. Melzer, "Spectroscopic Constants for Selected Homonuclear Diatomic Molecules," volume I, SAMSO–TR–76–31, 1976.

[43] J.I. Steinfeld, R.N. Zare, L. Jones, M. Lesk and W. Klemperer, "Spectroscopic Constants and Vibrational Assignments for the B State of Iodine," Journal of Chemical Physics, volume 42, number 1, 1965, p. 25.

[44] M.D. Levenson and A.L. Schawlow, "Hyperfine Interactions in Molecular Iodine," Physical Review A, volume 6, number 1, 1972, p. 10.

[45] G.A. Capelle and H.P. Broida, "Lifetimes and Quenching Cross Sections of I_2," Journal of Chemical Physics, volume 58, number 10, 1973, p. 4212.

[46] E. Rabinowitch and W.C. Wood, "Kinetics and Recombination of Iodine Atoms," Journal of Chemical Physics, volume 4, 1936, p. 497.